

Measurement of Particle Species Dependence of Elliptic Anisotropy  
with High Resolution Reaction Plane Detector  
at  $\sqrt{s_{NN}} = 39, 62$  and 200 GeV Au+Au Collisions  
at RHIC-PHENIX

Yoshimasa IKEDA

February 2014



Measurement of Particle Species Dependence of Elliptic Anisotropy  
with High Resolution Reaction Plane Detector  
at  $\sqrt{s_{NN}} = 39, 62$  and  $200$  GeV Au+Au Collisions  
at RHIC-PHENIX

Yoshimasa IKEDA  
Doctoral Program in Physics

Submitted to the Graduate School of  
Pure and Applied Sciences  
in Partial Fulfillment of the Requirements  
for the Degree of Doctor of Philosophy in  
Science  
at the  
University of Tsukuba

# abstract

According to quantum chromodynamics, quarks and gluons are confined with the strong force in hadron. It is expected that they are de-confined in a high temperature or high density. It is called Quark Gluon Plasma (QGP). The QGP may have existed in the early universe according to the big bang theory or in the core of the neutron star. Experimentally, it is formed by a relativistic heavy ion collision with a collider. Participant nucleons are distinguished from spectator nucleons in the relativistic collision. The system geometry is elliptical at the first stage of a non-central collision. The geometrical anisotropy generates the asymmetry in the yield of particles as a function of the azimuthal angle with respect to the event plane of an event. The azimuthal anisotropy indicates an interaction with a short mean free path of parton in the hot dense medium. And it gives information about the initial state and its expansion possibly through the QGP phase.

The magnitude of azimuthal anisotropy of particle emission is measured as the second term of Fourier series ( $v_2$ ). The measured  $v_2$  of hadrons increases with the transverse momentum  $p_T$  in the low  $p_T$  range ( $p_T < 2$  GeV/c). The rise of  $v_2$  of hadrons shifts towards higher  $p_T$  for heavier particles. A hydrodynamic model with a low viscosity reproduces the collective behavior for the particles. The  $v_2$  reaches to a constant value at  $p_T = 2 - 3$  GeV/c where the value scales with the constituent quark number and independent of the particle mass. It indicates that the flow of hadrons is built up by the flow of quarks in the QGP according to the quark coalescence model. The  $v_2$  of hadron is the sum of  $v_2$  of combined partons in the quark coalescence model. The experimental result of quark number scaling of  $v_2$  suggest the quark level collectivity in the hot dense matter and the quark coalescence mechanism to form hadron from quark matter via quark-gluon phase transition.

A new reaction plane detector was installed to measure the  $v_2$  of hadrons with an enhanced event plane resolution at RHIC-PHENIX experiment. It was developed as the suitable detector to measure the event plane of the heavy ion collision. It measures the azimuthal distribution of charged hadron yield with an acceptance of  $\phi = 2\pi$  and  $\eta = 1.5 - 2.8$ . The event plane was determined with two times better resolution compared to the ones measured before in the  $\sqrt{s_{NN}} = 200$  GeV Au+Au collision in PHENIX experiment. The higher resolution allows us to study  $v_2$  of rare particles or low energy collisions.

The  $v_2$  of  $\pi$ ,  $K$ ,  $p$ ,  $\bar{p}$ ,  $\Lambda$ ,  $\bar{\Lambda}$ ,  $\phi$ ,  $d$  and  $\bar{d}$  were measured in the Au+Au  $\sqrt{s_{NN}} = 200$  GeV collision. A blast-wave function describes the  $p_T$  spectra via the radial expansion with parameters of a local thermal temperature and a radial velocity at the freeze out. The blast-wave function is extended to describe the  $v_2$  as a function of  $p_T$ . The initial geometrical density distribution is taken from Glauber Monte-Carlo model with Wood-Saxon distribution. An additional elliptic expansion parameter, where the initial density distribution can expand into the reaction plane direction, is included to determine the final density distribution at the freeze-out. The gradient of the density distribution is used as velocity profile and is scaled by the overall radial expansion velocity. The

final eccentricity was given by the blast wave fitting to the measured  $p_T$  spectra and  $v_2$  of the six particles. The freeze-out eccentricity has been found to be smaller than the initial eccentricity, but it still holds the same orientation. The observation is consistent with the eccentricity extracted from Hunbury Brown and Twiss (HBT) effect measurement.

The  $v_2$  of baryons are larger than the  $v_2$  of mesons and the  $v_2$  of  $d$  is higher than the  $v_2$  of baryons at  $p_T > 3$  GeV/c.  $KE_T = m_T - m_0$  scaling describes the  $v_2$  shift by the mass effect.  $v_2$  as a function of  $KE_T$  of mesons, baryons and  $d$  seem to be given by centrality and the number of constituent quarks of the particles  $n_q$ . The  $v_2/n_q$  of the particles are consistent with each other at  $KE_T/n_q < 0.7$  GeV.  $\phi$  has a smaller cross section of the hadronic re-scattering. Therefore this consistency of the  $v_2$  of the particles indicates the  $v_2$  is generated before the QGP-hadron phase transition and less affected from the hadronic re-scattering after the QGP-hadron phase transition. The scaled  $v_2$  with the number of constituent quarks of the five hadrons and  $d$  indicates the quark level collectivity in the QGP, and hadron generation according to the quark coalescence mechanism during QGP-hadron phase transition.

The scaling of  $v_2$  with  $n_q$  and  $KE_T$  is broken at  $KE_T/n_q > 0.7$  GeV. The  $v_2$  of  $\pi$  and  $p$  are approaching each other at the high  $p_T$  range (6 GeV). It is known that there are different particle generation mechanisms such as jet production from hard process at the high  $p_T$ . In this case,  $v_2$  of the high  $p_T$  particle is expected to be given by the path length dependence of the jet quenching coming from the partonic energy loss.

The  $v_2$  of  $\pi$ ,  $K$ ,  $p$ ,  $\bar{p}$  and  $d$  were measured in the Au+Au  $\sqrt{s_{NN}} = 39$  and 62 GeV collisions. Particle (especially  $p$ )  $v_2$  differs from anti-particle  $v_2$  in these lower beam energy collisions. It could be given by interactions such as  $p$ - $\bar{p}$  annihilation in the high baryon density caused by the baryon stopping in the low energy collision. The number of constituent quark scaling of hadron  $v_2$  is mostly established in these energies. Considering this as an indication of the QGP phase, the threshold energy of the QGP-hadron phase transition would be lower than  $\sqrt{s_{NN}} = 39$  GeV.

# Contents

<b>1</b>	<b>Introduction</b>	<b>1</b>
1.1	Quantum Chromodynamics . . . . .	1
1.2	High energy heavy ion collision and QGP study . . . . .	1
1.2.1	collision geometry . . . . .	1
1.2.2	Time evolution . . . . .	2
1.2.3	Bjorken energy density . . . . .	3
1.3	System expansion and flow . . . . .	4
1.3.1	collective flow . . . . .	4
1.3.2	elliptic flow . . . . .	4
1.3.3	Hydro dynamic model . . . . .	5
1.3.4	Blast-wave model parametrization . . . . .	7
1.3.5	Quark coalescence model . . . . .	8
1.4	Thesis motivation . . . . .	8
<b>2</b>	<b>Experiment</b>	<b>10</b>
2.1	Relativistic Heavy Ion Collider . . . . .	10
2.2	Detectors of PHENIX experiment . . . . .	10
2.2.1	Beam-Beam Counter . . . . .	12
2.2.2	Zero Degree Calorimeter . . . . .	14
2.2.3	Muon Piston Chamber . . . . .	14
2.2.4	PHENIX magnet . . . . .	15
2.2.5	Drift Chamber . . . . .	15
2.2.6	Pad Chamber . . . . .	15
2.2.7	Time Of Flight . . . . .	16
2.2.8	Aerogel Cerenkov Counter . . . . .	16
2.2.9	Lead Scintillator Electromagnetic Calorimeter . . . . .	16
2.2.10	Ring Image Cerenkov Counter . . . . .	17
2.2.11	New Reaction Plane Detector (RxP) . . . . .	17
<b>3</b>	<b>Reaction Plane Detector</b>	<b>18</b>
3.1	Reaction Plane determination for flow analysis . . . . .	18
3.2	Reaction Plane resolution . . . . .	20
3.3	Reaction plane measurement in PHENIX . . . . .	20
3.4	Geant4 simulation and construction of RxP . . . . .	20
3.5	Resolution of RxP in PHENIX-Run7 (2007) . . . . .	27

<b>4 Analysis</b>	<b>34</b>
4.1 Event selection . . . . .	34
4.2 Reaction Plane Calibration . . . . .	34
4.3 Resolution estimation of Reaction Plane . . . . .	35
4.4 Reconstruction of charged particles . . . . .	36
4.5 Particle identification by Time of Flight . . . . .	36
4.6 Particle identification with ACC at high $p_T$ . . . . .	38
4.7 $d v_2$ . . . . .	42
4.7.1 Method 1 ( $\langle \cos 2\Delta\phi \rangle$ and S/N calculation) . . . . .	42
4.7.2 Method 2 (Mass fitting) . . . . .	42
4.7.3 Method 3 (Fourier fitting) . . . . .	48
4.7.4 method 4 (In-Out ratio) . . . . .	48
4.7.5 Comparison with the methods . . . . .	48
4.8 $\Lambda$ and $\bar{\Lambda}$ reconstruction with $p\pi^-$ and $\bar{p}\pi^+$ . . . . .	51
4.9 $\phi$ -meson reconstruction with $K^+K^-$ pair . . . . .	51
4.10 $p_T$ value of each X-axis bin. . . . .	64
4.11 New reaction plane resolution in PHENIX . . . . .	66
4.12 Systematic Error estimation . . . . .	66
4.12.1 Auto-correlation and jet effect . . . . .	68
4.12.2 Uncertainty of Reaction Plane . . . . .	68
4.12.3 Uncertainty of particle identification . . . . .	70
4.12.4 Other Uncertainties . . . . .	73
<b>5 Result and discussions</b>	<b>75</b>
5.1 The elliptic flow ( $v_2$ ) of hadrons as a function of transverse momentum ( $p_T$ ) in Au+Au $\sqrt{s_{NN}} = 200$ GeV . . . . .	75
5.2 $KE_T$ and Quark number scaling . . . . .	75
5.3 Blast wave fitting . . . . .	79
5.4 comparison between particles . . . . .	82
5.4.1 $p$ and $d$ . . . . .	82
5.4.2 $p$ and $\Lambda$ . . . . .	82
5.4.3 $\pi$ , $K$ and $\phi$ mesons . . . . .	94
5.5 Charm study . . . . .	94
5.6 Interaction between hard and soft . . . . .	100
5.7 consistency between particles and anti-particles . . . . .	104
5.8 Measurement of $v_2$ at Au+Au $\sqrt{s_{NN}} = 39$ and 62 GeV. . . . .	116
5.9 Summary . . . . .	122
<b>6 Conclusions</b>	<b>124</b>
<b>7 Acknowledgments</b>	<b>127</b>
<b>Reference</b>	<b>128</b>

# Chapter 1

## Introduction

### 1.1 Quantum Chromodynamics

Quantum Chromo-Dynamics (QCD) is a quantum field theory of a special kind called a non-Abelian gauge theory. It is important for the Standard Model in the particle physics. In QCD, the strong interaction is calculated. The strong interaction is one of the four fundamental forces. Quarks and gluons are interacting with the strong force in any hadron. Hadron has two quarks is called meson and that has three quarks is called baryon. Gluons mediate them by the strong interaction.

The attractive force between quarks increases in proportion to the distance between them. This means it would take an infinite amount of energy to separate two quarks. Gluon exchange the strong force between quarks. Experimentally, any search of the single quark has failed. This confinement is expected in the lattice QCD calculation.

The lattice QCD is a well-established non-perturbative approach to solving the quantum chromodynamics theory of quarks and gluons. It is a lattice gauge theory formulated with a grid or lattice of points in space and time. Confinement of quark is dominant in low energy scales, but asymptotic freedom in which quarks and gluons interact weakly becomes dominant in high energy scale. It is called Quark Gluon Plasma (QGP) if quark and gluon are deconfined in the high energy density. The temperature reaches the QCD energy scale  $T \sim 10^{12}$  K  $\sim 170$  MeV (Fig.1.1). It corresponds to an energy density  $\epsilon \sim 1$  GeV/fm<sup>3</sup>. This is one order of magnitude larger than that of normal nuclear matter[1, 2].

The QGP may have exist in the early universe according to the big bang theory or in the core of the neutron star at the normal temperature[3, 4].

### 1.2 High energy heavy ion collision and QGP study

#### 1.2.1 collision geometry

Experimentally, the QGP is formed by a relativistic heavy ion collision with a collider. The experiments are carried out to search QGP at CERN and BNL since 1980. The nuclei are accelerated to a relativistic velocity. Lorentz contracted nuclei being discal and slammed into each other. A participant which consists of colliding nucleons and spectators which consist of non-colliding nucleons are separated well because the relativistic speed is much faster than the Fermi motion of nucleons in the nucleus. The impact parameter is defined by the distance between the centers of two nuclei in the collision. The measured particle yields (and energy) in the participant and the spectators

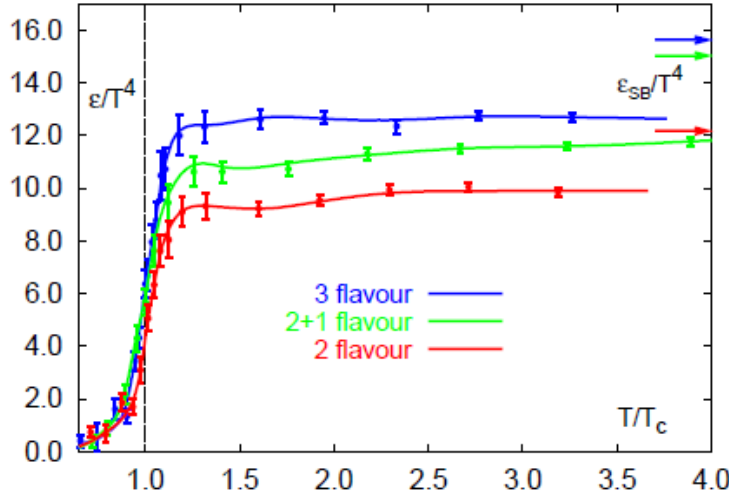


Figure 1.1: The energy density  $\epsilon$  divides by  $T^4$  as a function of temperature  $T$  scaled with the critical temperature  $T_c$  calculated in Lattice QCD simulation[2]. The arrows on the right side indicating the values of the Stefan-Boltzmann limit.

are used to estimate the impact parameter. The number of participant nucleons ( $N_{part}$ ) is related to impact parameter and they can be estimated by Glauber Model. Number of nucleon-nucleon collisions ( $N_{coll}$ ) and spatial eccentricity are given by the impact parameter, too[5].

In the experiment, the centrality of the collision is often estimated by measurement of the multiplicity of the generated particles because the  $N_{part}$  and the multiplicity are almost linearly correlated. The centrality is calibrated to be flat over 0 - XX % (0 - 92 % at Au+Au  $\sqrt{s_{NN}} = 200$  GeV or 0 - 86 % at Au+Au  $\sqrt{s_{NN}} = 62$  and 39 GeV).

### 1.2.2 Time evolution

In the relativistic heavy ion collision, two discal ions pass through each other, and hot dense matter is generated just after that. The hot dense matter (may be QGP or not) will expand under its own pressure and be cooled. The generated quarks and gluons from hard scattering are emitted after hadronization even if they go through QGP phase. J. D. Bjorken suggested the space-time evolution from quark generation to hadron emission of the high energy heavy ion collision based on hydrodynamics[6]. The evolution of the hot dense matter would be described by the hydrodynamics framework if a thermal equilibrium is achieved[7].

Figure 1.2 shows the image of the space-time evolution. In this picture, ions collide at  $z = 0$ . The system size of the collision is same as overlap of the ions. Many partons (quarks and gluons) are generated by hard scattering. The system begins expansion in space. QGP may be created if the energy density is enough to that at  $\tau = \tau_0$ . The QGP system expands based on hydrodynamics if local equilibration is achieved in the system. The QGP phase will be changed to hadron gas phase when the matter cools down to the critical temperature  $T_C = 180$  MeV, which is called QGP phase transition. The hadron gas system expands with hadron scattering and hadrons are emitted. Species of the emitting particle are fixed when inelastic scattering is finished, which is called chemical

freeze-out. Momentum distribution of particle emission is fixed when elastic scattering is finished, which is called thermal freeze out.

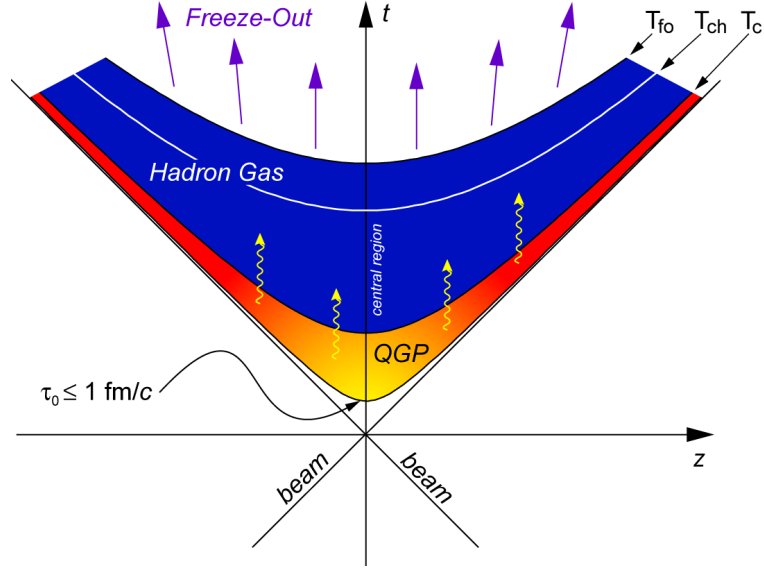


Figure 1.2: Time scale of high energy heavy ion collision with QGP phase transition.

### 1.2.3 Bjorken energy density

Bjorken estimated the energy density  $\epsilon$  of forming hot matter at a timing  $\tau_0$  as follows,

$$\epsilon = \frac{1}{\pi R_A^2 \tau_0} \frac{dE_T}{dy}, \quad (1.1)$$

$$\langle m_T \rangle \frac{dN}{dy} = \frac{dE_T}{dy}, \quad (1.2)$$

$$m_T = \sqrt{p_T^2 + m^2}, \quad (1.3)$$

$$y = \frac{1}{2} \ln \left( \frac{t+z}{t-z} \right), \quad (1.4)$$

where  $E_T$  is total energy and  $dz = \tau dy$  at the central rapidity ( $y = 0$ )[6],  $m_T$  is transverse mass,  $E_T$  means transverse energy of the produced hadrons,  $N$  is the number of particles,  $y$  is rapidity and  $dN/dy$  means rapidity distribution of particle multiplicity. The total energy  $E$  and volume of the system  $\Delta V$  at  $\tau_0$  are shown as follows,

$$E = \langle m_T \rangle \frac{dN}{dy} \delta y = \frac{dE_T}{dy} \delta y, \quad (1.5)$$

$$\Delta V = \pi R^2 dz, \quad (1.6)$$

$$\epsilon_0 = \frac{\Delta E}{\Delta V} = \frac{1}{\pi R^2 \tau_0} \frac{dE_T}{dy}, \quad (1.7)$$

where  $R$  is a radius of the colliding nucleus.  $\epsilon_0$  was estimated with measured  $dE_T/dy$  in the heavy ion experiment. The value is  $\epsilon_0 = 9(5.5)$  GeV/fm $^3$  ( $\tau_0 = 0.6(1.0)$  fm/c) in the Au+Au  $\sqrt{s_{NN}} = 200$  GeV collision at RHIC. The energy density is enough to form QGP ( $\epsilon_c > 1$  GeV/fm $^3$ ) according to the lattice QCD model. QGP formation is expected because the energy density is higher than the critical point at RHIC.

## 1.3 System expansion and flow

### 1.3.1 collective flow

The momentum distributions of particles are measured after thermal freeze-out which means the mean free path becomes larger than the size of the system. The momentum distributions of the particles follow the Boltzmann distribution if the system is a thermal equilibrium state of the hadron gas. The transverse momentum ( $p_T$ ) distribution is described as follows,

$$\frac{dN}{m_T dm_T} = A \exp\left(-\frac{m_T}{T}\right), \quad (1.8)$$

where  $A$  is a constant,  $T$  is the inverse slope parameter which is the mean temperature of the system during the thermal freeze-out and  $m_T$  is called transverse mass that is given by transverse momentum and mass of the particle[8]. This is an exponential function and the slope parameter does not depend on mass in  $pp$  collision. One temperature is given by  $\pi$ ,  $K$ ,  $p$  for a small system ( $T_\pi = T_K = Tp = 150$  MeV) [9].

Conversely, the slope parameter depends on mass in heavy ion collision[10, 11]. Light particles have small slope and heavy particle have large slope[12]. The slope that depends on system size and particle mass, indicates collective flow of particles in the high energy heavy ion collision. Particles have a common transverse velocity of the collective expansion in transverse direction. The inverse slope parameter  $T$  can be written as follows,

$$T = T_f + 0.5m\beta^2, \quad (1.9)$$

where  $T_f$  is the thermal temperature,  $m$  is particle mass and  $\beta$  is the collective velocity. In Au+Au  $\sqrt{s_{NN}} = 200$  GeV collision, these parameters are measured as  $T_f = 177.0 + 1.2$  MeV and  $\beta = 0.48 + 0.07$  with  $\pi$ ,  $K$ , and  $p$ [13].

### 1.3.2 elliptic flow

The study of collective flow is important for high energy heavy ion collision. One of the clues of the property of the hot dense medium is to study of the state of the collective expansion of the system. The system geometry is elliptical at the first stage of non-central heavy ion collision. The plane includes the beam lines and the minor axis of the oval overlap region is called reaction plane. The particle emission yield as a function of the azimuthal angle depends on the system geometry in Au+Au  $\sqrt{s_{NN}} = 200$  GeV collision at RHIC. It indicates the mean free path is smaller than the

size of the system. The magnitude of azimuthal anisotropy of particle emission is measured as the second term of Fourier series ( $v_2$ ),

$$dN/d\phi = N(1 + 2v_2 \cos 2(\phi - \Psi)), \quad (1.10)$$

where  $N$  is number of the particle emissions,  $\phi$  is azimuthal angle of the particle emission [rad] and  $\Psi$  is the reaction plane angle [rad]. The anisotropy parameter  $v_2$  is called “elliptic flow”. The large  $v_2$  is an indicator of the small mean free path in the hot dense medium.

The measured  $v_2$  of hadrons increases with  $p_T$  in the low  $p_T$  range ( $p_T < 2$  GeV/c). The observed  $p_T$  dependence of identified particle  $v_2$  has two important features. The rise of  $v_2$  shifts towards higher  $p_T$  for heavier particles. This indicates the radial collective flow of the particles and the common acquired velocity from the flowing medium for all the different mass particles. On the other hand, the  $v_2$  of  $p$  is larger than that of  $\pi$  or  $K$  in high  $p_T$  range ( $p_T > 2$  GeV/c). The  $v_2$  reaches to a constant value at  $p_T = 2 - 3$  GeV/c where the values scale with the number of constituents quark and independent of the particle mass. This indicates the flow of hadrons is built up by the flow of quarks in QGP according to quark coalescence model.

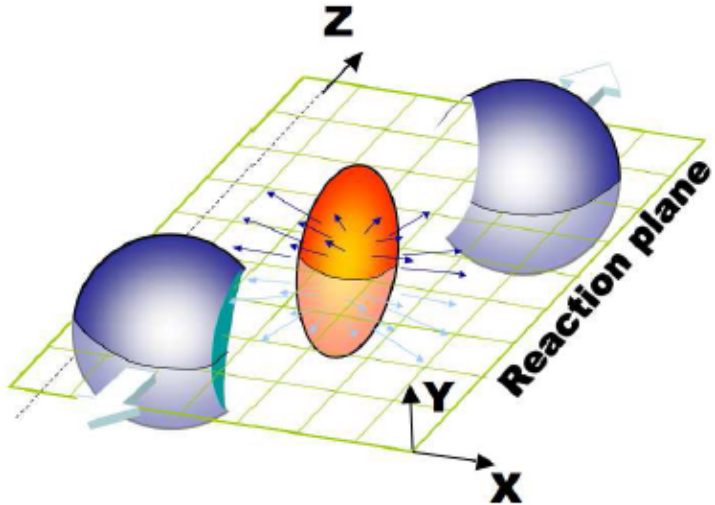


Figure 1.3: Picture of a participant and spectators in non-central high energy heavy ion collision.

### 1.3.3 Hydro dynamic model

Hydro-dynamic model is proposed to explain the large elliptic flow  $v_2$  with radial collective expansion of the system in heavy ion collision. It describes well the  $p_T$  dependence of  $v_2$  for  $\pi$ ,  $K$  and  $p$  in low  $p_T$  range ( $p_T < 1.5$  GeV/c). Thermalization at the initial stage (0.6 fm/c) of the collision and low viscosity (as perfect liquid) of the medium are assumed in this model[14, 15]. The good agreement between the model and the experimental result at low  $p_T$  (soft particles) indicates the  $v_2$  is generated in the initial stage of collision.

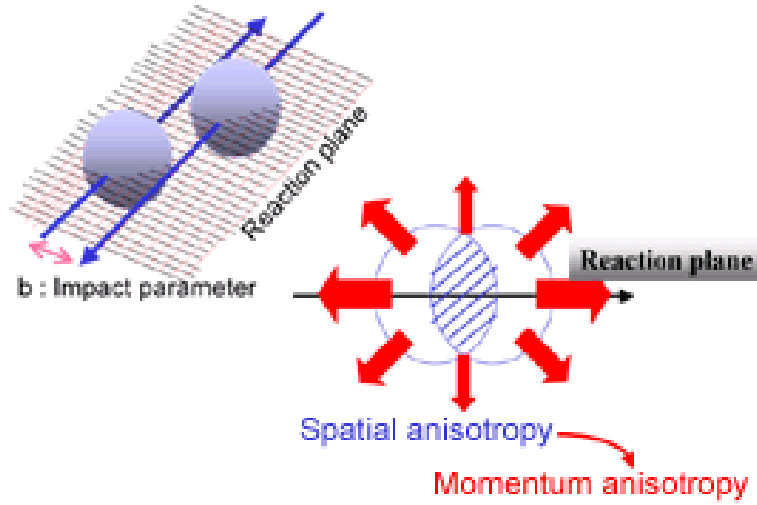


Figure 1.4: An image of a reaction plane of a heavy ion collision and azimuthal anisotropy of particle emission.

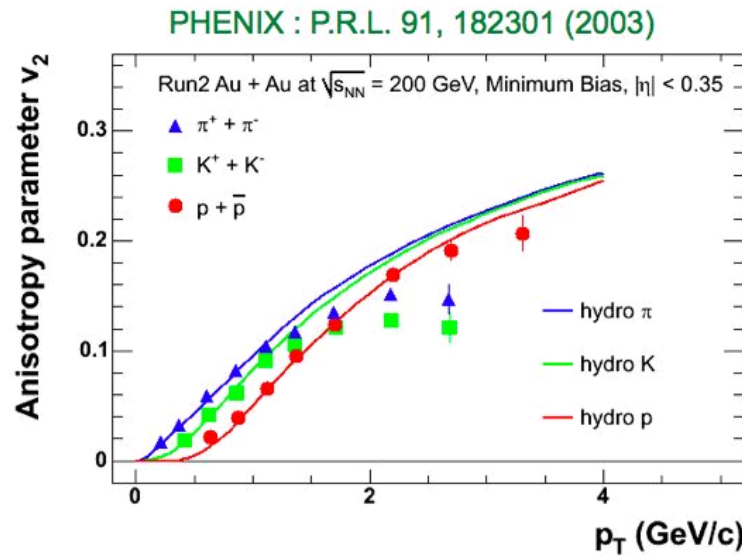


Figure 1.5: The  $v_2$  as a function of  $p_T$  of identified hadrons in  $\sqrt{s_{NN}} = 200$  GeV Au+Au collision in PHENIX-Run2 (2001)[15].

### 1.3.4 Blast-wave model parametrization

The blast-wave function is hydro-dynamic inspired parameterized function for expanding freeze-out system. The function of this model describes the transverse momentum spectra with parameters of freeze-out temperature and radial velocity of expansion[40].

$$\frac{dN}{p_T dp_T} = \int dr d\phi K_1(\beta) I_0(\alpha), \quad (1.11)$$

$$\alpha = \frac{p_T}{T} \sinh \rho = \frac{p_T}{T} \frac{e^\rho - e^{-\rho}}{2}, \quad (1.12)$$

$$\beta = \frac{m_T}{T} \cosh \rho = \frac{p_T}{T} \frac{e^\rho + e^{-\rho}}{2}, \quad (1.13)$$

$$\tanh \rho = \frac{r}{R_{max}} \beta_T, \quad (1.14)$$

where  $I_0$  is Bessel function of first kind,  $K_1$  is Bessel function of second kind,  $T$  is freeze-out temperature (GeV) and  $\beta_T$  is radial flow velocity. The density distribution is assumed to be constant and velocity profile is linear as a function of radius in the transverse directions in standard blast-wave model which fits the  $p_T$  spectra of identified hadrons in the heavy ion collision. Parameters of spatial anisotropy of density distribution of the system are added to extend this model to fit the  $v_2$  as a function of  $p_T$ . Especially, the eccentricity of density distribution is sensitive for the  $v_2$  fitting in the extended blast-wave model. Often, two elliptical parameters are defined as the eccentricity  $s_2$  of the density distribution and the eccentricity  $\beta_2$  of the expansion velocity as follows,

$$v_2 = \int dr d\phi K_1(\beta) I_2(\alpha) \cos(2\phi) (1 + 2s_2 \cos(2\phi)) / (dN p_T dp_T), \quad (1.15)$$

$$\alpha = \frac{p_T}{T} \sinh \rho = \frac{p_T}{T} \frac{e^\rho - e^{-\rho}}{2}, \quad (1.16)$$

$$\beta = \frac{m_T}{T} \cosh \rho = \frac{p_T}{T} \frac{e^\rho + e^{-\rho}}{2}, \quad (1.17)$$

$$\tanh \rho = \beta_T (1 + 2\beta_2 \cos 2\phi) \frac{r}{R_{max}}, \quad (1.18)$$

where  $\beta_2$  is the elliptical parameter of the expansion velocity and  $s_2$  is the elliptical parameter of density distribution. In this thesis, the initial density distribution  $W(r, \phi)$  is estimated with the overlap participant density of Glauber Monte Carlo with Wood-Saxon distribution collision picture. The gradient of the density distribution  $G(r, \phi)$  is calculated and used as the velocity profile of the expansion. Boost angle  $\phi_B$  which is direction of the gradient means direction of velocity. The Glauber distribution gives the initial collision geometry, but freeze-out density and velocity profiles are required in this blast-wave parameterized function. One free parameter  $A$  is added to estimate freeze-out eccentricity in the density distribution  $W'(x', y) = W(Ax, y)$  and velocity distribution  $G'(x', y)$  (Reaction Plane direction is  $y = 0$ ). The distributions expand to in-plane because the blast-wave model does not have sensitivity of size but eccentricity. These free parameters (freeze-out temperature, radial velocity and freeze-out eccentricity) can be extracted from elliptic flow and momentum spectra which are measured at PHENIX. The blast-wave function with glauber model with the eccentricity parameter is shown as following functions (see section5.3).

$$dNp_Tdp_T = \int dxdyW(Ax, y)K_1(\beta)I_0(\alpha), \quad (1.19)$$

$$v_2 = \int dxdyW(Ax, y)K_1(\beta)I_2(\alpha)\cos(2\phi_B)/(dNp_Tdp_T), \quad (1.20)$$

$$\alpha = \frac{p_T}{T} \sinh \rho = \frac{p_T}{T} \frac{e^\rho - e^{-\rho}}{2}, \quad (1.21)$$

$$\beta = \frac{m_T}{T} \cosh \rho = \frac{p_T}{T} \frac{e^\rho + e^{-\rho}}{2}, \quad (1.22)$$

$$\tanh \rho = \beta_T G(Ax, y). \quad (1.23)$$

### 1.3.5 Quark coalescence model

The quark coalescence model suggests mechanism of hadron generation at QGP-hadron phase transition. Baryon or meson are formed with two or three of quarks[16, 17]. The hadrons that are formed with two or three of quarks succeed the azimuthal anisotropy of quarks if the quarks have the anisotropy during the QGP phase in this model. The  $v_2$  of hadron are shown as follows,

$$v_2^{hadron}(p_T) = nv_2\left(\frac{p_T}{n}\right), \quad (1.24)$$

where  $n$  is the number of constituents quark in hadron. It is expected that  $v_2$  as a function of  $p_T$  of hadrons are scaled by the numbers of constituents quark in hadron. The  $v_2$  of some hadrons were measured and compared with the quark number scaling at RHIC. The  $v_2$  is shown as a function of  $KE_T$  ( $m_T - m_0$ ) in order to cancel or reduce the  $p_T$  shift given by the mass effect and compare the quark number dependency. The scaled  $v_2$  with the quark number  $v_2/n$  are consistent for measured hadrons at  $KE_T/n < 0.7$  GeV.

## 1.4 Thesis motivation

Experiment of high energy heavy ion collision has been performed to study QGP phase transition and behavior of parton in the hot dense matter at RHIC. Theoretically, the estimated energy density of collision area according to the Bjorken model ( $\sim 5$  GeV/fm $^3$ ) is higher than the critical energy density ( $\sim 1$  GeV/fm $^3$ ). Experimentally, the measurement of the azimuthal anisotropy is one of the most important probes to study the behavior of parton in the high energy heavy ion collision. Especially, the value of the elliptic flow  $v_2$  has an information of the initial state and the expansion behavior of the collision system. The large  $v_2$  is an indicator of the short mean free pass of partons in the hot dense medium. The measured  $v_2$  of identified hadrons have two interesting characteristics. The  $v_2$  increases with  $p_T$  and the rise of the  $v_2$  shifts towards higher  $p_T$  for heavier particles in the low momentum range ( $p_T < 2$  GeV/c). The hydrodynamics model with a low viscosity reproduced the collective behavior for the particles. The  $v_2$  of baryon ( $p$ ) is larger than that of meson ( $\pi$  and  $K$ ) at  $p_T = 2 - 3$  GeV/c. These are consistent with the number of constituents quark scaling and  $KE_T$  scaling. The quark number scaling indicates  $v_2$  is generated during QGP phase and hadrons are formed according to the quark coalescence model, where the  $v_2$  of the hadrons is inherited from the  $v_2$  of quarks. These are important clues to understand the hot dense matter as QGP. More hadrons should be compared as well as  $\pi$ ,  $K$  or  $p$  to obtain the conclusive evidence of the quark number scaling.

The indicator of the quark level flow is provided by the  $v_2$  of identified hadrons. However, the  $v_2$  of identified hadrons were measured at only low  $p_T$  of  $\pi$ ,  $K$  and  $p$ . It is necessary to measure many species of hadrons to discuss for quark flow in detail. The  $v_2$  of identified hadrons in high  $p_T$  ( $> 3$  GeV/c) (hard particles are dominant) range are interesting, too. But, the measurement of  $v_2$  has been limited by poor resolution of reaction plane at RHIC-PHENIX. The  $v_2$  is measured with the  $\Delta\phi$  distribution of particles with respect to the event plane (the measured reaction plane) angle. The accuracy of the  $v_2$  measurement is given by statistics of the identified particles of interest and the resolution of the event plane determination. In 2007, a new reaction plane detector (RxP) was installed and the  $v_2$  was measured with two times better resolution compared to the one measured before in Au+Au  $\sqrt{s_{NN}} = 200$  GeV collision at RHIC-PHENIX. It allows us to study  $v_2$  of the rare particles, at high transverse momentum  $p_T > 3$  GeV/c or at low energy collisions.

In this paper, the  $v_2$  of the following rare particles is measured and presented with the  $v_2$  of  $\pi$ ,  $K$  and  $p$ .  $\phi$  is important because it is not only a heavy mass meson (the mass is similar to  $p$  even though it consists of two quarks), but also the hadronic re-scattering cross-section is smaller than baryon[18]. It is expected that the  $v_2$  of  $\phi$  is generated before the QGP-hadron phase transition and less affected from the hadronic re-scattering after the QGP-hadron phase transition. It is expected the  $d$  is formed at final stage since the weak binding energy between nucleons rather than quarks in hadron. The  $v_2$  of  $d$  should be larger than the  $v_2$  of baryon if the quark coalescence model holds at high  $p_T$  range. The  $v_2$  of  $\Lambda$  should be similar to the  $v_2$  of  $p$  because they are baryons and have similar mass.

The blast-wave function which is parameterized function for  $p_T$  spectra of identified particles is extended for  $v_2$  as a function of  $p_T$  with elliptical factors of density distribution and velocity of expansion. Although four free parameters ( $T_f$ ,  $\beta_t$ ,  $s_2$  and  $\beta_2$ ) are usually used for blast-wave fitting of  $v_2$ , the density distribution is estimated with number of participant distribution from Glauber Monte Carlo with Wood-Saxon distribution and the velocity of expansion is estimated as gradient of the number of participant distribution. One free parameter is added to estimate eccentricity of dense matter at freeze-out timing in this participant distribution. The result of new method is compared with result of HBT and helps understanding of the history of quark matter expansion.

The study of  $v_2$  at low energy heavy ion collision may provide information about threshold behavior of collision energy, if the quark number dependency is an indicator of a QGP phase. In 2010, the  $v_2$  is measured in  $\sqrt{s_{NN}} = 62$  and  $39$  GeV Au+Au collision, too. The resolutions for the low energy collisions are reduced because the multiplicity is smaller than that of  $\sqrt{s_{NN}} = 200$  GeV collision, however the influence to flow analysis with the high resolution event plane from RxP is minor than the other detectors. The  $v_2$  of low energy collision are measured and compared with 200 GeV collision for  $\pi^+$ ,  $\pi^-$ ,  $K^+$ ,  $K^-$ ,  $p$ ,  $\bar{p}$  and  $d$  at minimum bias range of centrality. The results of  $v_2$  at three collision energies (200, 62 and 39 GeV) are compared to search for a threshold behavior in QGP phase transition as a function of collision energy.

# Chapter 2

# Experiment

## 2.1 Relativistic Heavy Ion Collider

Relativistic Heavy Ion Collider is an intersecting storage ring particle accelerator which has two independent rings. It can accelerate (100 GeV per nucleon for Au, 250 GeV for proton) and collide variety of particle species. It means the maximum collision energy is  $\sqrt{s_{NN}} = 200$  GeV for Au+Au ( $\sqrt{s} = 500$  GeV for pp). These were performed since 2000 to 2013 and U+U and Cu+Au collisions are also provided in 2012. The current average luminosity of the collider is  $20 \times 10^{26} \text{ cm}^{-2}\text{s}^{-1}$

Ions are accelerated to 1 MeV per nucleon by Tandem Van de Graff accelerator at first. Au ions have electric charge of +31 after electron stripped. they are accelerated to 95 MeV per nucleon by the Booster Synchrotron. The charge value has been +77. They are accelerated to 8.86 GeV per nucleon and +79 charge by the Alternating Gradient Synchrotron (AGS) after that. Finally, they are transferred into the RHIC storage ring.

RHIC ring is hexagonal and has six collision points. Four experiments have been carried out or are working at RHIC. STAR has large acceptance ( $2\pi$  of  $\phi$  angle) for solid angle. PHOBOS had the largest pseudo-rapidity coverage. BRAHMS was designed for momentum spectroscopy. PHENIX aim identified rare or high momentum particles by good triggering capabilities.

## 2.2 Detectors of PHENIX experiment

PHENIX is one of large experiment groups at RHIC. PHENIX detector is designed to measure identified hadrons, muons, electrons or photons at high momentum. It consists of many sub system detectors.

Global detectors include BBC and ZDC characterize the nature of an event. Beam-Beam Counter (BBC) is used as trigger counter. It can measure z-position of collision point of beam line and centrality which is estimated by multiplicity. They provide a basic event selection at PHENIX analysis. BBC provides collision time to measure time of flight, too[19]. BBC can measure reaction plane, but it does not have good enough resolution. RxP was installed to measure reaction plane with high resolution in 2007. Zero Degree Counter (ZDC) detects neutron from the spectator[20].

The central arm spectrometer is mainly used for tracking and identifying particles which have mid rapidity acceptance (pseudo rapidity  $\eta < 0.35$ ). An east arm and a west arm are located on both sides of the beam line. Drift Chambers (DC) track charged particles and measure momentum of



Figure 2.1: Aerial photography of BNL

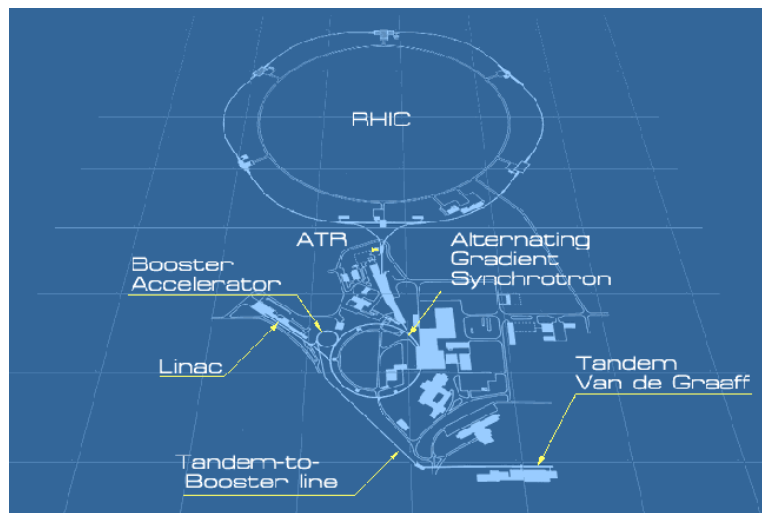


Figure 2.2: BNL collider map

that in a magnetic field. The magnetic field is supplied by the central magnet. It provides an axial field parallel to the beam direction. Particle mass can be estimated by the momentum and time of flight which is measured by Time Of Flight East (TOF.E), Time Of Flight West (TOF.W) or Lead Scintillator (PbSc). Aerogel Cerenkov counter reinforces the particle identification at especially high momentum. PbGl (Lead Glass) and PbSc have a good energy resolution for electrons and photons. Ring Image Cerenkov counter (RICH) identifies electron. Pad chambers (PC1, PC2 and PC3) provide background rejection by matching of tracking system.

Muon arms detect muons from  $J/\Psi$  decay. The Rapidity acceptance is  $1.15 < y < 2.44$ . The muon tracker (MuTr) consists of three stations of multi-plane drift chambers that provide precision tracking. The muon identifier (MuID) consists of alternating layers of steel absorbers and low resolution tracking layers of streamer tubes of the Iarocci type. The pion contamination of identified muon is typically  $3 \times 10^{-3}$ [21].

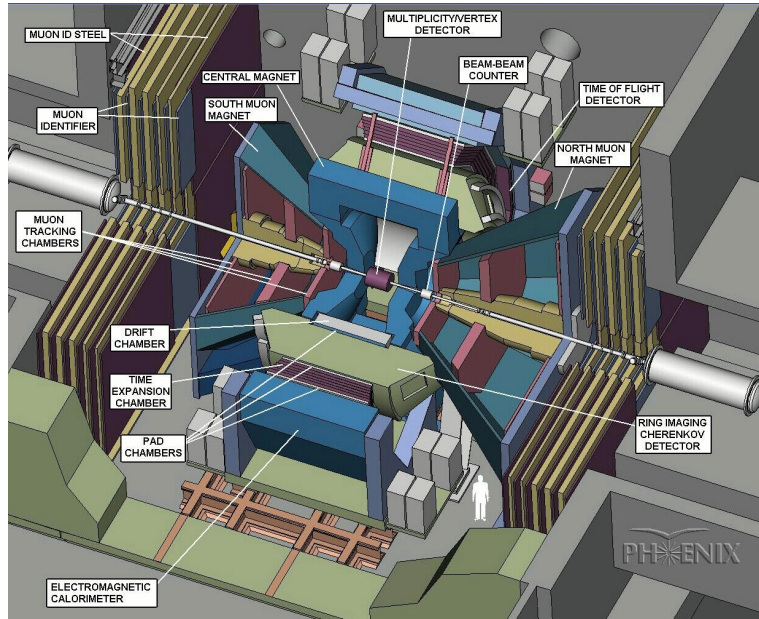


Figure 2.3: PHENIX all views in 2000

### 2.2.1 Beam-Beam Counter

A pair of Beam-Beam counter (BBC) is located at 1.44 m (and -1.44 m) from center of collision point. Each one consists of 64 modules of Cerenkov counter which located around beam line. They cover forward rapidity ( $\eta = 3.0 - 3.9$ ). R6178 PMTs (1 inch, mesh-dynode type) with 3 cm of fused quartz radiator are used for each Cerenkov counter module. They work on high radioactive and high magnetic field. Wide dynamic range detects hits of 1 to 30 of minimum ionization particles (MIP) which are expected for one Cerenkov counter module for  $pp$  or  $Au + Au$  central collision. Centrality of  $Au + Au$  collision can be estimated with BBC charge which is in proportion to number of MIP. Reaction plane can be estimated by  $\phi$  angle distribution of the charge, too. The fast responsible PMT and Time to Voltage Converter (TVC) provide high resolution (44ps) to measure collision timing. Collision time is estimated by average of arrival time of the charged particles between BBC

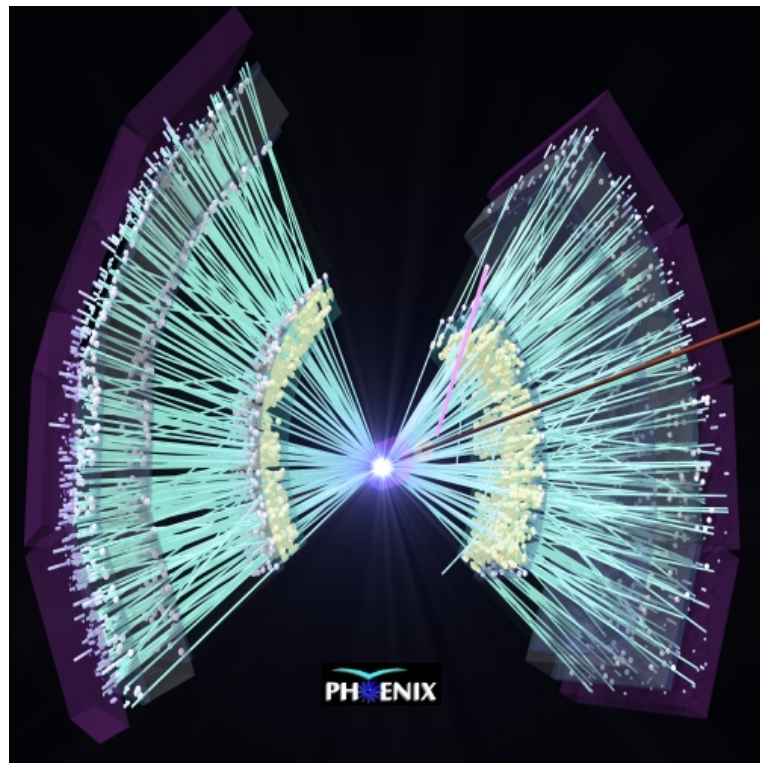


Figure 2.4: PHENIX tracking view of hit particles.

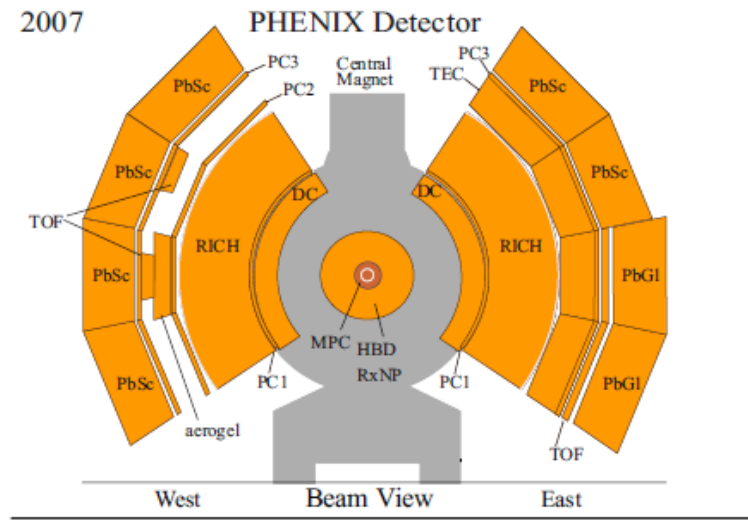


Figure 2.5: PHENIX beam view in 2007

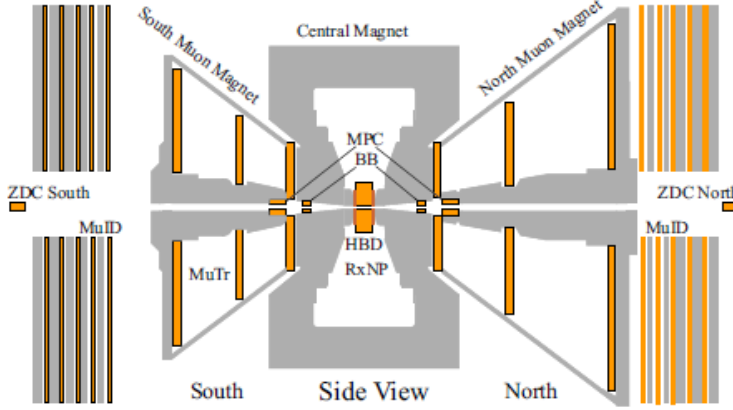


Figure 2.6: PHENIX side view in 2007

South and BBC North that is used as the start time of TOF measurement. Vertex position on beam line is estimated the difference of the arrival time between BBC south and BBC north as follows,

$$T_{col} = (T_{BBCS} + T_{BBCN})/2, \quad (2.1)$$

$$Z_{vtx} = c(T_{BBCS} - T_{BBCN})/2, \quad (2.2)$$

where  $T_{BBCS}$  or  $T_{BBCN}$  is the mean value of arrival time of particles for each module. BBC has timing resolution of 40 ps and Z-vertex resolution of 0.6 cm. BBC provides the main trigger for many PHENIX detectors and various analysis.

### 2.2.2 Zero Degree Calorimeter

Zero Degree Calorimeter (ZDC) covers forward rapidity ( $\eta < 6.0$ ). A pair of ZDC is located 18 m (and  $-18$  m) from center of collision point. ZDC is the hadron calorimeter to detect neutrons of fragmented participants of heavy ion collision. Charged particles are rejected because ZDC is located behind DX dipole magnet. ZDC consists of three modules of tungsten alloy plates and ribbons of commercial optical fibers in a sampling layer. The ZDC charge that has negative correlation with BBC charge shows the number of fragmented neutrons in collision. It means ZDC detect signal from the spectator. It is important that the measured collision geometries between by participant and by spectator are consistent. ZDC can estimate collision time and vertex position same as BBC. The timing resolution is 150 ps and z-vertex resolution is 2.5 cm. It can measure reaction plane as a directed first order plane with information from spectator that have less non-flow (jet) correlation than event plane from participant region.

### 2.2.3 Muon Piston Chamber

Muon Piston Chamber (MPC) was installed in 2007. Although MPC covers same rapidity acceptance as BBC, it has better resolution of the reaction plane than BBC because the reaction plane can be weighted by energy measurement from MPC. The each segment of MPC is electromagnetic calorimeter with PbWO<sub>4</sub> scintillator crystals[22].

#### 2.2.4 PHENIX magnet

The PHENIX magnet system is composed of three spectrometer magnets, Central Magnet (CM) and Muon Magnets (MMN and MMS), with warm iron yokes and water-cooled copper coils. The CM provides a magnetic field around the collision point with two pairs of concentric coils. The strength is 0.75 T for PHENIX-Run7 (2007) at the collision point. It's a component parallel to the beam axis has an approximately Gaussian dependence on the radial distance from the beam axis, dropping from 0.48 T at the center to 0.096 T (0.048 T) at the inner (outer) radius of DC[23]. A charged particle which is emitted from the collision bend into a perpendicular direction to both of magnetic line and trajectory of its own by the magnetic field according to Lorentz law. The bending angle  $R$  is estimated with crossing angle between track and DC surface  $\phi$  is measured to estimate momentum.

#### 2.2.5 Drift Chamber

One Drift Chamber (DC) has a quarter round for  $\phi$  angle from collision point and 1.8 m long along the beam direction. A pair of DC is located at 2 - 2.5 m distance from beam line. DC measures pending angle of charged particles in a magnetic field. Momentum is estimated by the pending angle in PHENIX. And DC provides tracking information to link through other subsystem detectors of Central arm.

DC consists of six types of wire planes they are stacked radially and called X1, U1, V1, X2, U2, V2. Each plane consists of four anodes and four cathode wire nets. Cathode net consists only of cathode wires. X1 and X2 are in parallel to the beam to measure track in  $\phi$  angle. U and V are inclined at a small angle (-5 or 5) to measure Z-position for full three-dimensional track reconstruction. They work in a gas mixture of 50 % of Ar and 50 % of C2H5.

DC has 99 % of track finding efficiency for high multiplicity of Au+Au collision, 1 mrad of angular resolution and spatial resolution in the z direction better than 2 mm.

#### 2.2.6 Pad Chamber

Pad chambers (PC) are multi-wire proportional chambers[24]. Each layer contains a single plane of wires inside a gas volume bounded by two cathode planes. One cathode is nearly segmented into an array of pixels. Nine pixels are connected together electronically to form a pad. The size of pixel cell is  $0.84 \times 0.84 \text{ cm}^2$ .

Three layers (PC1, PC2, and PC3) are on each central arm (PC2 is only in the west arm). PC1 is located between the DC and RICH (2.5 m from beam line) on the east arm and the west arm. This provides a Z position resolution of 1.7 mm and  $r - \phi$  resolution of 2.5 mm. PC1 measures the three-dimensional momentum vector of charged particles at the surface of the DC. DC and PC1 provide track reconstruction at first at PHENIX. PC2 behind the RICH is only in west arm. PC3 is in front of EMC in the east arm and the west arm. PC2 and PC3 have the Z position resolution of 3.1 mm, and 3.6 mm. They can reject background track that is generated at outside of DC or PC1. Expected hit position of Z axis and through angle of  $\phi$  for each track on each detector (PC2, PC3) are calculated with DC and PC1 information and they compared with measured values with each detector.

### 2.2.7 Time Of Flight

Time Of Flight East (TOF.E) and West (TOF.W) measured hit timing of charged particles. The flight time and flight length of a charged particle to TOF from the collision point provide mass of the particle is as follows,

$$m^2 = p^2(T^2/L^2) - 1, \quad (2.3)$$

where  $m$  is mass of particle,  $p$  is momentum,  $L$  is the flight path length and  $T$  is flight time. The flight length is estimated by DC information although TOF is located at a radial distance of 5 m from the interaction point since charged particle bends in a magnetic field.

TOF.E is in the east arm and TOF.W is in the west arm. TOF.E consists of plastic scintillation counter module of 960 slats. Scintillator which is 637.7 or 433.9 mm of length has two PMTs at both sides. TOF.E has been used from the beginning of PHENIX and the time resolution is about 110 ps. TOF.W was installed in 2007 and the resolution is 90 ps. TOF.W consists of Multi-Gap Resistive Plate Chamber (MRPC) module of 128. The half of TOF.W and ACC acceptances overlap. It provides not only an increased time of flight acceptance, but cooperation of TOF.W and ACC provides particle identification at higher  $p_T$  range.

### 2.2.8 Aerogel Cerenkov Counter

Aerogel Cerenkov Counter (ACC) consists of 160 cells. Each cell has Cerenkov radiator and two PMTs. Silica aerogel which have a refractive index of  $n=1.011$  is used. The volume of the cell is (22cm  $\times$  11cm  $\times$  12cm), and they are stacked into an array of 10 cells for  $\phi$  and 16 cells in  $z$  direction. ACC located at 4.5 m from the beam line which is between PC2 and PC3 in the west central arm. The acceptance of  $4 \text{ m}^2$  for the area and of 0.7 for  $\eta$ . This overlaps with a half of TOF.W acceptance. They provide particle identification for charged particle at wide  $p_T$  range. Cerenkov photons are emitted from charged particle when the particle moves faster than the speed of light in a material. Particle emits Cerenkov photons so as to be light mass at a momentum range. The threshold energy  $E$  for the emission of Cerenkov radiation is as follows,

$$E = \frac{nm}{\sqrt{n^2 - 1}}. \quad (2.4)$$

where  $m$  is particle mass and  $n$  is the refractive index of the medium.

### 2.2.9 Lead Scintillator Electromagnetic Calorimeter

Electromagnetic Calorimeter (EMC) has 8 sectors on central arm. Six of them (all of the west arm and two of the east arm) are Lead-Scintillator type (PbSc) which is shashlik type sampling calorimeters and two of them (two of the east arm) are Lead-Glass type (PbGl) which is Cerenkov detector.

PbSc has 15552 of lead and scintillator towers. The tower consists of 66 cell sampling consisting of alternating tiles of Pb and scintillator. These cells are optically connected by 36 fibers and light is corrected to PMT which located at the back of the towers. A module consists of four towers which are mechanically brought together. One sector consists of 18 super modules and one super module consists of 36 modules[25].

PbGl sector consists of 192 super-modules and One super-module consists of 24 modules. PbGl consists of 9216 modules. The system worked in WA98 experiment at CERN[26]. Both of two

types have good energy resolution. EMC measures the energy and spatial position of photon and electron with RICH. In addition, PbSc has timing resolution of 400 ps. Because PbSc and TOF.E do not overlap, they have maximum acceptance for hadron PID in PHENIX. They are useful when identified two particles correlation analysis or particle detection by invariant mass method although the resolution of PbSc is lower than TOF.

### 2.2.10 Ring Image Cerenkov Counter

Ring Image Cerenkov Counter (RICH) and EMC identify electron. Each RICH module has a volume of  $40 \text{ m}^3$  which has an entrance window area of  $8.9 \text{ m}^2$  and an exit window area of  $21.6 \text{ m}^2$ . Cone of the Cerenkov photons is emitted when charged particle traverses a medium if the velocity greater than the speed of light in the medium. The photon emission angle from track trajectory is shown as follows,

$$\cos \theta = \frac{1}{\beta n}, \quad (2.5)$$

where  $n$  is the refractive index of the medium. The photon of the cone is detected on a position sensitive planar photon detector of RICH, which allows reconstructing the ring images. Each detector consists of 48 composite mirror panels which are formed two intersecting spherical surfaces. The reflecting area totaled  $20 \text{ m}^2$ . The reflectivity of the mirrors is 83 % at 200 nm or 90 % at 250 nm. The photons are collected by the spherical mirror and focused onto the PMT placed at the focal plane. They formed a circle with radius  $r = f\theta$  that independent of the emission point along the particle track. Where  $f$  is the focal length of the intersecting spherical surfaces. CO2 ( $n = 1.000410$ ) was used as the Cerenkov radiator and the  $r$  is 5.9 cm. PMT (H3171S) is located on either side of the RICH entrance window. It has two diameter Winston cones and magnetic shields. UV glass windows of PMT absorb photons of wavelengths below 200 nm.

### 2.2.11 New Reaction Plane Detector (RxP)

Reaction Plane Detector (RxP) was installed in 2007 to measure reaction plane. Poor resolution is limiting factor of  $v_2$  measurement. BBC can measure reaction plane, but the resolution is not so good. RxP has two times better resolution than that of BBC. This high resolution allows study of elliptic flow for rare particles which are *deuteron*,  $\phi$ -meson or high  $p_T$  hadron in PHENIX.

This detector upgrade is an important key point for the analysis of this paper. See next chapter for detail of the development of RxP.

# Chapter 3

## Reaction Plane Detector



Figure 3.1: Sensitive parts of RxP and beam pipe of PHENIX.

### 3.1 Reaction Plane determination for flow analysis

Event anisotropy is one of the most important studies in heavy ion collision. Large azimuthal anisotropy was observed and that provides evidence of formation of high density partonic medium in Au+Au  $\sqrt{s_{NN}} = 200$  GeV collision at RHIC.

Elliptical azimuthal anisotropy ( $v_2$ ) is measured by  $\Delta\phi$  (particle emission angle) distribution from reaction plane. Reaction plane and particle distribution in azimuthal angle, so the peak (averaged direction) of the distribution is taken as the reaction plane ( $-\frac{\pi}{2}$  to  $\frac{\pi}{2}$ ). And  $v_2$  means amplitude of the peak (the second term of the Fourier series). Particles must not be used to measure both of reaction plane angle and  $v_2$ . Auto correlation effect is a large bias on  $v_2$  measurement, although we want to know “flow  $v_2$ ”. Therefore, detectors which measure them have another

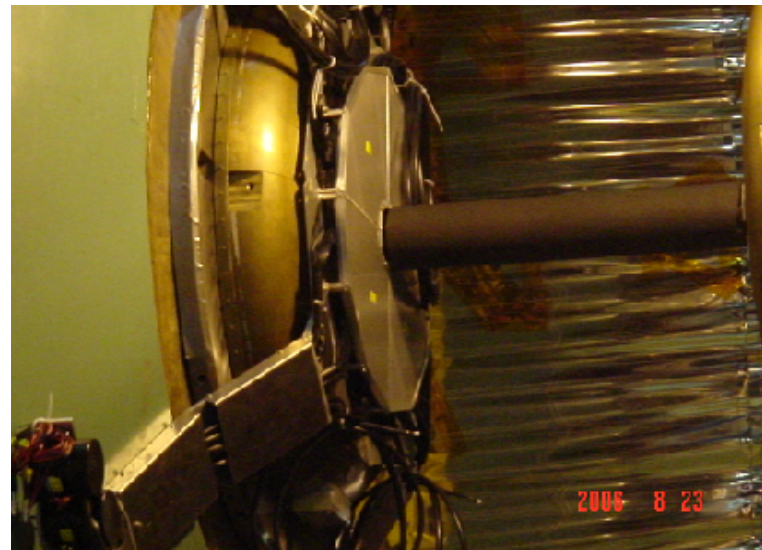


Figure 3.2: One side photo of RxP.

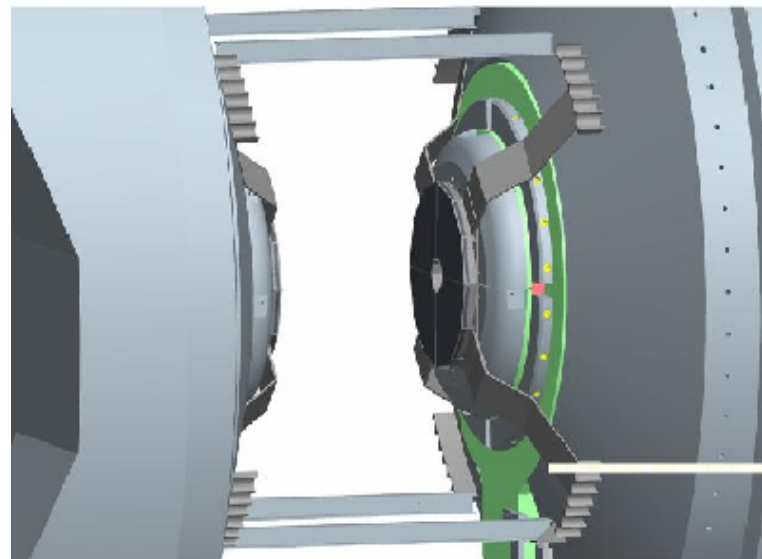


Figure 3.3: Schematic figure of RxP detector.

acceptance. (It often means a different  $\eta$  acceptance.)

## 3.2 Reaction Plane resolution

Measurements of the  $v_2$  of rare particles are limited by statistics of 2 types. These are the statistics of the identified particles and the reaction plane resolution. The reaction plane resolution is estimated with a distribution of  $\Delta\Phi$  which is the difference between the measured event plane  $\Phi$  and the reaction plane  $\Psi$  of each event ( $\Delta\Phi = \Phi - \Psi$ ). The observed  $v_2$  is reduced by intrinsic event plane resolution by a detector. The relation between the observed  $v_2^{observe}$  and the corrected  $v_2^{real}$  is as follows,

$$v_2^{observe} = v_2^{real} \times \langle \cos(2\Delta\Phi) \rangle. \quad (3.1)$$

The observed  $v_2$  is corrected by the correction factor  $\langle \cos 2\Delta\Phi \rangle$ . This correction factor is called reaction plane resolution. The ideal value is 1. And 0 of that means no resolution for reaction plane. Estimation of the reaction plane resolution and correction with that provide  $v_2^{real}$ . However, the correction increases the statistical error of the  $v_2$  measurement. The formula of  $v_2$  error shows that the error in the  $v_2$  is amplified by a factor of inverse resolution. The statistical value of the measurement is reduced by a factor of  $(\frac{1}{\cos 2\Delta\Phi})^2$  due to the reaction plane resolution.

## 3.3 Reaction plane measurement in PHENIX

BBC was used to determine reaction plane for  $v_2$  analysis. The reaction plane resolution of BBC is 0.4 at maximum. It means the observed  $v_2$  value is only 40 % of real  $v_2$  at maximum. This poor reaction plane resolution was a major limiting factor of  $v_2$  measurement of rare signals in PHENIX experiment.

## 3.4 Geant4 simulation and construction of RxP

The new reaction plane detector (RxP) was installed in PHENIX experiment in autumn of 2006. Figure 3.1 and 3.2 show the RxP detector immediately just after the installation. It is just before PHENIX-Run7 (9 Jan 2007 - 3 Jul 2007) PHENIX consisted of many detectors already. Therefore a geometry of RxP was limited. It has been required for the reaction plane detector to satisfy the following three points. It has to have an acceptance outside of central arm spectrometer ( $\eta < 0.35$ ) where  $v_2$  of the particle of interest are measured. It has to have azimuthal (around beam line) sensitivity part to measure the  $\phi$ -angle distribution of particle emission. It has to be closer to the collision point so that small sensitive area can cover large angle acceptance. To meet these requirements, RxP was positioned at  $z = 35$  cm from the collision point inside the magnetic field and the thickness is 5 cm. It has acceptance of  $\phi = 2\pi$  and  $\eta = 1.5 - 2.8$ .

RxP measures particle number distribution as energy loss. The sensitive part is divided by some  $\phi$ -angle segments to measure the energy deposit which is in proportional to the number of particles in each  $\phi$ -angle segment. Figure 3.6 and 3.7 show the  $\eta$  acceptance ranges of new/old reaction plane detectors with multiplicity and  $v_2$  of Au+Au  $\sqrt{s_{NN}} = 200$  which mean the particle statistics and the signal magnitude for reaction plane measurement.

The magnetic field at the collision point reaches to about 1 T. High magnetic field is known to deteriorate the performance of PMT, therefore a fine mesh PMT (R5924) was adopted, since it's

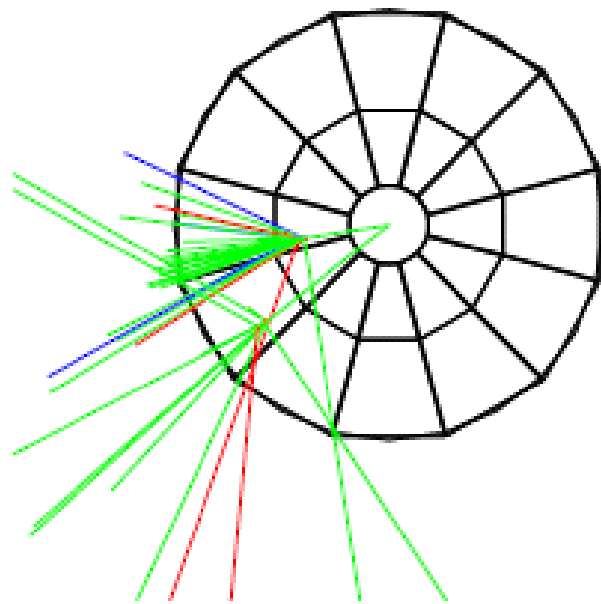


Figure 3.4: GEANT4 simulation of RxP (1)

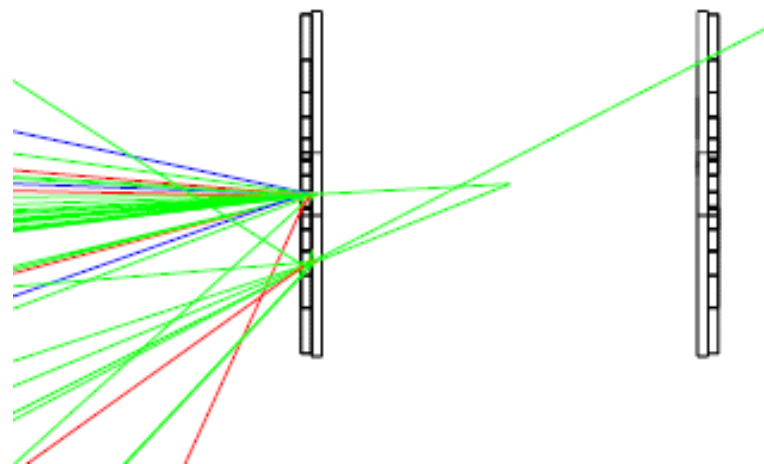


Figure 3.5: GEANT4 simulation of RxP (2)

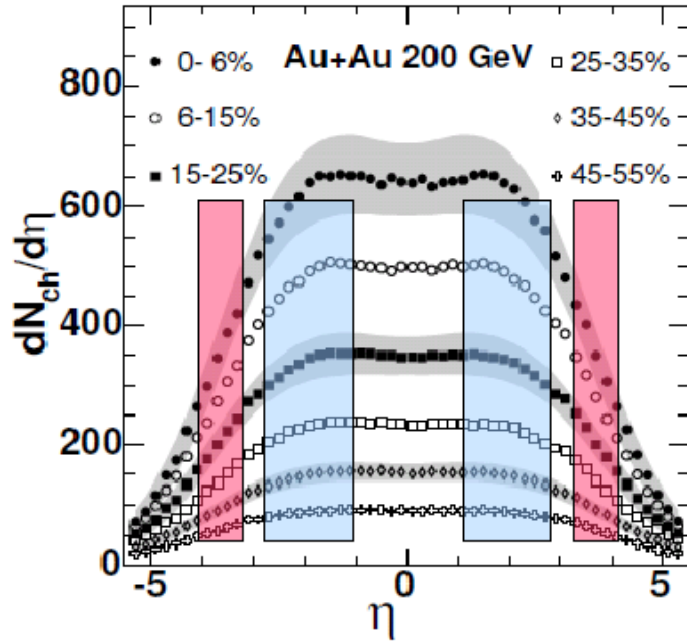


Figure 3.6:  $dN/d\eta$  as a function of  $\eta$  in Au+Au  $\sqrt{s_{NN}} = 200$  GeV in PHOBOS[27]. Blue band shows  $\eta$  acceptance of RxP. Red band shows  $\eta$  acceptance of BBC.

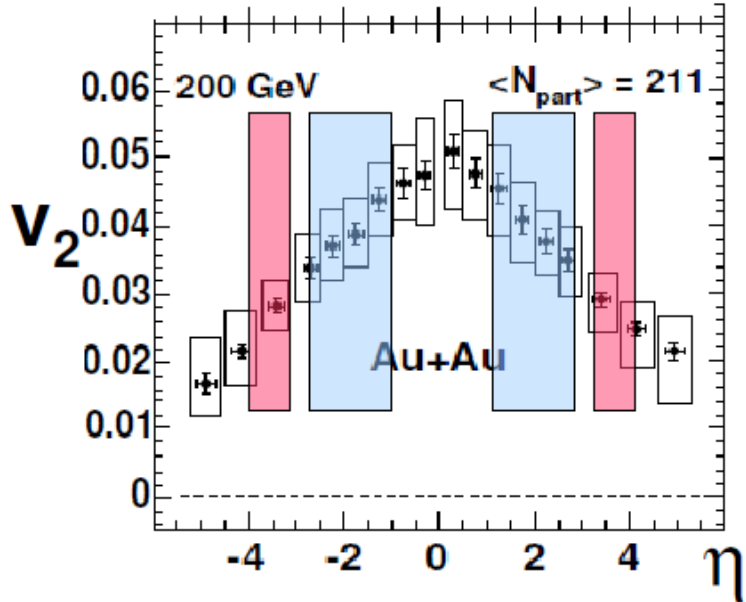


Figure 3.7:  $v_2$  as a function of  $\eta$  in Au+Au  $\sqrt{s_{NN}} = 200$  GeV in PHOBOS[28]. Blue band shows  $\eta$  acceptance of RxP. Red band shows  $\eta$  acceptance of BBC.

less affected in high magnetic field. It works under magnetic field of 0.35 T (fig.3.8). Long light guide (150 cm) was adopted to keep PMT away from the center of the magnetic field.

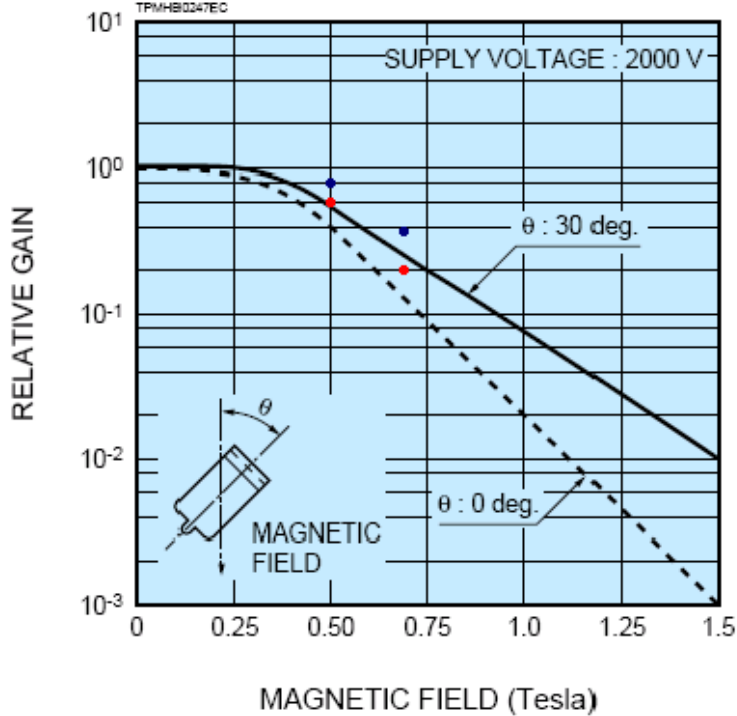


Figure 3.8: Fine mesh PMT output in magnetic field[29]. Red and blue points show results of test measurement for each sample.

Some prototypes of the detector were examined at KEK-ps accelerator facility. Figure 3.9 shows the setup for the test beam experiment. Figure 3.10 shows the prototypes of the detector. A scintillator (BC412) for scintillation counter and an acrylic material for Cerenkov counter were tested and compared. Optical fiber and acrylic were tested for the light guide. As a result, adoption of the scintillation counter with the fiber light guide has been used for the final design. The fiber light guide reduces hit position dependence of the signal pulse height of the charged particle. Fibers (BCF92 and Y11) were embedded into the scintillator every 0.5 cm.

“PCF92 Bycron”  
 Emission Peak 492 nm  
 Decay time 2.7 ns  
 $1/e$  length  $> 3.5$

“Y11 Kuraray”  
 Emission Peak 476 nm  
 Att. Leng.  $> 3.5$

Figure 3.11 shows the result of the test experiment. The acrylic light guide has a higher yield of photon than fiber, but the hit position dependence is large. Cerenkov counter with fiber light guide has too small signal because the number of Cerenkov photons is much less than that of scintillation photons.

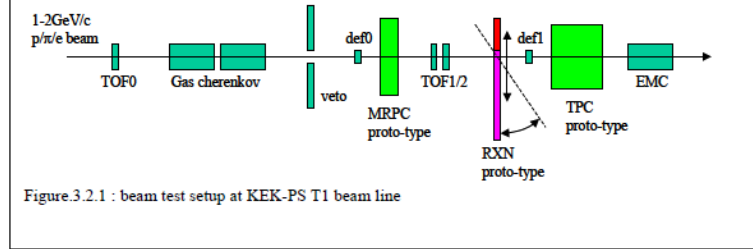


Figure 3.9: RxP test setup in KEK

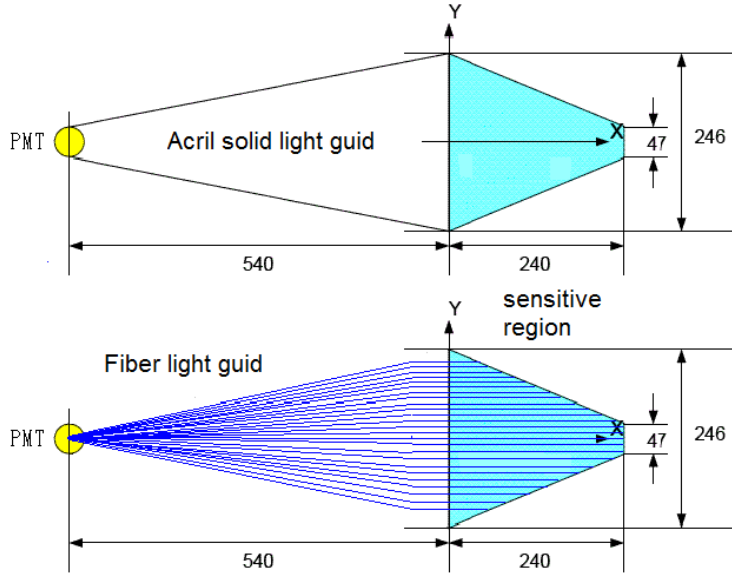


Figure 3.10: RxP proto types in KEK test

Lead converter amplifies the number of charged particles in the active material. The limit for the thickness of full detector material was 4 cm except aluminum flames (5 cm of total of RxP). The energy deposit of charged particles has a large Landau fluctuation with thin scintillator. Lead converter was used to amplify the number of charged particles and to reduce the effective fluctuation of energy deposit. Charged  $\pi$ -mesons are dominant with no converter, but decay photons from  $\pi^0$  decay are dominant with converter. The total number of charged particles is amplified to about 10 times by EM shower.

The optimum thickness of the converter and scintillator as well as optimum number of segmentations were estimated by GEANT simulation. As a result, 2 cm of the scintillator was divided into

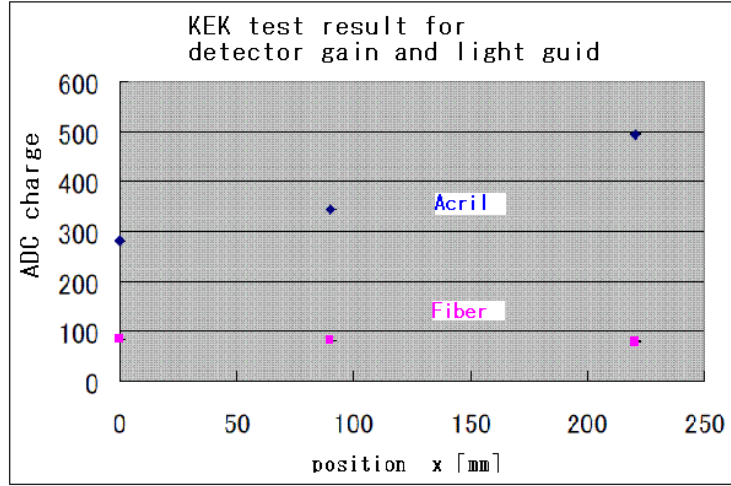


Figure 3.11: Hit position dependent of PMT outotput. Horizontal axis shows x-position from left edge of sensitive area on Fig.3.10

12 segments along the  $\phi$ -angle (and 2 cm of the lead converters in front of the scintillators). Figure 3.3 shows a schematic figure of RxP. Figure 3.4 and 3.5 show event displays of 1 GeV/c  $\pi^0$  with RxP in the GEANT simulation. Figure 3.12 and 3.13 show the result of the simulation to optimize the thickness of scintillator and converter.

In order to understand and actually measure the auto correlation effect, the event plane is determined in different  $\eta$  acceptances away from central arm detectors, which measures  $v_2$  of the particle of interest. In addition, jet correlation effect may influence  $v_2$  measurement because the jet is defined to have many high momentum particles in a similar direction within a small cone. The measured  $v_2$  would be biased, when one particle in the jet hits the  $v_2$  detector and another particle in the same jet hits the reaction plane detector, even if the jet direction has no correlation to the reaction plane. The larger rapidity gap is needed in order to remove this bias completely. The bias of  $v_2$  measurement of PHENIX was simulated by HIJING and PYTHIA. It was assumed that the kinematic property of jet in the heavy ion collisions (Au+Au  $\sqrt{s_{NN}} = 200$  GeV) is same as proton collision (p+p  $\sqrt{s_{NN}} = 200$  GeV) because jet property in heavy ion collisions is still under study[30].

As the simulation result (Fig.3.14), no bias in  $v_2$  is found for the particle measured at  $\eta < 0.35$  when the reaction plane is measured at  $\eta = 1.5 - 2.8$ . Based on that simulation results, RxP was divided at  $\eta = 1.5$  between inner ring ( $\eta = 1.5 - 2.8$ ) and outer ring ( $\eta = 1.0 - 1.5$ ). The bias by jet seems to be stronger in peripheral collision events because the jet pair ratio over the combinatorial pair is higher than that of the central collision event. Acceptance has been divided in order for us to be able to study the  $v_2$  bias and to compare the  $v_2$  values between the RxP inner and the RxP outer reaction planes.

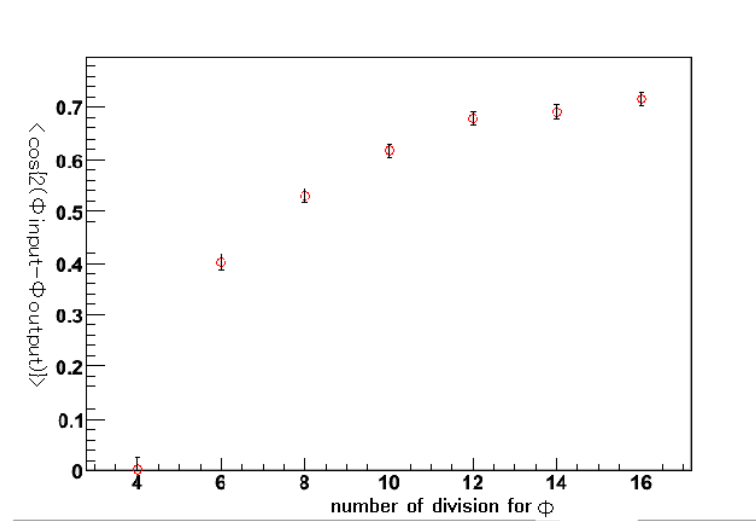


Figure 3.12: Reaction plane resolution as a function of  $\phi$ -angle division of scintillator of RxP in GEANT simulation.

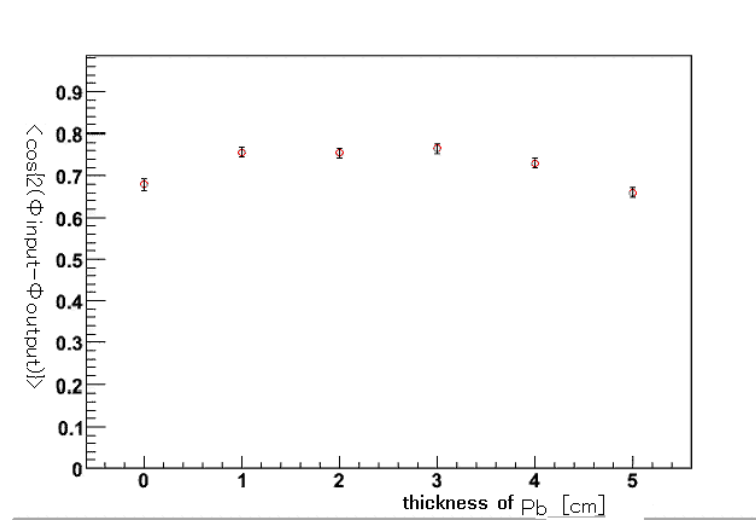


Figure 3.13: Reaction plane resolution as a function of lead converter thickness of RxP in GEANT simulation.

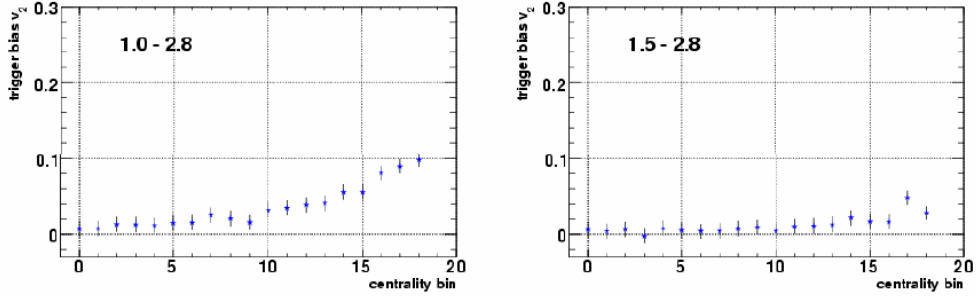


Figure 3.14:  $v_2$  bias of jet-correlation ( $\Delta v2$ ) as a function of centrality. Left panel shows that with reaction plane detector of  $\eta = 1.0 - 2.8$ . Right panel shows that with reaction plane detector of  $\eta = 1.5 - 2.8$ .

### 3.5 Resolution of RxP in PHENIX-Run7 (2007)

RxP worked very well during the PHENIX Run7 period and demonstrated the design performance[31]. As a result of this upgrade, reaction plane resolution of 0.75 is achieved for Au+Au  $\sqrt{s_{NN}} = 200$  GeV collision. It means the reaction plane resolution improves by a factor of two. It is equivalent with four times statistics for  $v_2$  measurement. This allows us to improve the precision of the measurements of azimuthal anisotropy ( $v_2$ ) for high  $p_T$  identified hadrons up to  $p_T$  of 6 GeV/c. Figure 3.15 - 3.22 show the final design and photos of RxP detector.

Table 3.1: RxP operation periods

Run	beam	start	end
7	AuAu	9 Jan 2007	3 Jul 2007
8	dAu, pp	6 Nov 2007	18 Mar 2008
9	pp	27 Jun 2009	7 Jul 2009
10	AuAu	1 Dec 2009	15 Jun 2010



Figure 3.15: Photo of a flame part of RxP

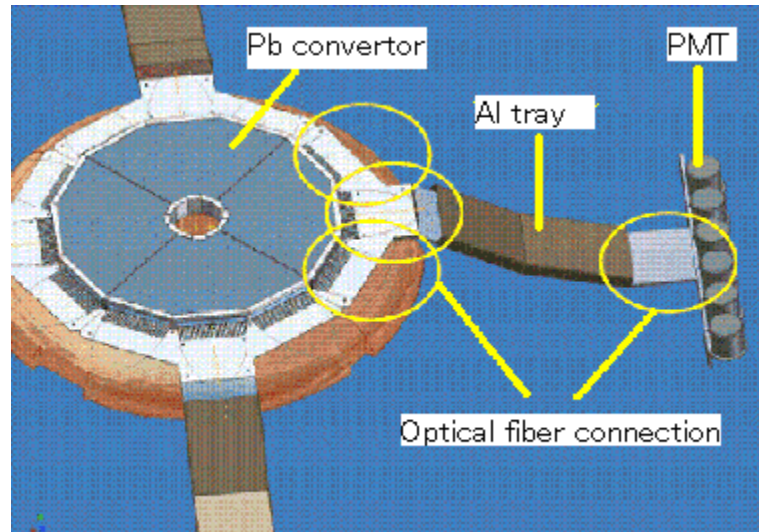


Figure 3.16: Picture of light guide connection of RxP.

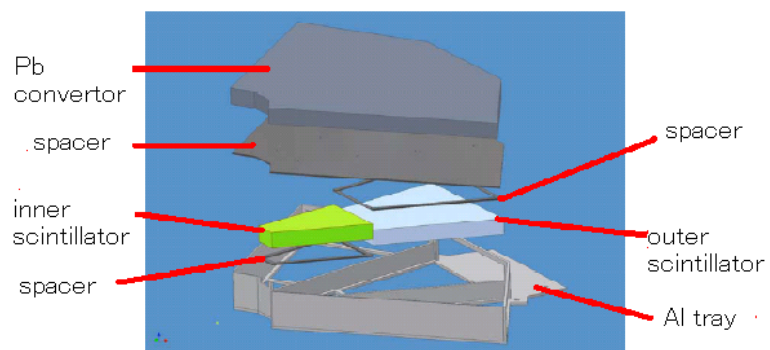


Figure 3.17: Picture of a scintillator part of RxP.

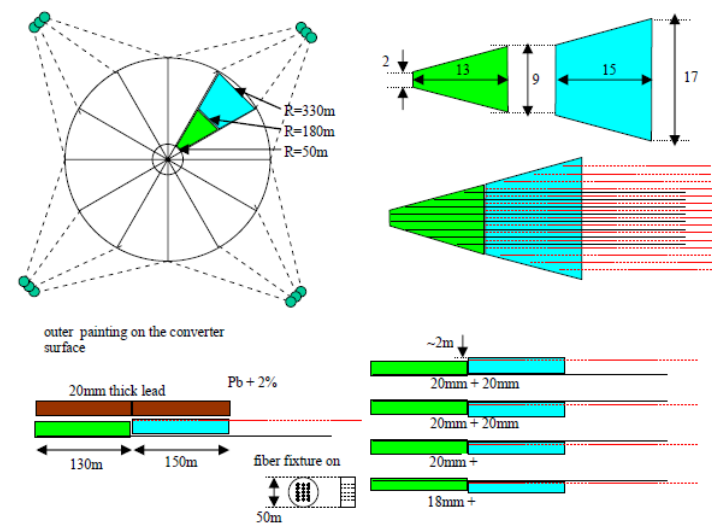


Figure 3.18: Picture of scintillator and fiber part of RxP

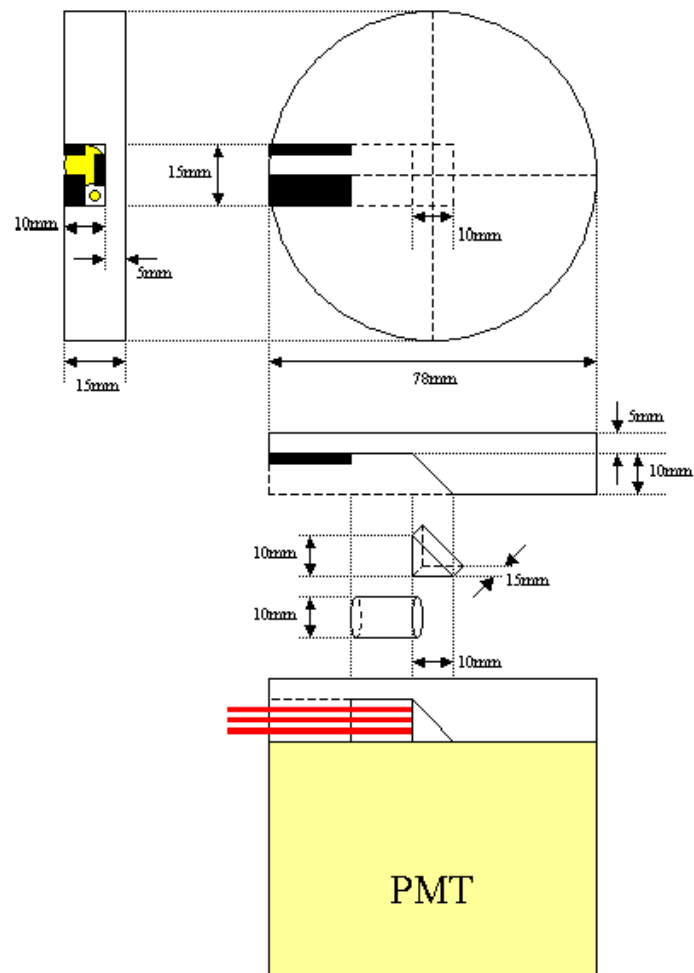


Figure 3.19: Picture of PMT and optical cookie.



Figure 3.20: Photo of fibers and optical cookies.



Figure 3.21: Photo of a PMT part



Figure 3.22: Photo of scintillator parts

# Chapter 4

## Analysis

### 4.1 Event selection

Primary vertex (collision point) position on Z-axis is used as event selection. The following function shows the event cut.

$$|BbcZVertex| < 30.0\text{cm.} \quad (4.1)$$

BbcZVertex is primary vertex on Z-axis measured with BBC.

### 4.2 Reaction Plane Calibration

The reaction plane angle is determined by the following function with azimuthal particle distribution.

$$\Psi = \frac{1}{2} \arctan \left( \frac{\sum_i^n \sin 2\phi_i}{\sum_i^n \cos 2\phi_i} \right), \quad (4.2)$$

where  $\Psi$  is the reaction plane direction,  $n$  is the number of particles and  $\phi_i$  is the direction of emission of  $i$ -th particle. High energy heavy ion collision has large multiplicity, 8000 for Au+Au  $\sqrt{s_{NN}} = 200$  GeV. RxP does not measure the multiplicity distribution but measure the energy deposit distribution of the charged particles as follows,

$$\Psi = \frac{1}{2} \arctan \left( \frac{\sum_j^s \Delta E_j \sin 2\phi_j}{\sum_j^s \Delta E_j \cos 2\phi_j} \right), \quad (4.3)$$

where  $s$  is the number of total segments of detector,  $\phi_j$  is the angle of the center of the  $j$ -th segment and  $\Delta E_j$  is an energy deposit in the  $j$ -th segment. It is assumed that energy deposit is proportional to multiplicity and is measured by Analog-to Digital Converter (ADC) as a charge signal. The mean of the ADC charge is calibrated for all sectors to become equal. However, the raw event plane has some bias still due to conditions of detector or beam collision. The true reaction plane

distribution should be flat because it should randomly be oriented. It is calibrated in order to make the corrected distribution to be flat. The flatness of event plane is very important to measure  $v_2$  because PHENIX has no  $2\pi$  acceptances of central detectors.

Sometime, observed  $\Psi$  has large bias due to shifted collision vertex points  $\text{rhat}$  are not centered in XY plane or gain of PMTs are not same etc..., although real  $\Psi$  should be flat distribution.

Step 1 “Centering calibration”

$$\Psi' = \frac{1}{2} \arctan \left( \frac{(\sin 2\Psi - \langle \sin 2\Psi \rangle) / \sigma_{\sin 2\Psi}}{(\cos 2\Psi - \langle \cos 2\Psi \rangle) / \sigma_{\cos 2\Psi}} \right). \quad (4.4)$$

Step 2 “flattening calibration”

$$\Psi'' = \Psi' + \sum_{n=1}^5 2 \left\{ -\langle \sin (2n\Psi') \rangle \cos (2n\Psi') + \langle \cos (2n\Psi') \rangle \sin (2n\Psi') \right\} / n. \quad (4.5)$$

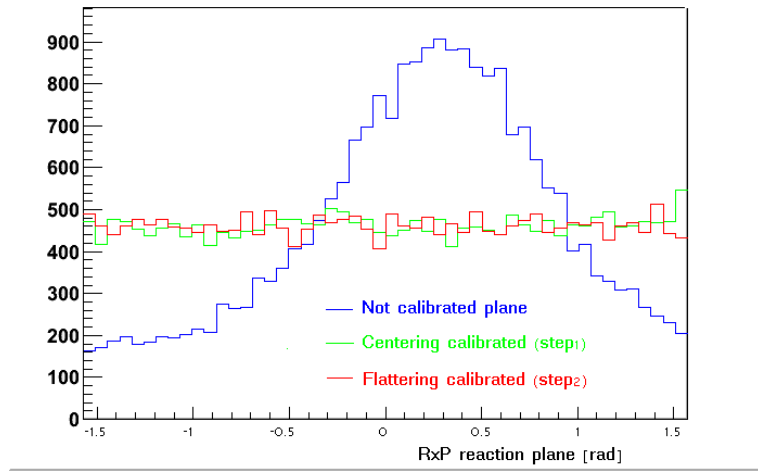


Figure 4.1: Flattening calibration for Reaction Plane of RxP. Blue shows the event plane distribution before calibration. Green shows the event plane distribution after centering (step 1) calibration. Red shows the event plane distribution after flattening (step 2) calibration.

### 4.3 Resolution estimation of Reaction Plane

Reaction plane resolution can be quantified by correlation between real plane and measured plane. The resolution of reaction plane is determined by the difference between measured plane (event plane) and real reaction plane ( $\langle \cos 2(\Psi_{\text{observe}} - \Psi_{\text{real}}) \rangle$ ). It can be estimated by two methods. In 2-sub method, the resolution is estimated with difference of the event plane from two sub-sectors of a detector. (Some detectors can be divided equally by south sector and north sector.) Following functions show the resolution and the difference of event plane of two sectors of a detector,

$$\langle \cos 2 (\Psi_{observe} - \Psi_{real}) \rangle = \frac{\sqrt{\pi}}{2\sqrt{2}} \left[ \chi_m \sqrt{2} \right] \exp \left( - \left[ \chi_m \sqrt{2} \right]^2 / 4 \right) \left\{ I_0 \left( \left[ \chi_m \sqrt{2} \right]^2 / 4 \right) + I_2 \left( \left[ \chi_m \sqrt{2} \right]^2 / 4 \right) \right\}, \quad (4.6)$$

$$\langle \cos 2 (\Psi^S - \Psi^N) \rangle = \frac{\sqrt{\pi}}{2\sqrt{2}} \chi_m \exp (-\chi_m^2 / 4) \{ I_0 (\chi_m^2 / 4) + I_2 (\chi_m^2 / 4) \}, \quad (4.7)$$

where  $\Psi^S$  and  $\Psi^N$  are the event planes which are measured by the south sector or the north sector of a detector. It is important that both of the two sectors have the same resolution in this method.

In 3-sub method, the resolution is estimated with difference between three detectors.

$$\langle \cos 2 (\Psi^A - \Psi^{real}) \rangle = \sqrt{\frac{\langle \cos 2 (\Psi^A - \Psi^B) \rangle \langle \cos 2 (\Psi^C - \Psi^A) \rangle}{\langle \cos 2 (\Psi^B - \Psi^C) \rangle}}. \quad (4.8)$$

There are one reaction plane and azimuthal anisotropy of particle emission from the plane for each event. Then resolution can be estimated by correlation between some measured planes. We know hadron jet occurs at high energy collision. Some particles are emitted in a direction of the jet. The jet may increase the correlation when particles from a same jet traverse the both of detectors which are used for resolution estimation. The large rapidity gap between sub-detectors is always preferred in order to reduce such correlations. In this analysis, reaction plane resolutions are estimated by 2-sub method with south and north sectors. SMD which has low resolution and CNT which has no south or north sector is estimated by 3-sub method with RxP south and RxP north.

## 4.4 Reconstruction of charged particles

Tracking, momentum reconstruction and charge determination are done with DC and PC1. At first, the good tracks are selected that have more than five or six hits on six DC wires. Ghost tracks are rejected by track matching cut with PC2, PC3, TOF.E, TOF.W and EMC. The difference of  $\phi$ -angle or Z-position between hit position on each detector and expected position from DC tracking information are calculated. Signal distribution from charged particle makes a Gaussian peak at zero in 2-dimensional  $\Delta\phi$  and  $\Delta z$  coordinate space (ghost track distributes wider). 2 or 3 sigmas of these Gaussian peaks are selected for charged hadron identification in EMC and PC3. The similar track matching selections with TOF.W and PC2 or TOF.E are applied before the particle identification for  $\pi$ ,  $K$ ,  $p$  and  $d$  with TOF.W or TOF.E.

## 4.5 Particle identification by Time of Flight

$\pi^+$ ,  $\pi^-$ ,  $K^+$ ,  $K^-$ ,  $p$  and  $\bar{p}$  are identified by mass square ( $m^2$ ) distribution with EMC, TOF.E and TOF.W.  $d$ , and  $\bar{d}$  are identified with  $m^2$  distributions of TOF.E and TOF.W include BG subtraction. Figure 4.2, 4.3 and 4.4 show  $m^2$  distribution with TOF.E, TOF.W or EMC at  $p_T = 1 - 5$  GeV/c. 4 Gaussian peaks (3 for EMC) are seen in these figures. Sigma values of these Gaussian peaks are measured for particle identification.

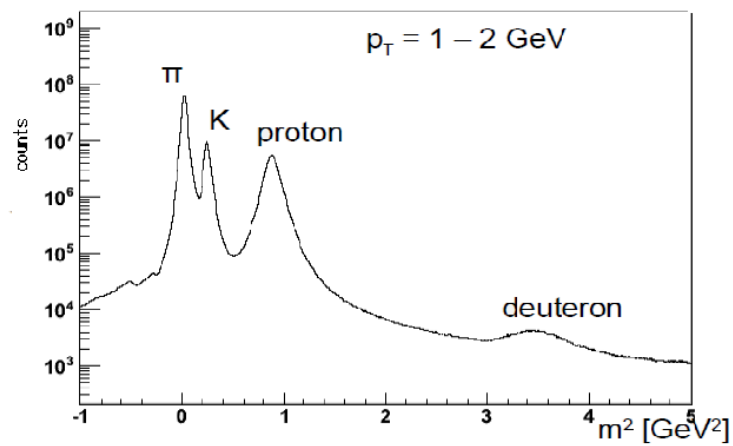


Figure 4.2:  $M^2$  distribution with TOF.E at  $p_T = 1 - 2 \text{ GeV}/c$

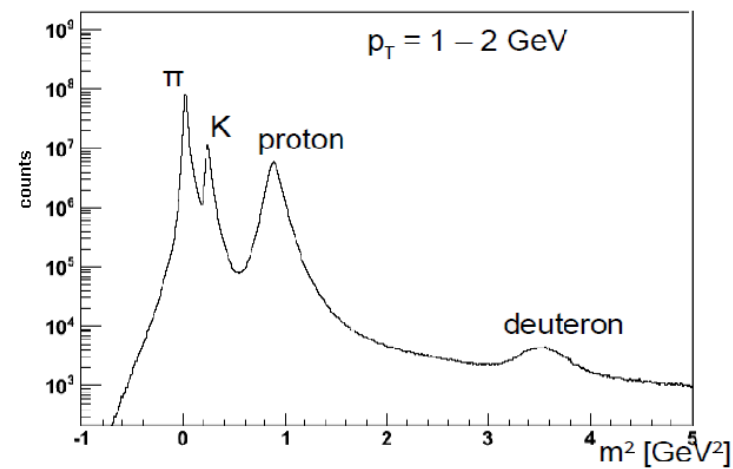


Figure 4.3:  $M^2$  distribution with TOF.W at  $p_T = 1 - 2 \text{ GeV}/c$

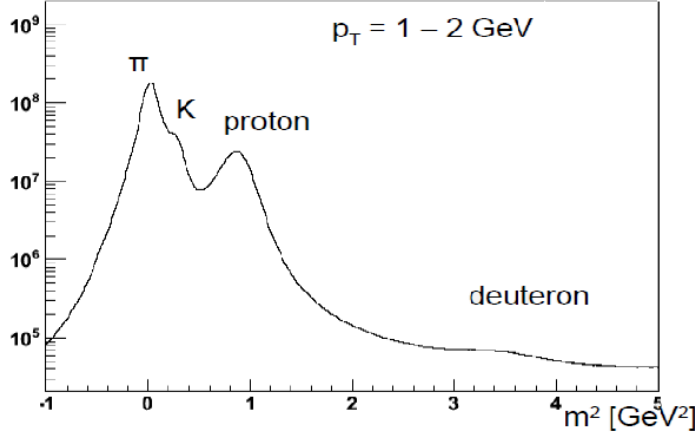


Figure 4.4:  $M^2$  distribution with EMC at  $p_T = 1 - 2$  GeV/c

Figure 4.5, 4.6 and 4.7 show the sigma values of  $m^2$  for each particle with TOF.E, TOF.W or EMC. Solid lines show fitting with the following function.

$$\sigma_{M^2}^2 = 4Ap^4m^2 + 4Bm^4 \left(1 + \frac{m^2}{p^2}\right) + 4Cp^2 (m^2 + p^4). \quad (4.9)$$

Now, following function S is used for particle identified track selection.

$$S = \left| \frac{m^2 - M^2}{\sigma_{M^2}} \right|, \quad (4.10)$$

where  $m^2$  is measured mass square of the track,  $M^2$  is the mean of the Gaussian peak for each particle ( $\pi$ ,  $K$ ,  $p$  or  $d$ ) and  $\sigma_{M^2}$  is the variance value of the Gaussian peak. The S value is calculated for each track and each peak of particle to identify as follows.

- $\pi$  :  $S_\pi < 2$ ,  $S_K > 2$ ,  $S_p > 2$  and  $p_T > 0.2$  GeV/c
- $K$  :  $S_\pi > 2$ ,  $S_K < 2$ ,  $S_p > 2$  and  $p_T > 0.3$  GeV/c
- $p$  :  $S_\pi > 2$ ,  $S_K > 2$ ,  $S_p < 2$  and  $p_T > 0.5$  GeV/c
- $d$  :  $S_\pi > 2$ ,  $S_K > 2$ ,  $S_p > 2$ ,  $S_d < 2$  and  $p_T > 1.0$  GeV/c

## 4.6 Particle identification with ACC at high $p_T$

The elliptic event anisotropy parameter:  $v_2 = \langle \cos 2\Delta\phi \rangle$  is measured for  $\pi$ ,  $K$  and  $p$  identified with TOF.W and ACC. ADC charge information of ACC is calibrated to the number of photons. The number of Cherenkov photon depends on the velocity of the particle.  $\pi$  can be selected or rejected from hadrons with the information of ACC. ACC + TOF.W combination provides good particle identification and S/N ratio, although the statistics are limited because of the limited acceptance. It allows us to study  $\pi$ ,  $K$  and  $p$  at high  $p_T$ . The purity of this identification the hadrons is more than 99 %.

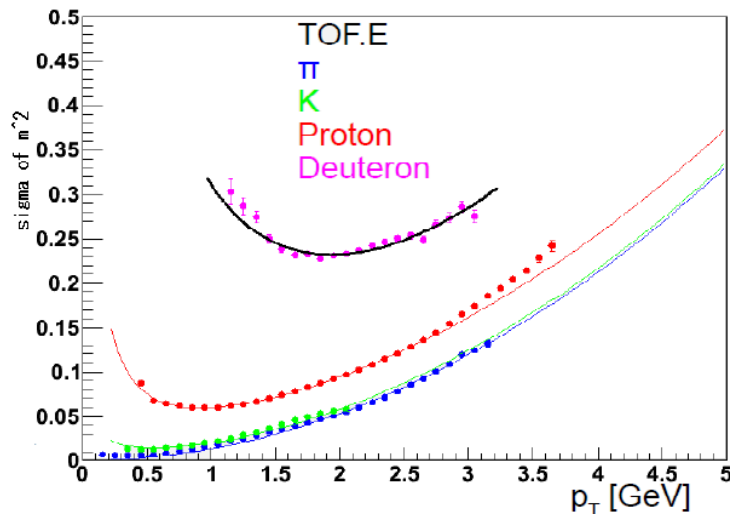


Figure 4.5: Sigma of  $M^2$  as a function of  $p_T$  of particles with TOF.E

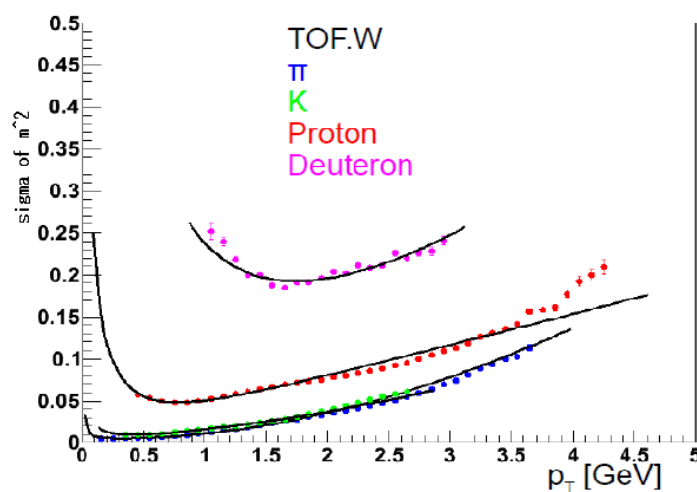


Figure 4.6: Sigma of  $M^2$  as a function of  $p_T$  of particles with TOF.W

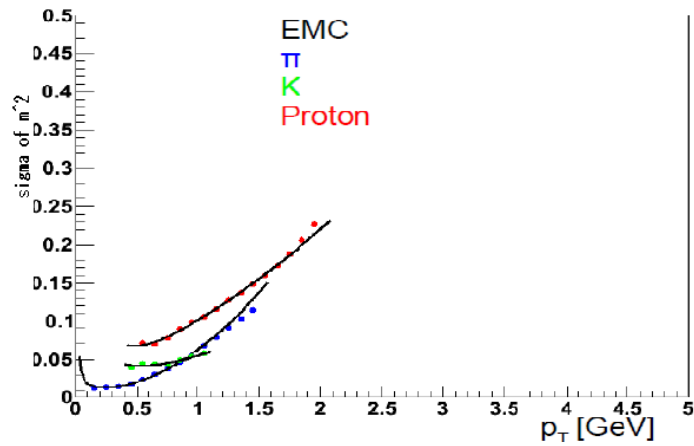


Figure 4.7: Sigma of  $M^2$  as a function of  $p_T$  of particles with EMC

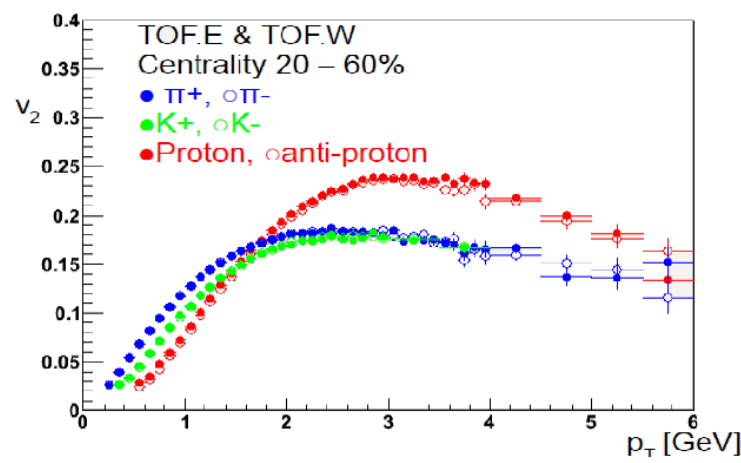


Figure 4.8:  $v_2$  as a function of  $p_T$  of  $\pi^-$ ,  $\pi^+$ ,  $K^-$ ,  $K^+$ ,  $p$  and  $\bar{p}$  with TOF.E and TOF.W

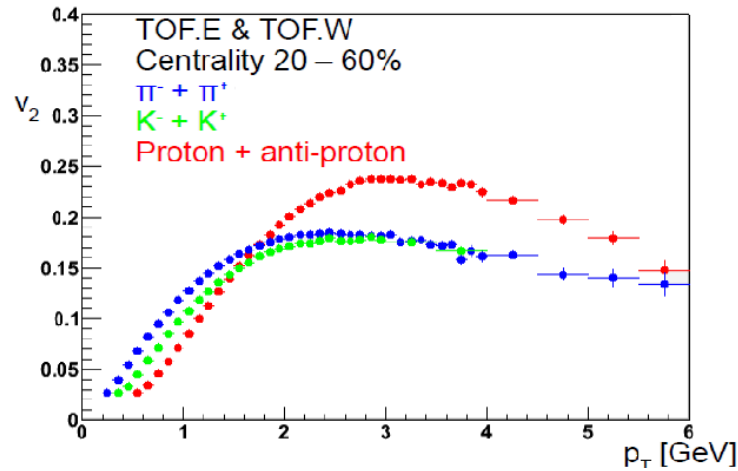


Figure 4.9:  $v_2$  as a function of  $p_T$  of  $\pi$ ,  $K$ ,  $p$  with TOF.E and TOF.W

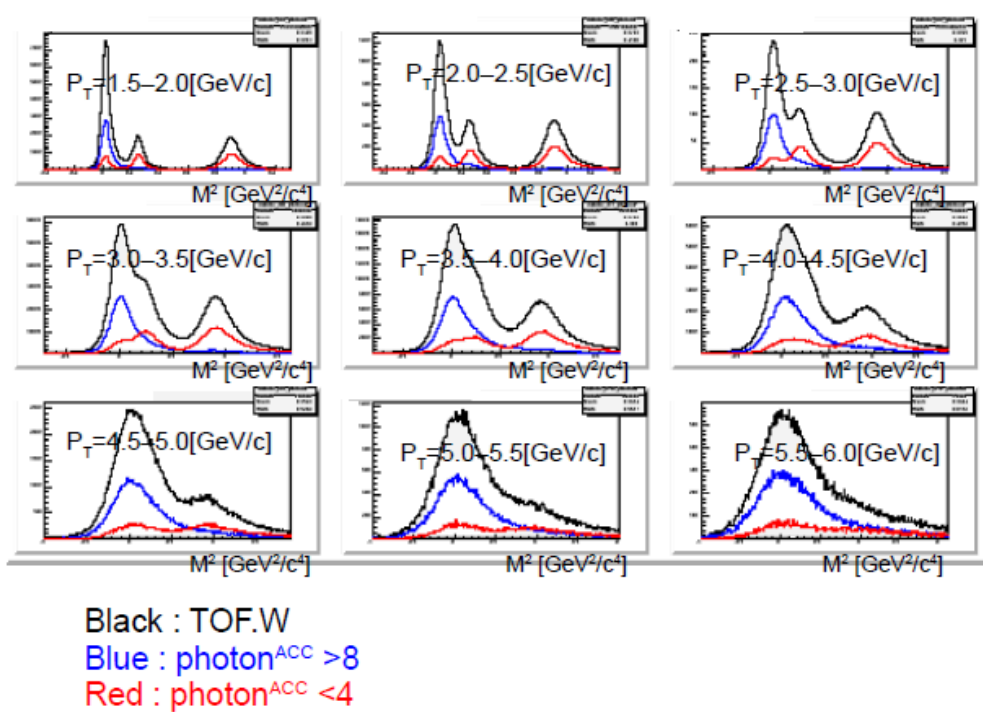


Figure 4.10: Black line shows  $m^2$  distribution of charged hadron with TOF.W. Blue line shows  $\pi$  selection with ACC. Red line shows  $\pi$  rejection with ACC.

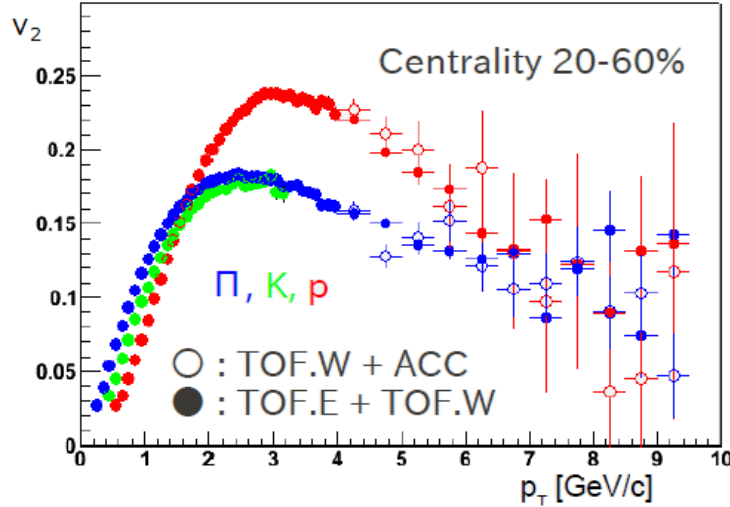


Figure 4.11:  $v_2$  as a function of  $p_T$  with TOF.W (close) and TOF.W+ACC (open)

## 4.7 $d v_2$

Figure 4.12 shows  $m^2$  distribution with TOF.W at  $p_T = 4.0 - 5.0$  GeV/c. The  $v_2$  of  $d$  could not be measured only by the  $m^2$  cut because of the large background. Background is reduced by tight tracking selection cuts and four different BG subtraction methods are used to measure  $d v_2$ .

### 4.7.1 Method 1 ( $\langle \cos 2\Delta\phi \rangle$ and S/N calculation)

$v_2$  of  $d$ +background and  $v_2$  of background is measured by  $\langle \cos 2\Delta\phi \rangle$  same as  $\pi$ ,  $K$ ,  $p$ . And the  $v_2$  of  $d$  is calculated by these two  $v_2$  and the ratio between signal to background. Top of Fig.4.13 shows  $v_2$  which is measured by  $\langle \cos 2\Delta\phi \rangle$  as a function of  $m^2$ . The background  $v_2$  is measured at the side bands of the  $d$  peak at  $m^2 = 2.0 - 3.0$  &  $4.5 - 6.0$  GeV $^2/c^4$ . It is assumed that the background  $v_2$  is flat at  $m^2 = 2.0 - 6.0$ . Figure 4.14 shows Signal+Background (gauss+exp) fitting for each  $p_T$  bin and Fig.4.15 shows the ratio of S/B.

### 4.7.2 Method 2 (Mass fitting)

This method is similar to the Method 1. The  $v_2$  of  $d$  is extracted by fitting the measured  $v_2$  as a function of  $m^2$ . The fitting function is shown as follows,

$$v_2^{observe} = \frac{v_2^d N^d + v_2^{background} N^{background}}{N^d + N^{background}}. \quad (4.11)$$

Figure 4.16 and 4.17 shows this fitting for each  $p_T$  bin with TOF.E and TOF.W. The value of the number of  $d$  signal and the number of background are given by Gaussian and exponential fitting to Fig.4.14.

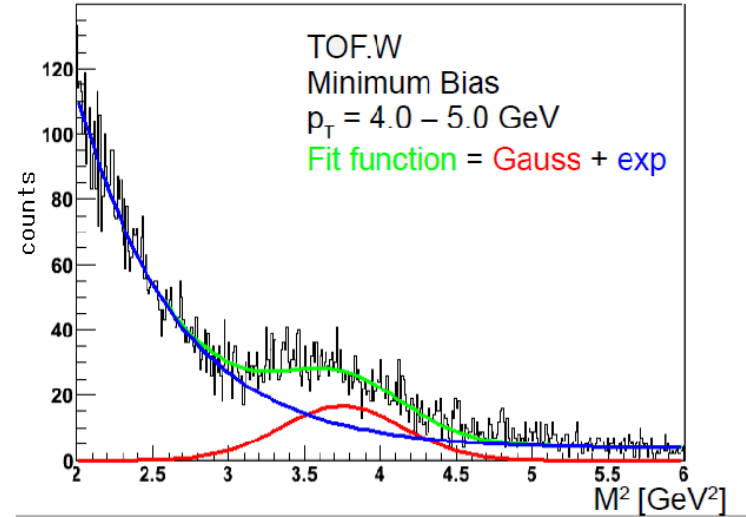


Figure 4.12:  $m^2$  distribution with TOF.W

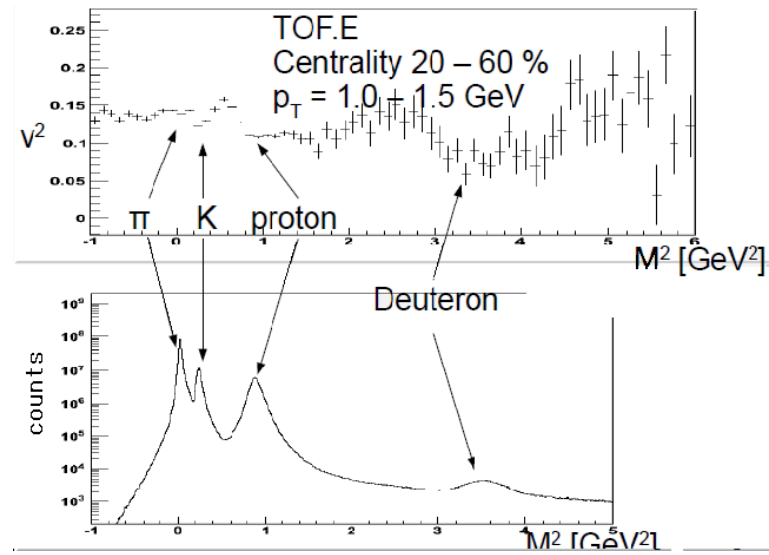


Figure 4.13: Top picture shows  $v_2$  as a function of  $m^2$  which measured as  $\langle \cos 2\Delta\phi \rangle$ . The bottom picture shows the  $m^2$  distribution of charged hadrons.

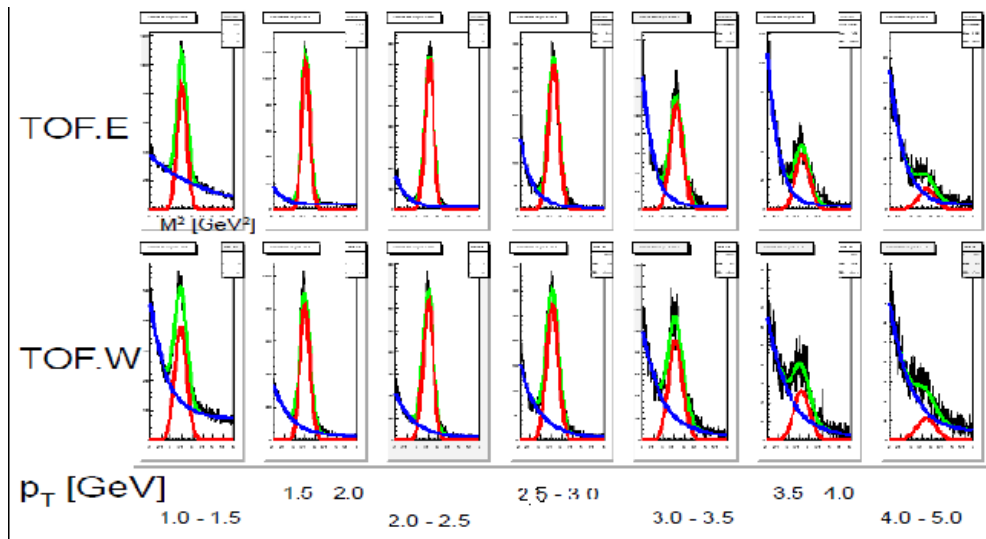


Figure 4.14: Black lines show  $m^2$  distribution of charged particles. Green lines show fitting with Gaussian and exponential functions. Red lines show the Gaussian components of the green lines. Blue lines show the exponential components of the green lines.

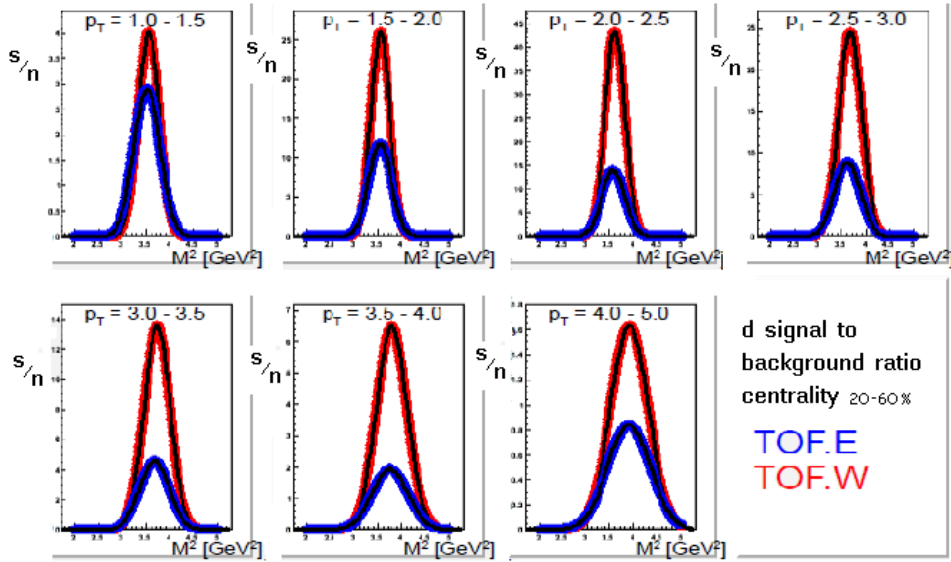
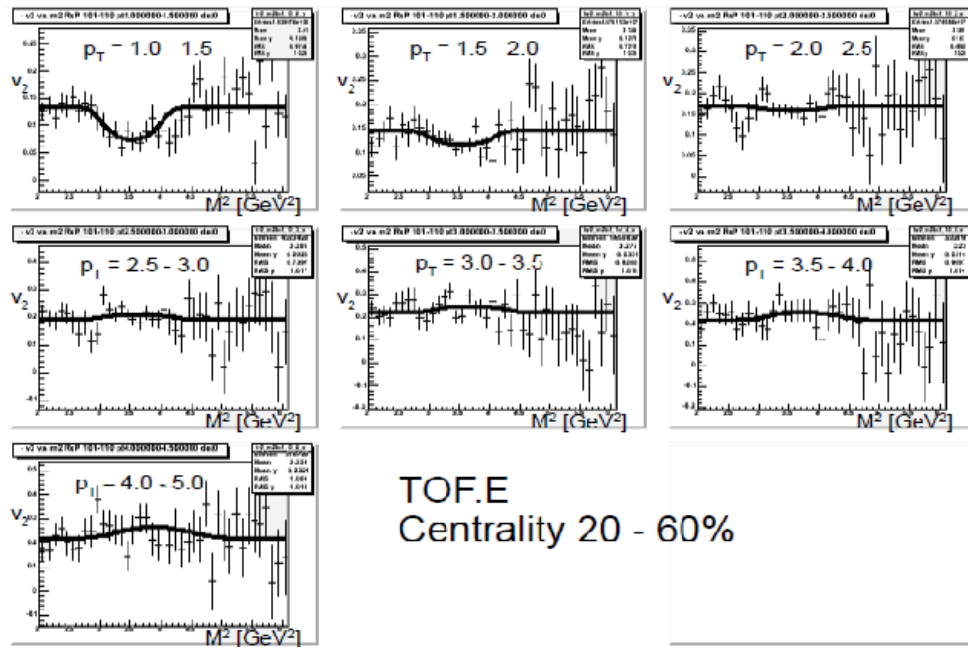
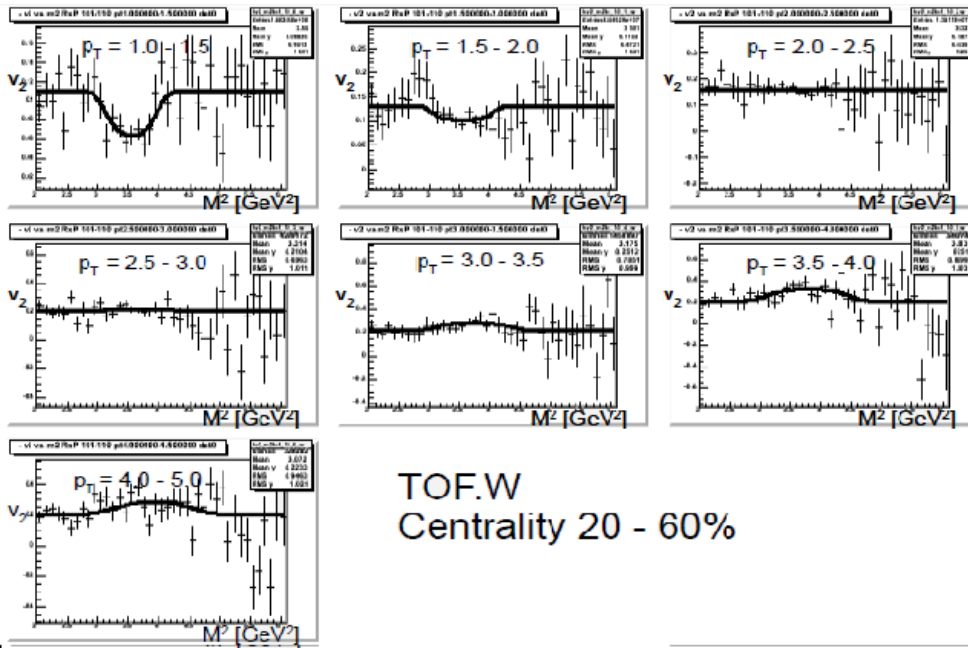


Figure 4.15: Ratio of signal to background of  $d$  identification. The vertical axis shows Gaussian/exponential of Fig.4.14. Red shows it with TOF.W, Blue shows it with TOF.E. Black line shows fitting with Gaussian for them.



TOF.E  
Centrality 20 - 60%

Figure 4.16:  $v_2$  as a function of  $m^2$  for each  $p_T$  bin with TOF.E. Lines show fitting function with the Signal/Background ratio of  $d$ .



TOF.W  
Centrality 20 - 60%

Figure 4.17:  $v_2$  as a function of  $m^2$  for each  $p_T$  bin with TOF.W. Lines show fitting function with the Signal/Background ratio of  $d$ .

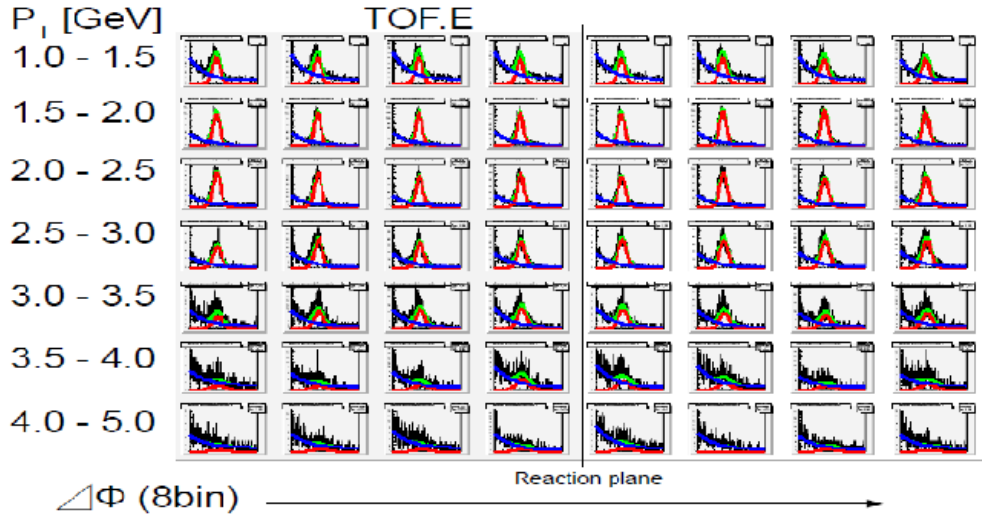


Figure 4.18: Black lines show  $m^2$  distribution of charged particles with TOF.E for each  $p_T$  and  $\phi$ -angle range. Green lines show fitting with Gaussian and exponential functions. Red lines show the Gaussian components of the green lines. Blue lines show the exponential components of the green lines.

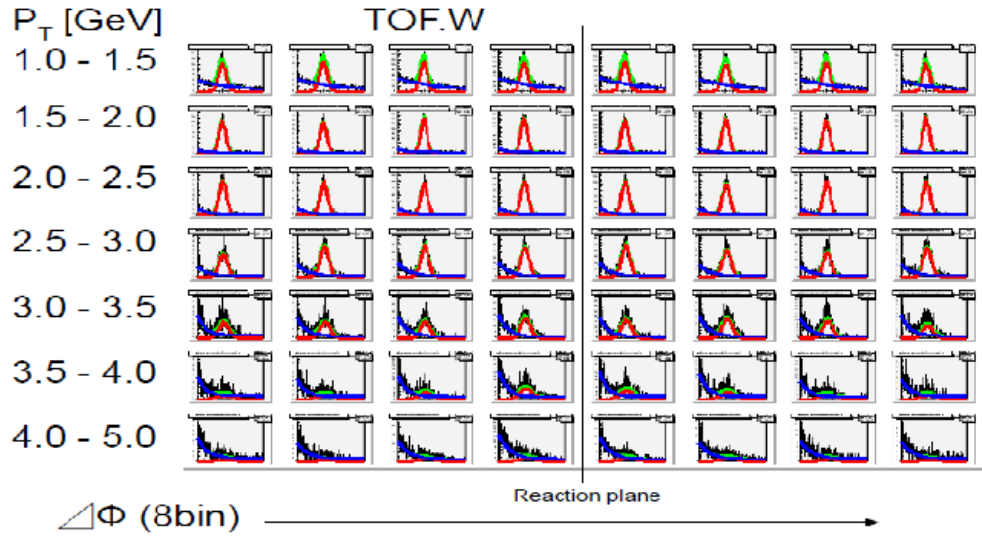


Figure 4.19: Black lines show  $m^2$  distribution of charged particles with TOF.W for each  $p_T$  and  $\phi$ -angle range. Green lines show fitting with Gaussian and exponential functions. Red lines show the Gaussian components of the green lines. Blue lines show the exponential components of the green lines.

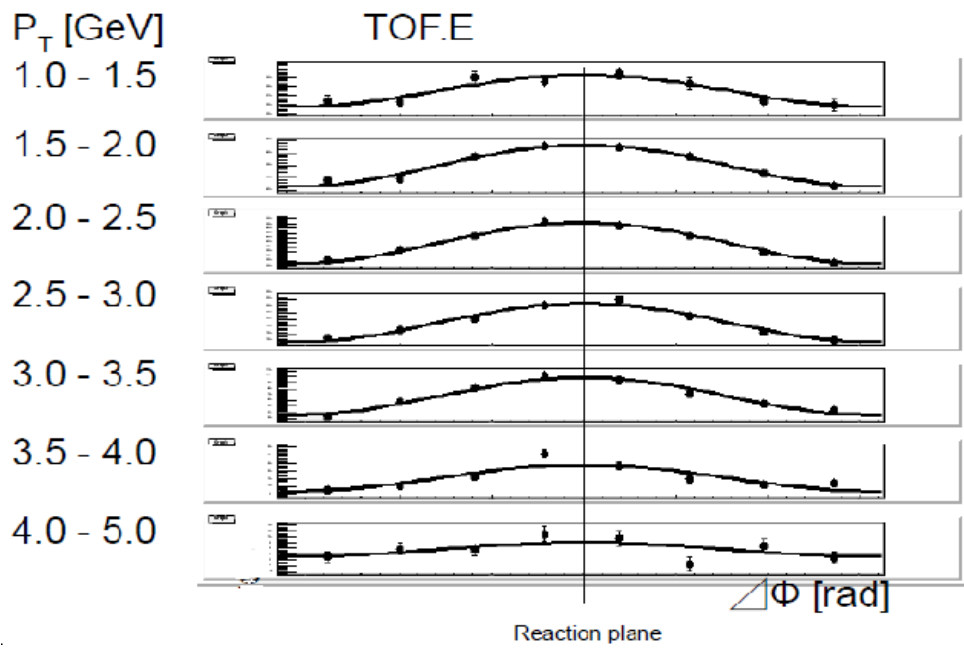


Figure 4.20: Fourier fitting for  $\Delta\phi$  distribution for each  $p_T$  range with TOF.E.

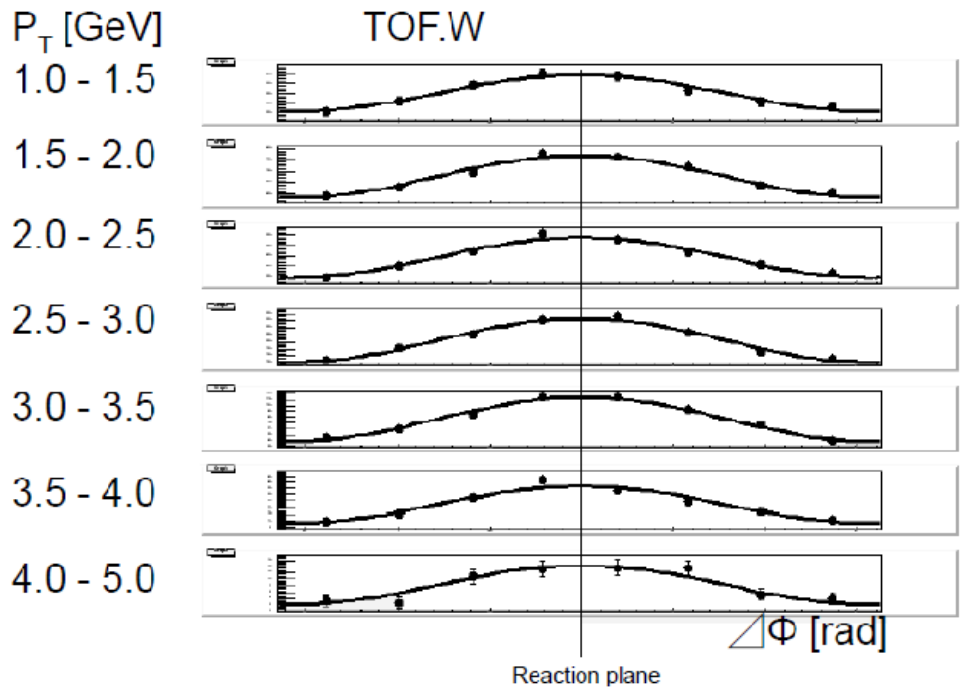


Figure 4.21: Fourier fitting for  $\Delta\phi$  distribution for each  $p_T$  range with TOF.W.

### 4.7.3 Method 3 (Fourier fitting)

In this method,  $v_2$  is measured by Fourier fitting on  $\Delta\phi$  distribution after subtracting the background by gauss+exp function fitting. Figure 4.18 and 4.19 show gauss+exp fitting for each  $p_T$  and  $\Delta\phi$  bin. Figure 4.20 and 4.21 show Fourier fitting on  $\Delta\phi$  distribution.

### 4.7.4 method 4 (In-Out ratio)

$v_2$  is calculated by yield ratio between in-plane and out-plane as following function 4.12 and 4.13 after subtracting background.

$$v_2 = \frac{\pi (N_{in} - N_{out})}{4 (N_{in} + N_{out})}, \quad (4.12)$$

$$\delta v_2 = \frac{\pi \sqrt{N_{out}^2 \delta N_{in}^2 + N_{in}^2 \delta N_{out}^2}}{2 (N_{in} + N_{out})^2}. \quad (4.13)$$

### 4.7.5 Comparison with the methods

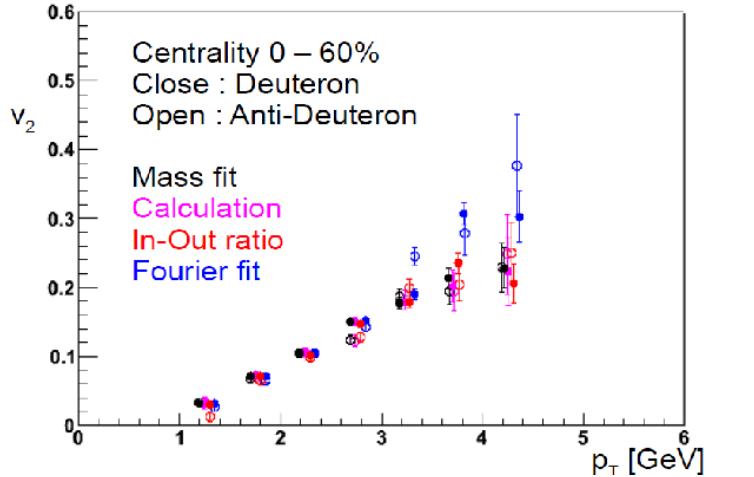


Figure 4.22:  $v_2$  as a function of  $p_T$  by four methods for  $d$  and  $\bar{d}$  at centrality 0 – 60%.

Figure 4.22 and 4.23 shows  $v_2$  of  $d$  and  $\bar{d}$  from the four different methods for each centrality range. These are consistent within error, except high  $p_T$  in Fourier fit (or In-Out ratio) method at centrality 20 – 60%. That is over estimation due to bad fitting for each  $m^2$  distribution especially out of the plane because of poor statistics. This effect from the small statistics are clear for  $\bar{d}$  at mid centrality and high  $p_T$  range in Fourier fit method. The statistics are divided in eight bins in  $\Delta\phi$  in Fourier fit method and two bins in In-Out ratio method. Figure 4.24 and 4.25 show  $v_2$  from four methods for combined  $d + \bar{d}$ . The similar effect due to the poor statistics are seen in the Fourier fit method at centrality 20 – 60%. The calculation method (Method 1) has been chosen and estimated systematic errors are defined by the difference from other methods except the Fourier fit method.

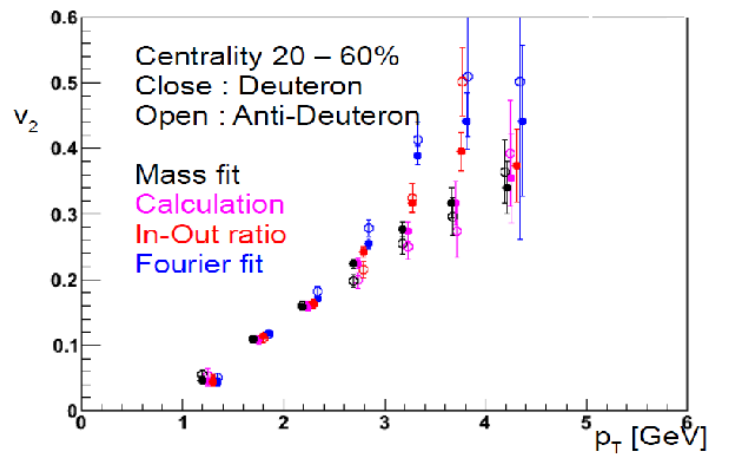


Figure 4.23:  $v_2$  as a function of  $p_T$  by four methods for  $d$  and  $\bar{d}$  at centrality 20 – 60%.

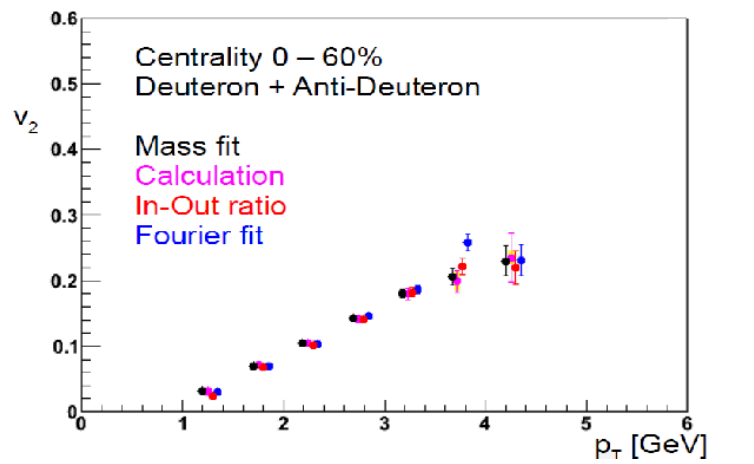


Figure 4.24:  $v_2$  as a function of  $p_T$  by four methods for  $d + \bar{d}$  at centrality 0 – 60%.

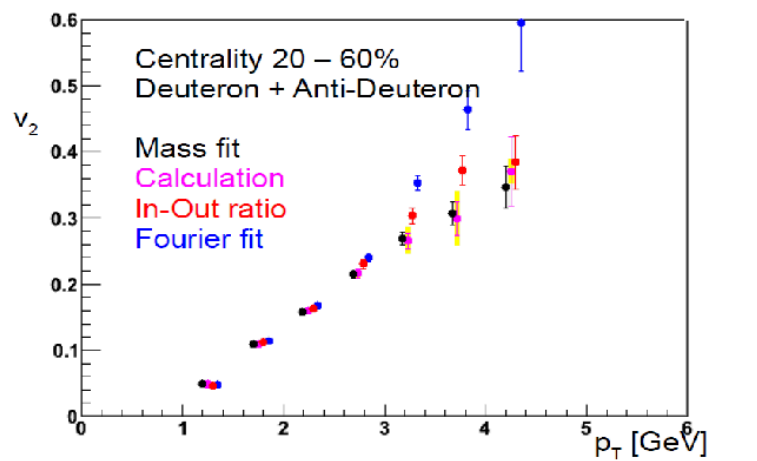


Figure 4.25:  $v_2$  as a function of  $p_T$  by four methods for  $d + \bar{d}$  at centrality 20 – 60%.

## 4.8 $\Lambda$ and $\bar{\Lambda}$ reconstruction with $p\pi^-$ and $\bar{p}\pi^+$

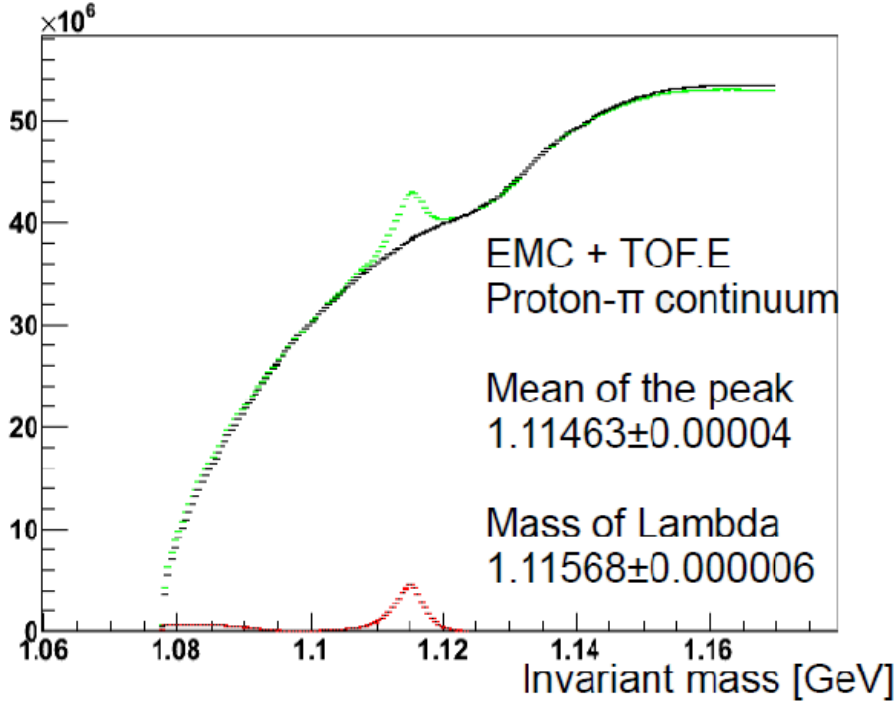


Figure 4.26: Invariant mass distribution of  $p\pi$  pairs. Green shows the real pair. Black shows normalized mix pairs. Red shows the difference of the real and mix.

Figure 4.26 shows invariant mass distribution of  $p\pi$  pair for  $\Lambda$  reconstruction. TOF.E and EMC are used to identify  $p$  ( $isP < 2$ ) and  $\pi$  ( $isPi < 2$ ). The large background is subtracted by the pair distribution from the mixed events. Mixed events are chosen from the same event class where the reaction plane and the centrality are divided into ten bins and the z-vertex is divided into twelve bins for the mixed pair. The mixed events are normalized at mass windows of  $1.08 < IM < 1.1$  &  $1.13 < IM < 1.17$  GeV/c<sup>2</sup>.

$\Lambda v_2$  is measured in the same way as  $d$  ( $m^2$  is replaced by  $IM$ ). But, “calculation method (Method 1)” is not suitable because the  $v_2$  is not flat as  $IM$ . “Mass fit”, “Fourier fit” and “In-Out ratio” (Method 2, 3, 4) were done. Figure 4.27 shows the Signal to Background ratio for each  $p_T$  range and Fig.4.28 shows the Mass fit method. Figure 4.29 shows the  $IM$  distribution for each  $p_T$  and  $\Delta\phi$  bin and Fig.4.30 shows the Fourier fit method. Figure 4.31 and 4.32 show  $v_2$  of  $\Lambda$  and  $\bar{\Lambda}$  measured with the three methods. These are consistent within error. Figure 4.33 and 4.34 show the  $v_2$  of combined  $\Lambda + \bar{\Lambda}$  measured with the three methods.

## 4.9 $\phi$ -meson reconstruction with $K^+K^-$ pair

Figure 4.35 shows the invariant mass (IM) distribution of  $K^+K^-$  pairs for  $\phi$ -meson. TOF.E and EMC are used for particle identification ( $isK < 2$ ). The mixed events are normalized at  $1.04 <$

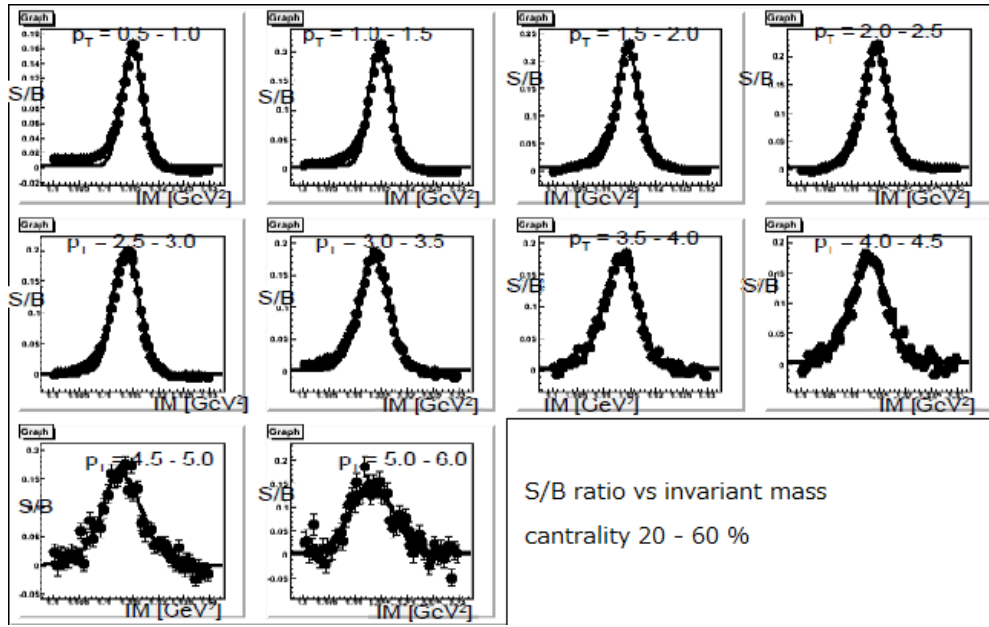


Figure 4.27: Ratio of signal/background as a function of invariant mass of  $\Lambda$  ( $p\text{-}\pi$ ) for each  $p_T$  range.

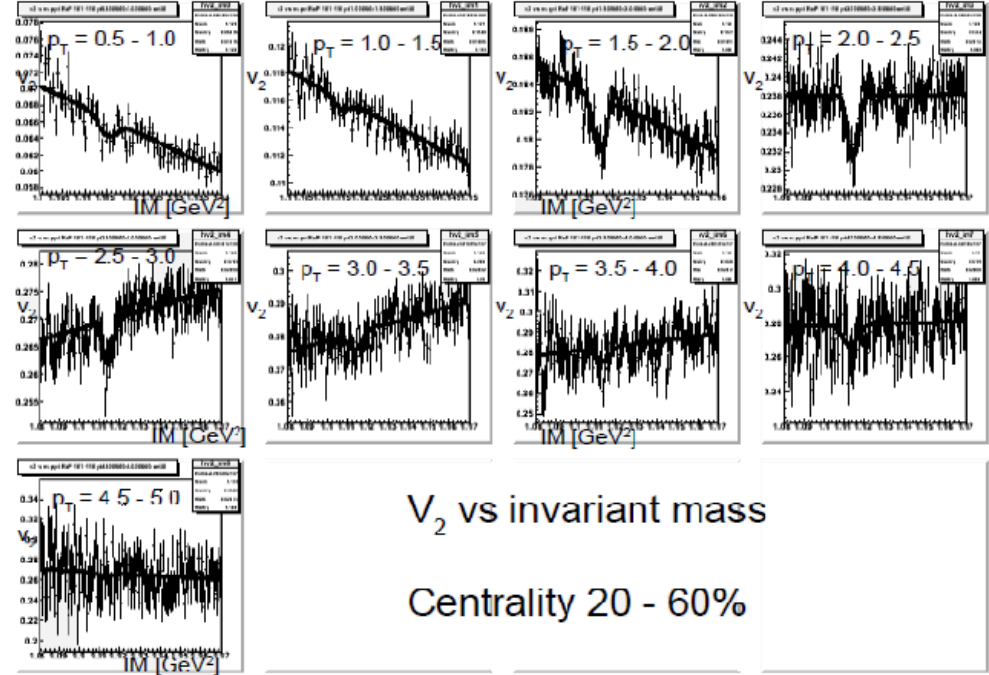


Figure 4.28:  $v_2$  as a function of invariant mass of  $\Lambda$  ( $p\text{-}\pi$ ) for each  $p_T$  range. Lines show fitting function with the Signal/Background ratio of  $\Lambda$ .

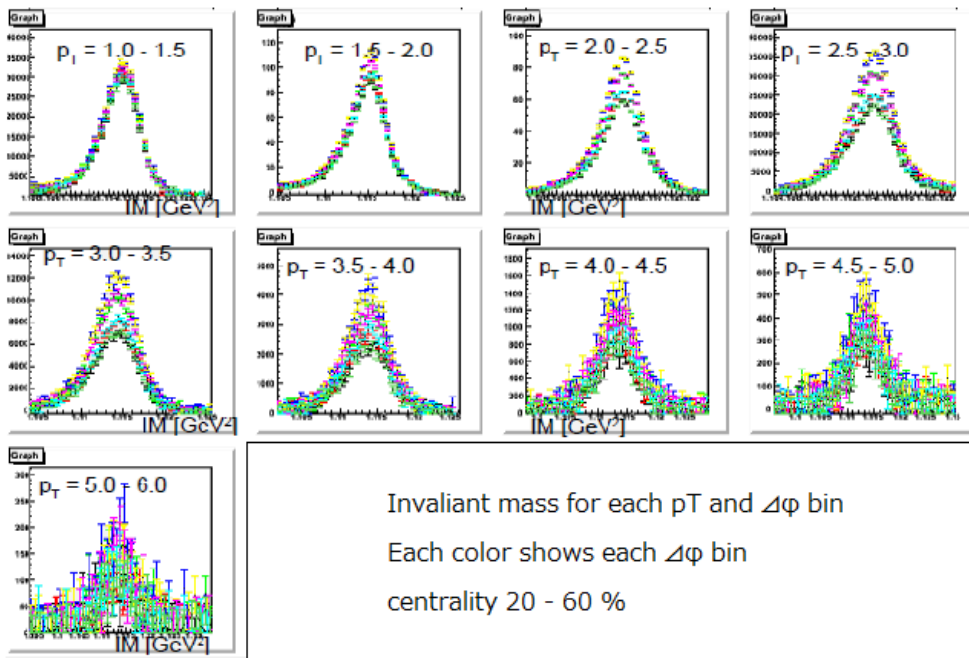


Figure 4.29: Distribution of the invariant mass of  $\Lambda$  ( $p$ - $\pi$ ). Background rejection with mix pairs for each  $p_T$  and  $\Delta\phi$  range.

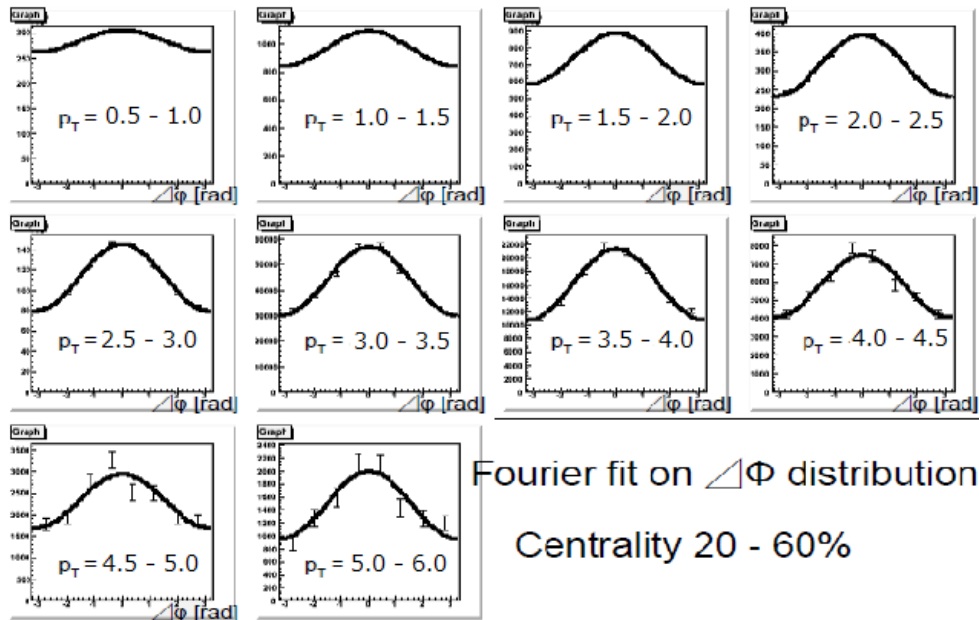


Figure 4.30: Fourier fitting for  $\Delta\phi$  distribution of  $\Lambda$  for each  $p_T$  range.

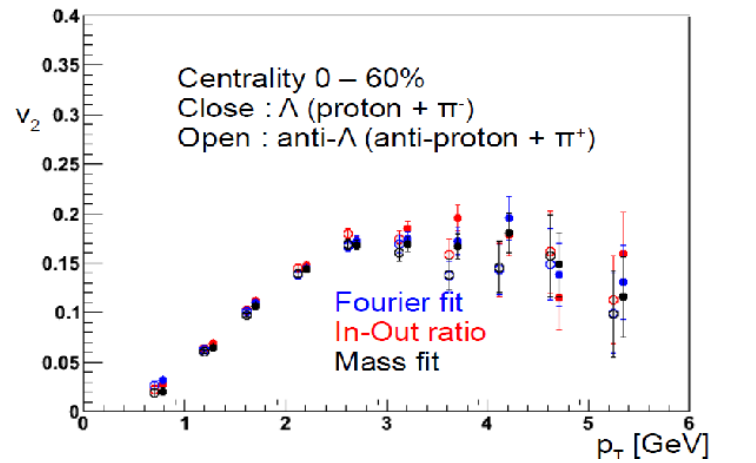


Figure 4.31:  $v_2$  as a function of  $p_T$  for  $\Lambda$  and  $\bar{\Lambda}$  by each method at centrality 0 – 60%.

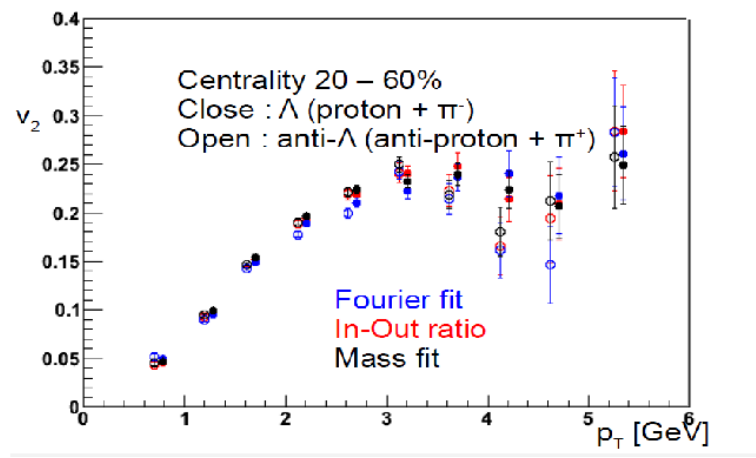


Figure 4.32:  $v_2$  as a function of  $p_T$  for  $\Lambda$  and  $\bar{\Lambda}$  by each method at centrality 20 – 60%.

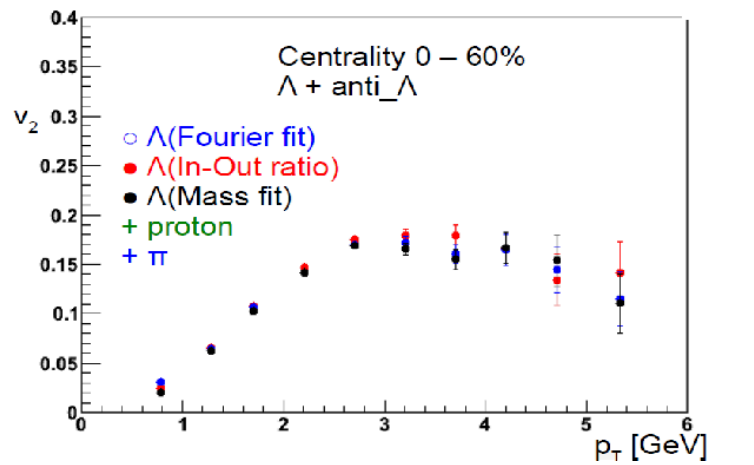


Figure 4.33:  $v_2$  as a function of  $p_T$  for  $\Lambda + \bar{\Lambda}$  by each method at centrality 0 – 60%.

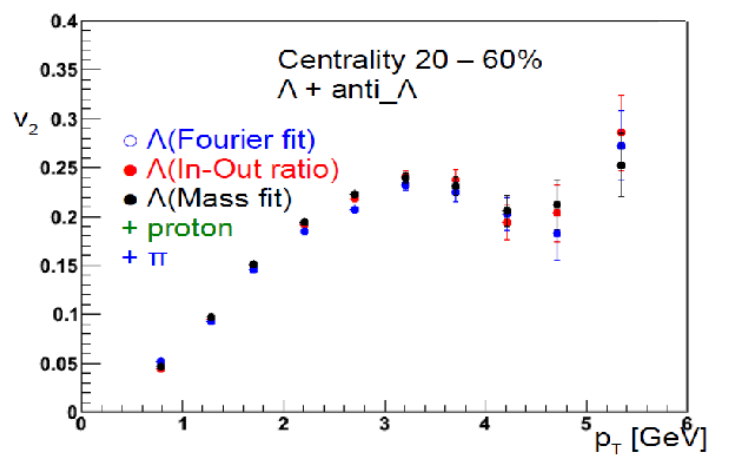


Figure 4.34:  $v_2$  as a function of  $p_T$  for  $\Lambda + \bar{\Lambda}$  by each method at centrality 20 – 60%.

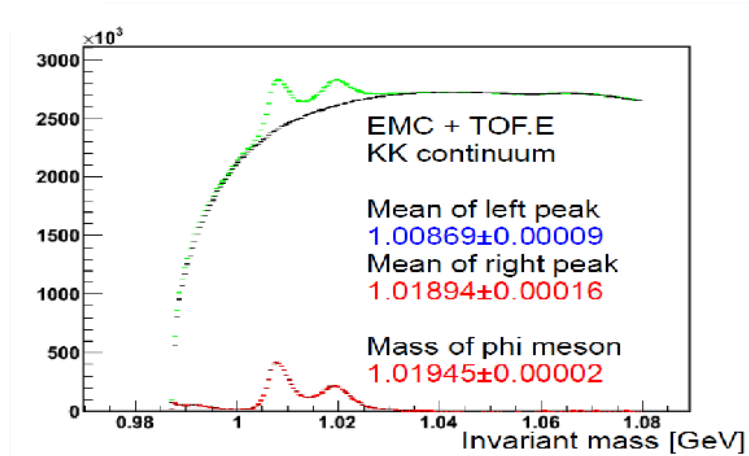


Figure 4.35: Invariant mass distribution of  $K^+K^-$  pairs. Green shows real pairs. Black shows normalized mix pairs. Red shows the difference of the real pairs and mix pairs.

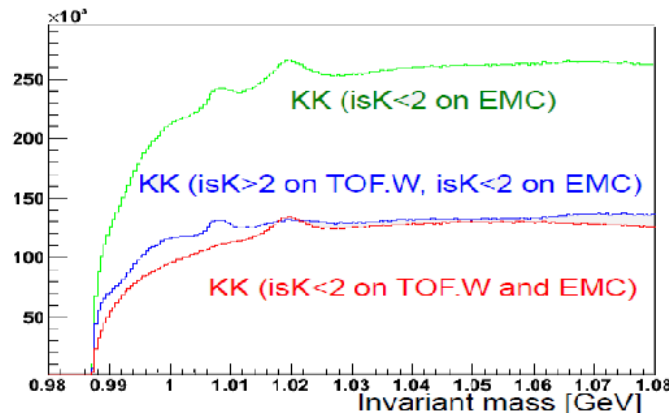


Figure 4.36: Invariant mass distribution of  $K^+K^-$  pairs. These are measured with TOF.W. Green shows distribution of pairs of  $K^+K^-$  which is identified with EMC. Blue shows distribution of pairs of  $K^+K^-$  which is identified with TOF.W. Red shows distribution of pairs of  $K^+K^-$  which is identified with both of TOF.W and EMC.

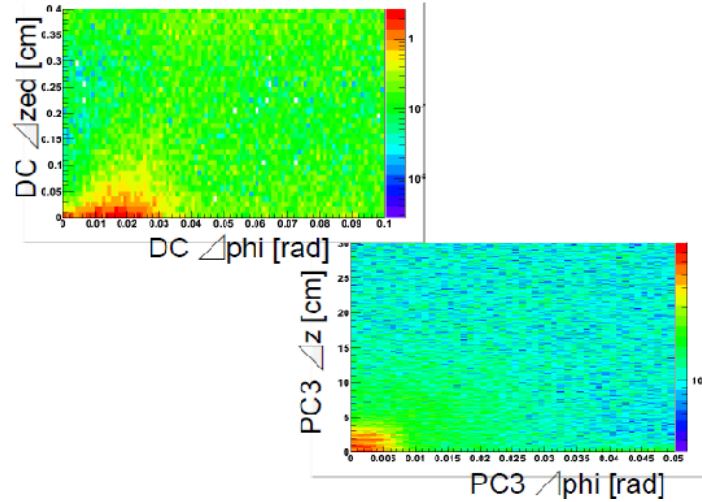


Figure 4.37: 2-D histogram of  $\Delta\phi$  vs  $\Delta z$  distribution with DC (top) and PC3 (bottom). These values are normalized by mix event. Ghost peak is seems around (0,0).

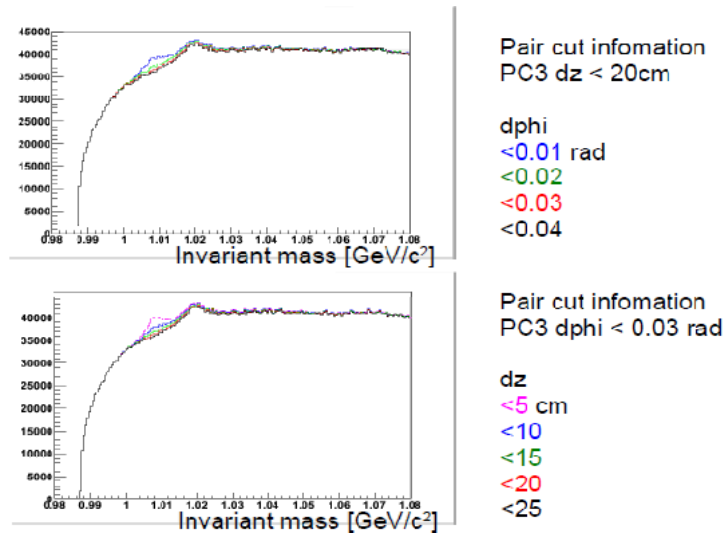


Figure 4.38: Distribution of invariant mass of  $K^+K^-$  pairs and ghost rejection by pair cut with PC3.

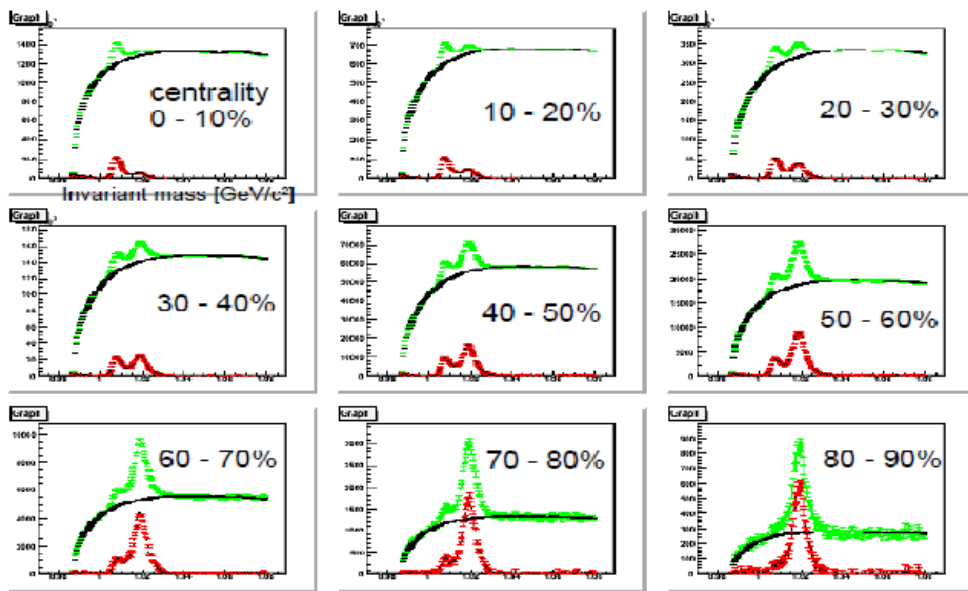


Figure 4.39:  $K^+K^-$  pairs without pair cut for each centrality. Green shows the real pairs. Black shows normalized mix pairs. Red shows the difference of the real pairs and mix pairs.

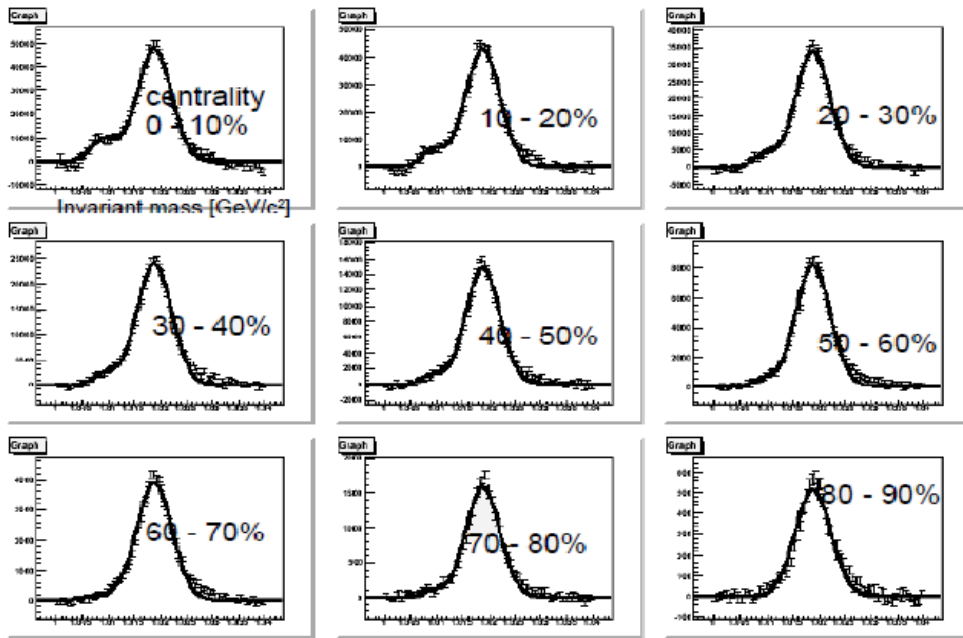


Figure 4.40:  $K^+K^-$  pairs with pair cut for each centrality. Points shows the difference of the real pairs and mix pairs. Line shows double Gaussian fitting.

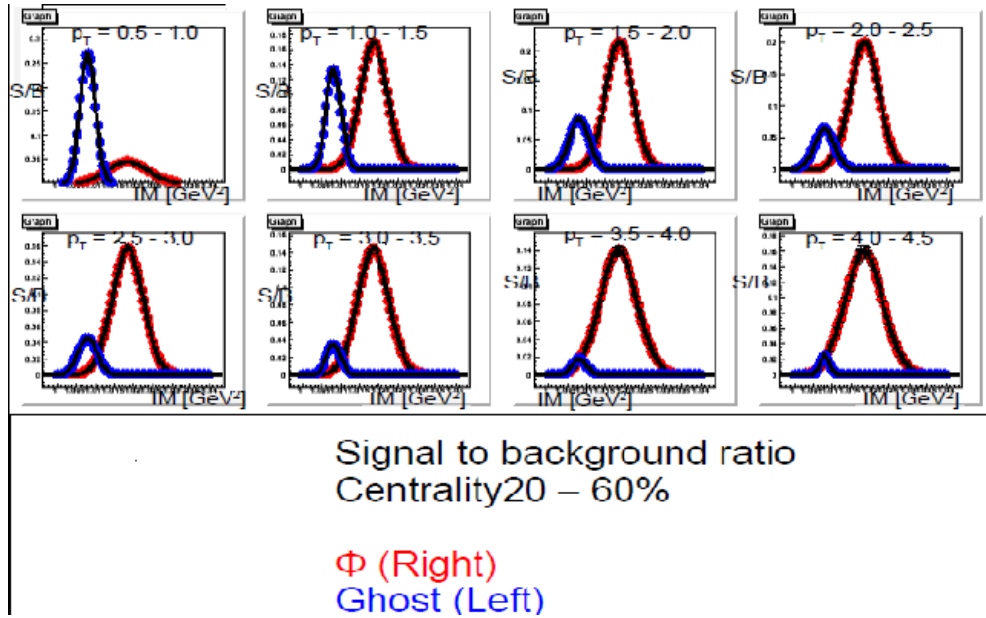


Figure 4.41: The ratio of signal/background without the pair cut for each  $p_T$  range. Red shows  $\phi$ -meson peak component and Blue shows that of ghost peak.

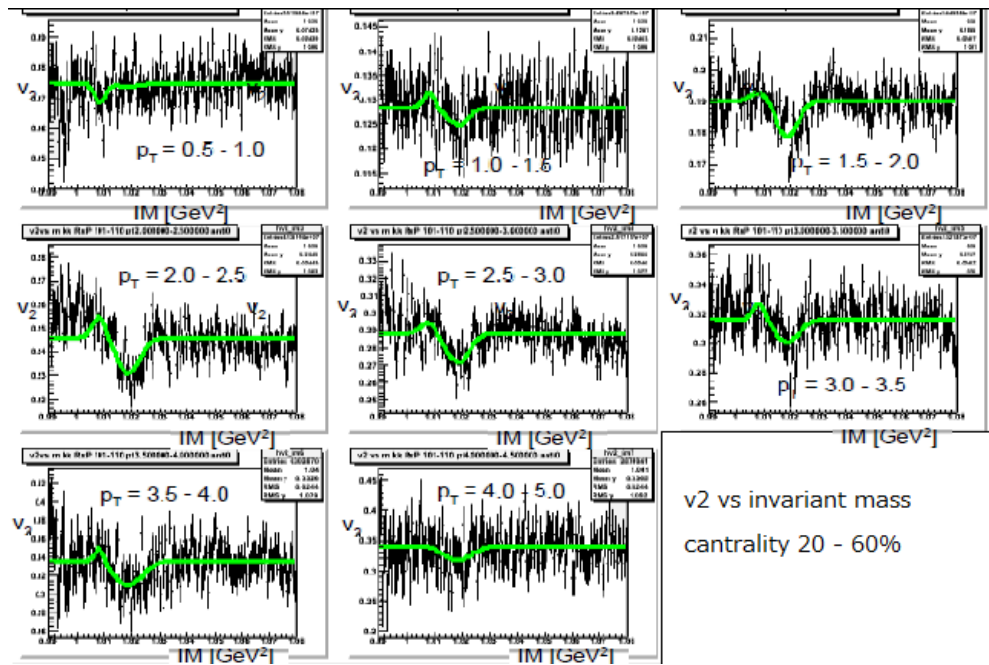


Figure 4.42:  $v_2$  as a function of distribution of invariant mass of  $K^+K^-$  pairs without pair cut for each  $p_T$  range.

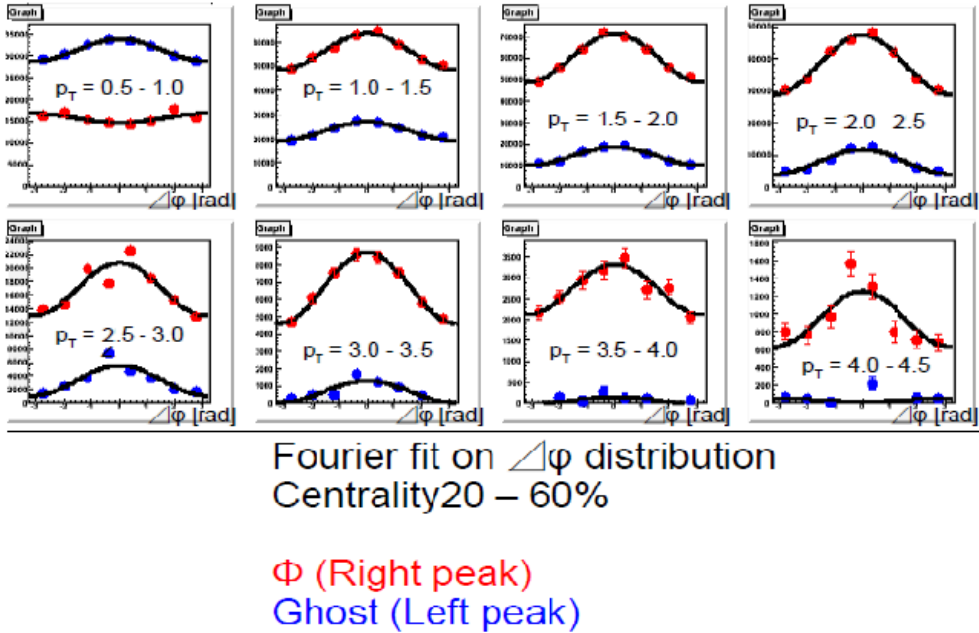


Figure 4.43: Fourier fitting for the  $\Delta\phi$  distribution of  $\phi$ -meson without the pair cut for each  $p_T$  range. Red shows  $\phi$ -meson and Blue shows ghost.

$IM < 1.08 \text{ GeV}/c^2$ . Basically, the methods for particle identification, invariant mass pair and measurement of  $v_2$  are same as that of  $\Lambda$ . However, the two peaks are seen in the invariant mass distribution of  $K^+K^-$  pairs. Right peak has mean value which is same as the expected mass of  $\phi$ -meson. Left peak is the ghost which has wrong mean value for  $\phi$ -meson mass. The ghost peak with TOF.E or TOF.W is very small compared to the EMC particle identification.

Figure 4.36 shows the invariant mass distribution that is measured with TOF.W acceptance range (It is in the EMC acceptance range) with the same tracking cut. Green shows pairs of  $K^+K^-$  which is identified by EMC. Blue shows pairs of  $K^+K^-$  which are identified as K in EMC but they are not identified as K in TOF.W. Red shows pairs of  $K^+K^-$  which are identified as K in both of TOF.W and EMC. The true  $\phi$ -meson peak (right peak) is only visible for red line and ghost peak (left peak) is only visible for blue line. It means that fake K track makes the ghost peak in  $K^+K^-$  combinatorial distribution of EMC. The ghost peak could not be rejected by particle identification cut or tracking cut with EMC.

The ghost peak is found to be rejected by pair cut with PC3. Figure 4.37 shows ghost peak of  $\Delta\phi$  vs  $dz$  distribution of DC or PC3. Figure 4.38 shows the ghost rejection and pair cut information. The values of PC3  $\Delta\phi < 0.03 \text{ rad}$  and PC3  $\Delta z < 20 \text{ cm}$  are used to reject ghost peak. Pair cut with DC has no effect to reject the ghost peak. Figure 4.39 shows the invariant mass picture for each centrality before pair cut and Fig.4.40 shows that of after pair cut. The ghost peak can be rejected with the pair cut.  $\phi$ -meson peak is extracted by double Gaussian fit with the pair cut and without the pair cut for systematic study.

Figure 4.44 and 4.45 show  $v_2$  for  $\phi$ -meson and ghost without pair cut. The ghost has very large  $v_2$ . Figure 4.46 shows comparison  $v_2$  by EMC+TOF.E and by TOF.E+TOF.W. They are consistent within error.

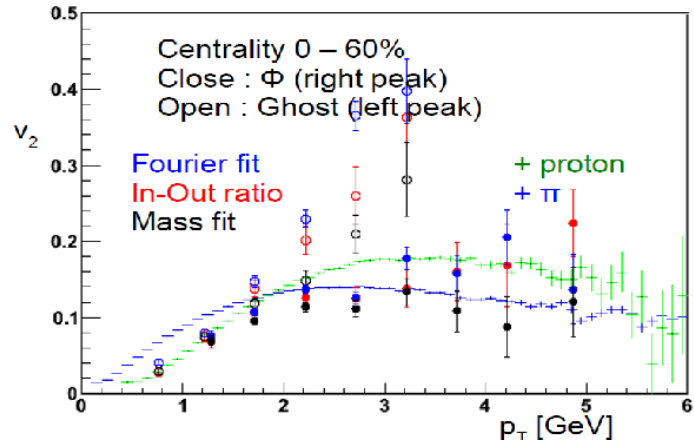


Figure 4.44:  $v_2$  as a function of  $p_T$  of  $\phi$ -meson and ghost by each method at centrality 0 - 60 %.

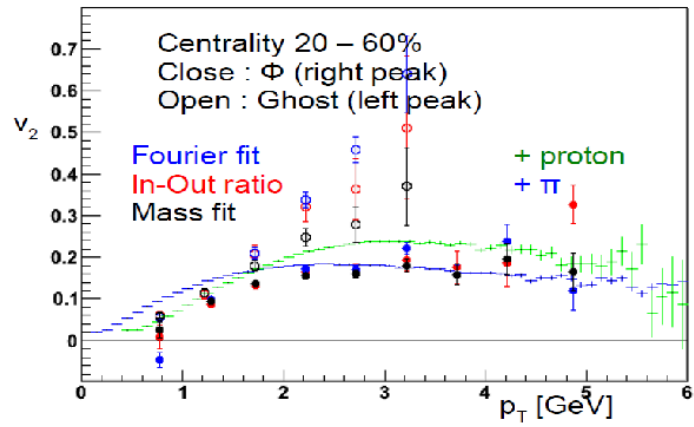


Figure 4.45:  $v_2$  as a function of  $p_T$  of  $\phi$ -meson and ghost by each method at centrality 20 - 60 %.

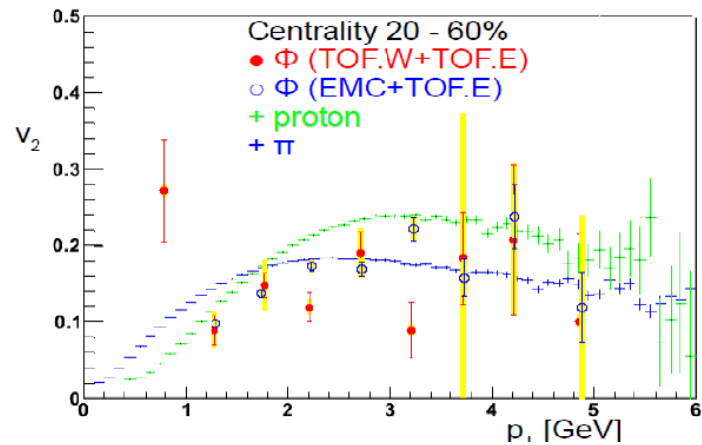


Figure 4.46:  $v_2$  as a function of  $p_T$  of  $\phi$ -meson and with EMC+TOF.E or TOF.W+TOF.E.

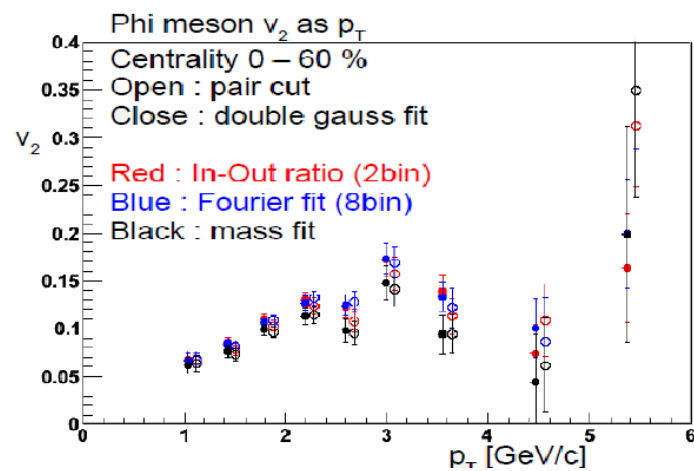


Figure 4.47:  $v_2$  as a function of  $p_T$  by each method at centrality 0 – 60%.

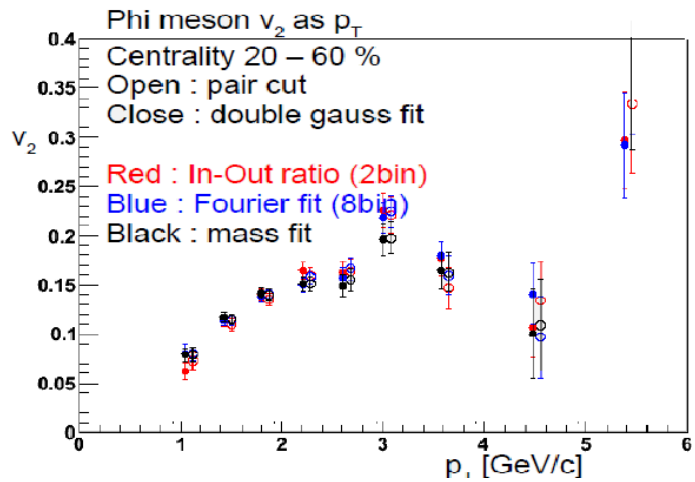


Figure 4.48:  $v_2$  as a function of  $p_T$  by each method at centrality 20 – 60%.

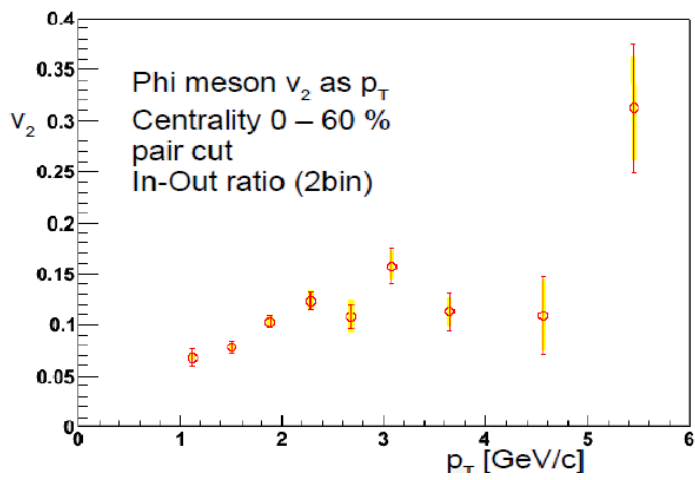


Figure 4.49:  $\phi v_2$  as a function of  $p_T$  at centrality 0 – 60%.

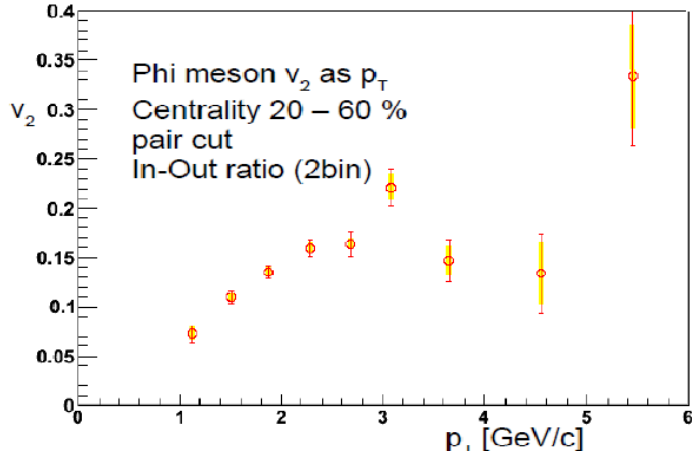


Figure 4.50:  $\phi v_2$  as a function of  $p_T$  at centrality 20 – 60%.

Figure 4.47 and 4.48 show comparison with 6 methods. They are all consistent nicely with each other. In Fig.4.49 and 4.50, the In-Out ratio method (method 4) is chosen and the differences from other methods are used as systematic error.

#### 4.10 $p_T$ value of each X-axis bin.

The  $p_T$  value of each  $p_T$  bin for  $v_2$  as a function of  $p_T$  is estimated as the mean value for each  $p_T$  bin with  $p_T$  distribution of measured particle yield. The mean value of each  $p_T$  bin (as x-axis of  $v_2$  as a function of  $p_T$ ) is estimated with average  $p_T$  value of fit function in this paper. However  $p_T$  of  $\Lambda$  is overestimated because the momentum of charged particle is calculated by DC position/angle and Magnetic field with an assumption that all tracks came from the primary vertex although  $\Lambda$  decays away from the collision point at high  $p_T$ . The difference between generated  $p_T$  and the reconstructed  $p_T$  is estimated by GEANT simulation. The effect of  $\Lambda$  decay in PHENIX detectors and reconstructed  $p_T$  in DC with magnetic field are calculated in the GEANT simulation.

Figure 4.51 shows the result of the simulation. The true  $p_T$  is estimated by the measured  $p_T$  multiplied by the ratio between Input/Output, that is same as generated/reconstructed  $p_T$ .

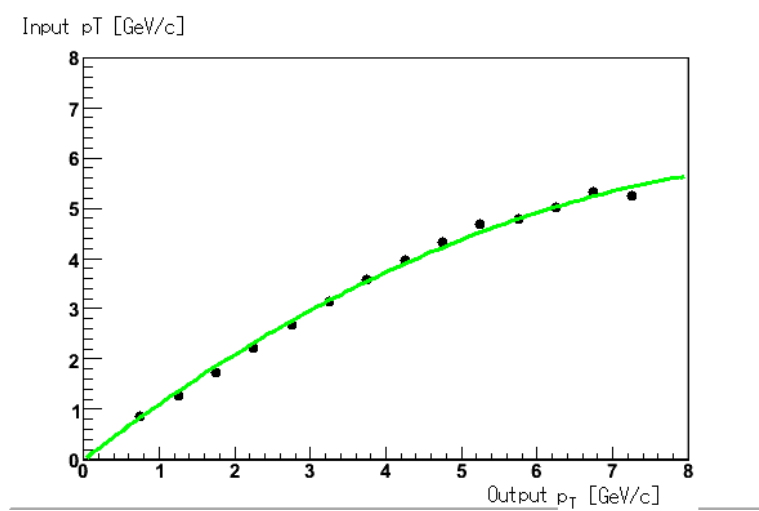


Figure 4.51: Input (real)  $p_T$  as a function of output (Measured)  $p_T$  of  $\Lambda$  in Geant simulation in PHENIX

## 4.11 New reaction plane resolution in PHENIX

4.2 billion events of  $\sqrt{s_{NN}} = 200$  GeV Au+Au collision was taken at RHIC-PHENIX experiment Run7 (2007). Reaction Plane detector (RxP) was installed before the running period. PHENIX has several detectors that can measure reaction plane although their resolutions are not so good except RxP. Figure 4.52 shows reaction plane resolutions of each detector for Au+Au  $\sqrt{s_{NN}} = 200$  GeV collision in Run7. These resolutions are estimated by 2-sub method or 3-sub method[32]. RxP provide good resolution 0.75 at maximum. It is two times of that of BBC which was used in Run4. It means the statistical error of  $v_2$  measurement is reduced to half of the current value with the same statistics. In addition, RxP provides good resolution estimation for other detectors. RxP which has the best resolution is used to measure  $v_2$  of identified hadrons in this analysis. Other detectors are used for systematic study of the resolution and flow measurement.

The charged hadrons  $v_2$  are measured at central arm ( $\eta < 0.35$ ). (Fig.4.55)

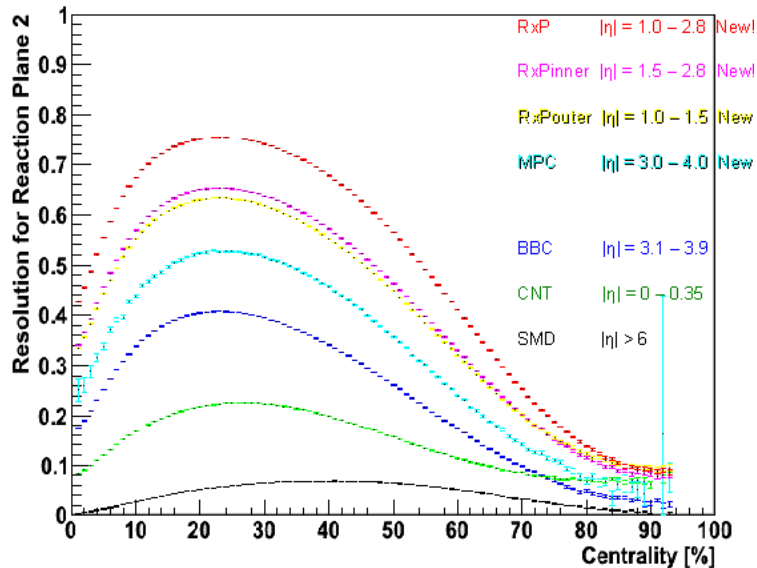


Figure 4.52: Event plane resolution as a function of centrality in Au+Au  $\sqrt{s_{NN}} = 200$  GeV. Red shows RxP, green shows MPC and blue shows BBC.

## 4.12 Systematic Error estimation

Systematic error of measured  $v_2$  are estimated in this section. The main uncertainty of  $v_2$  come from reaction plane. Systematic error of the reaction plane includes the uncertainty of reaction plane determination and correlation of jet effect. In addition, contamination from ghost track or mis-identified particle and systematical bias of  $v_2$  extraction method may contribute to increase the systematic error.

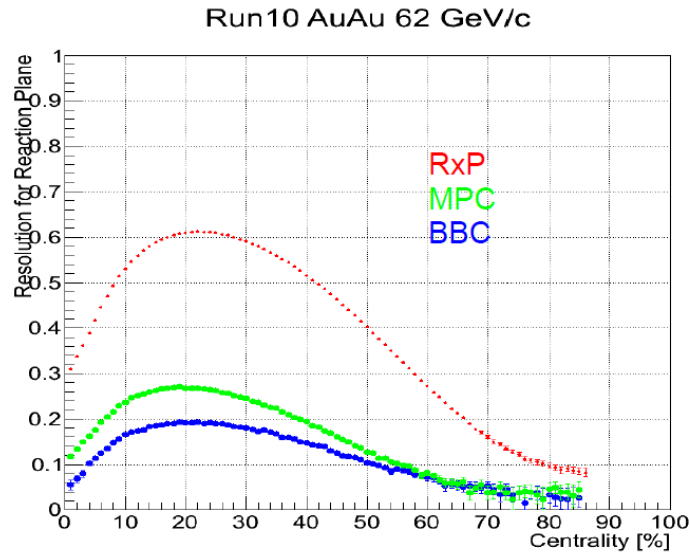


Figure 4.53: Event plane resolution as a function of centrality in Au+Au  $\sqrt{s_{NN}} = 62\text{GeV}$ . Red shows RxP, green shows MPC and blue shows BBC.

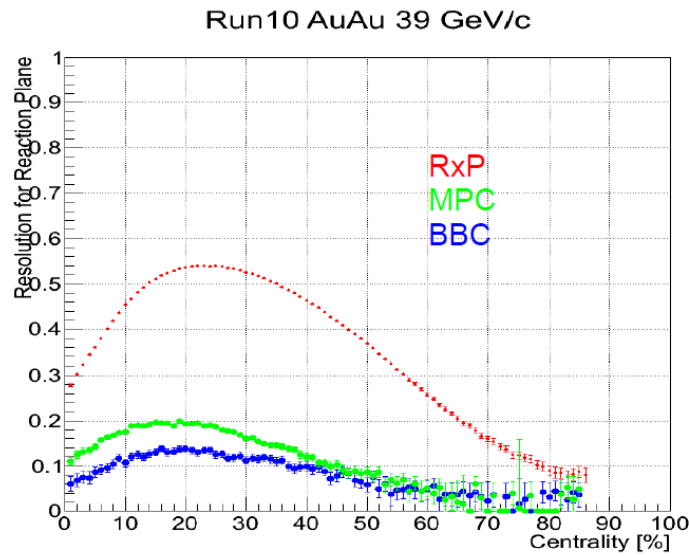


Figure 4.54: Event plane resolution as a function of centrality in Au+Au  $\sqrt{s_{NN}} = 39\text{GeV}$ . Red shows RxP, green shows MPC and blue shows BBC.

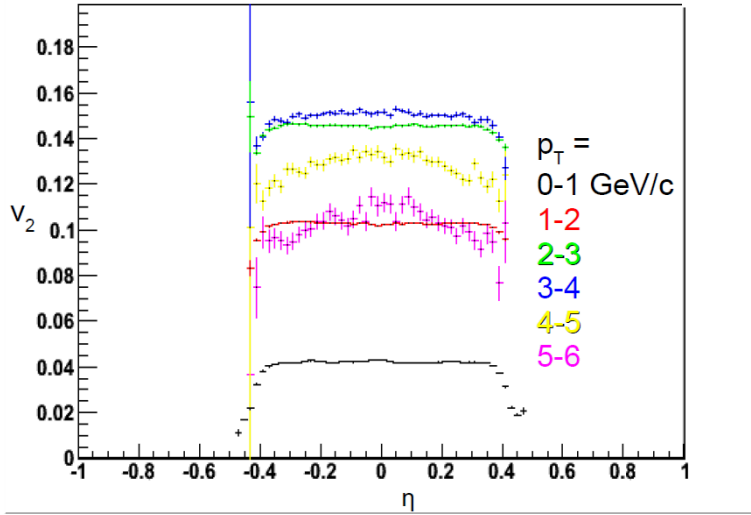


Figure 4.55: Charged hadron  $v_2$  as a function of  $\eta$  for each  $p_T$  range at minimum bias centrality.

#### 4.12.1 Auto-correlation and jet effect

Auto-correlation effect increases the measured  $v_2$  if some particles are used for both measurements of  $v_2$  and reaction plane. It is important that the different rapidity (or  $\eta$ ) acceptance are used to measure  $v_2$  from reaction plane detector to exclude such bias. A similar effect occurs in measured  $v_2$  when two different particles from a same source like a jet traverse the both of  $v_2$  detector and reaction plane detector. Figure 4.56 shows the charged hadron  $v_2$  which is measured as a function of centrality with event planes (measured reaction planes) from the different detectors. It provides jet correlation effect in measured  $v_2$  as a function of rapidity gap between the  $v_2$  and the event plane measurements.

$v_2$  value is affected by event plane coming from each rapidity acceptance. The jet bias is maximum when the central arm (CNT) is used to measure the reaction plane because of the very small  $\eta$ -gap between the measurements of  $v_2$  and reaction plane. The reconstructed tracks (particles) are sub-divided into  $\eta$ -slices, in order to have a particle of interest and the reaction plane from different  $\eta$ -slices. Figure 4.56 shows the measured  $v_2$  as the centrality of these detectors of PHENIX-Run7. These are consistent in the central collision event (centrality  $< 50\%$ ) except CNT. Figure 4.57 shows the comparison of centrality dependence of  $v_2$  measured with different event plane detectors for each  $p_T$  range and Fig.4.58 shows  $v_2$  as a function of  $p_T$  for each centrality range. Jet bias becomes remarkable to in the peripheral event that has small multiplicity. And the jet bias depends on  $p_T$  at centrality  $> 50\%$ .

#### 4.12.2 Uncertainty of Reaction Plane

The uncertainty of the reaction plane is estimated from differences of the measured  $v_2$  with the different event plane detectors. Figure 4.59 shows the difference of the  $v_2$  between RxP and other detectors. The difference does not strongly depend on  $p_T$  and the deviation is lower than almost 0.01 at 0 – 50%. At the peripheral (centrality  $> 50\%$ ), the difference that depends on  $p_T$  is seen in the fig.4.59. These two effects are used for the systematic error that include the jet bias and the

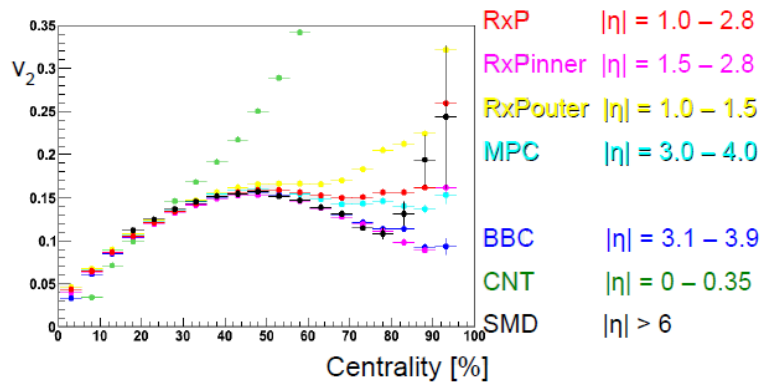


Figure 4.56:  $v_2$  as a function of centrality with each detector.

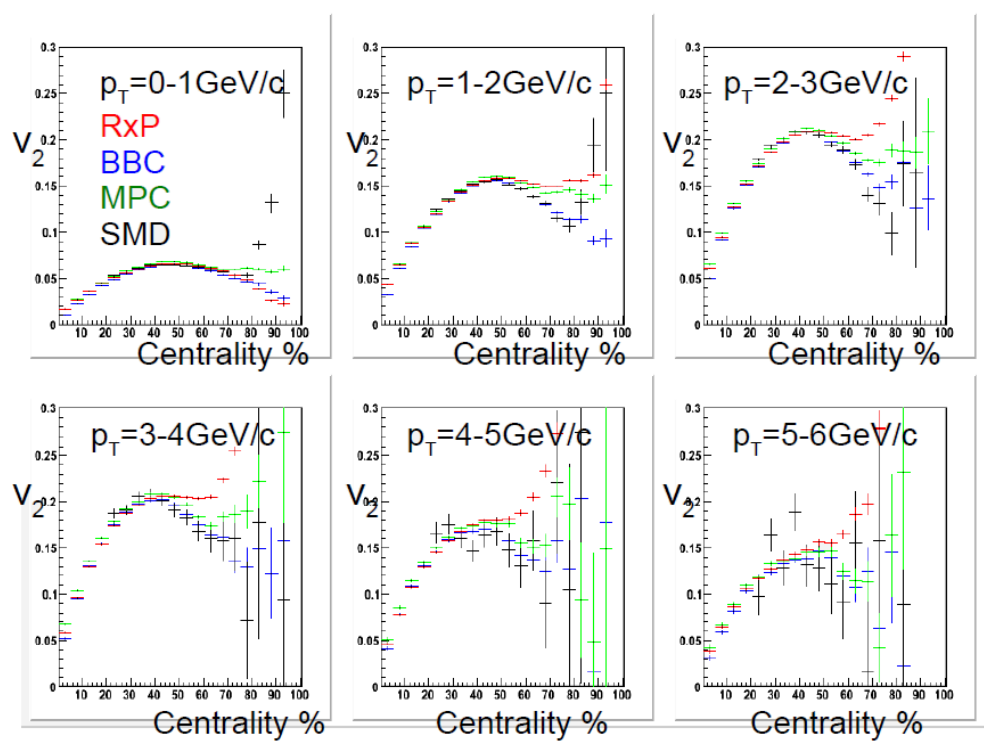


Figure 4.57:  $v_2$  as a function of centrality with each detectors at each  $p_T$  bin.

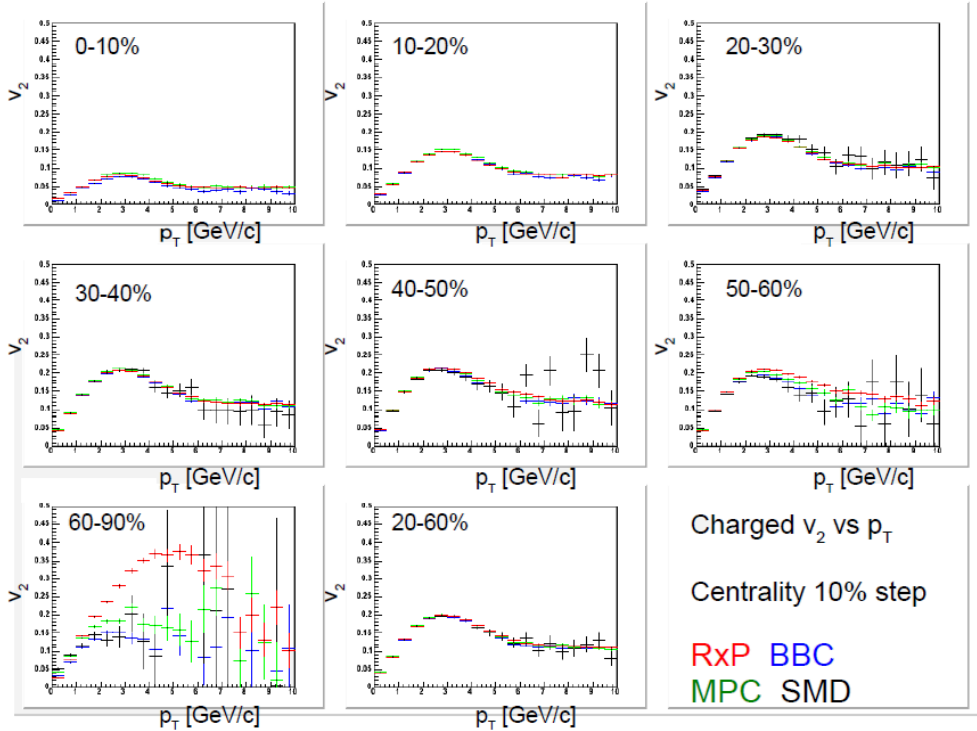


Figure 4.58:  $v_2$  as a function of  $p_T$  with each detectors at each centrality bin.

uncertainty for the reaction plane measurement of the detectors.

The most central collision events have a small amplitude of  $v_2$  since the small geometric anisotropy of collision. On the other hand, the most peripheral event has a large jet bias. Mid central collisions (20 – 60%) are suitable to measure elliptic flow  $v_2$  with small non-flow bias.

The measured  $v_2$  difference between RxP and BBC has been fitted by linear functions ( $\delta v_2^{chargedhadron} = A \times p_T$ ) and a constant A is extracted as -0.0043 for 50 – 60% centrality and -0.037 for 60 – 90% centrality. The  $p_T$  dependence of the  $v_2$  should only be discussed below 5GeV/c or in the central collisions (< 60%) because of the large background effect.

#### 4.12.3 Uncertainty of particle identification

Uncertainty of particle identification (PID) depends on the signal to noise ratio and it is estimated as difference between the  $v_2$  of each particle identification method (detector). It is defined as the difference between with ACC and without ACC for  $\pi$ -meson,  $K$ -meson and  $p$ . Or it is the difference between method of  $v_2$  measurement (background rejection) for  $\Lambda$ ,  $\phi$ -meson and  $d$ . Figure 4.60 and 4.61 show the identified hadron  $v_2$  of method difference for  $\pi$ ,  $K$  or  $p$ . The value of systematic error is higher than the statistical error at low  $p_T$  although it is lower than that from reaction plane. The  $v_2$  variation between analysis methods for  $\Lambda$ ,  $\phi$  and  $d$  are within statistical error for those particles. Then, the systematic error of the  $v_2$  of the three particles is smaller than the statistical error.

The systematic errors of the  $v_2$  measurement coming from the particle identification are shown in the following ( $\Delta v_2$ ).

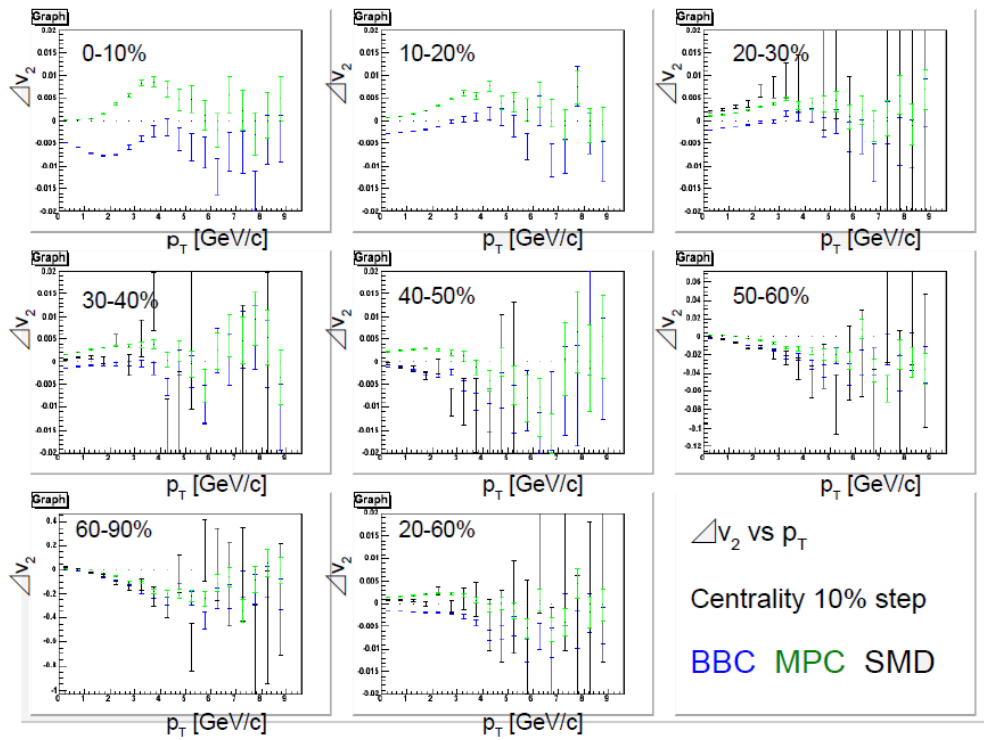


Figure 4.59:  $v_2$  difference between RxP and other detectors as a function of  $p_T$  for each centrality.

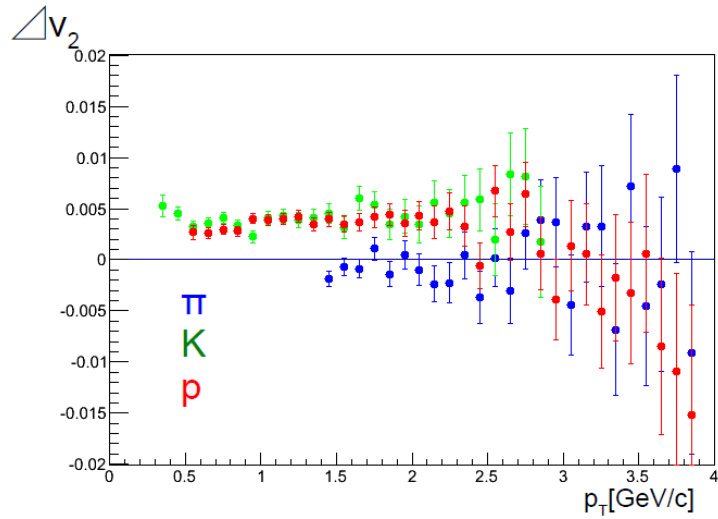


Figure 4.60:  $v_2$  difference as a function of  $p_T$  between with ACC and without ACC at centrality 20 – 60%. Red shows  $p$ , blue shows  $\pi$  and green shows  $K$ .

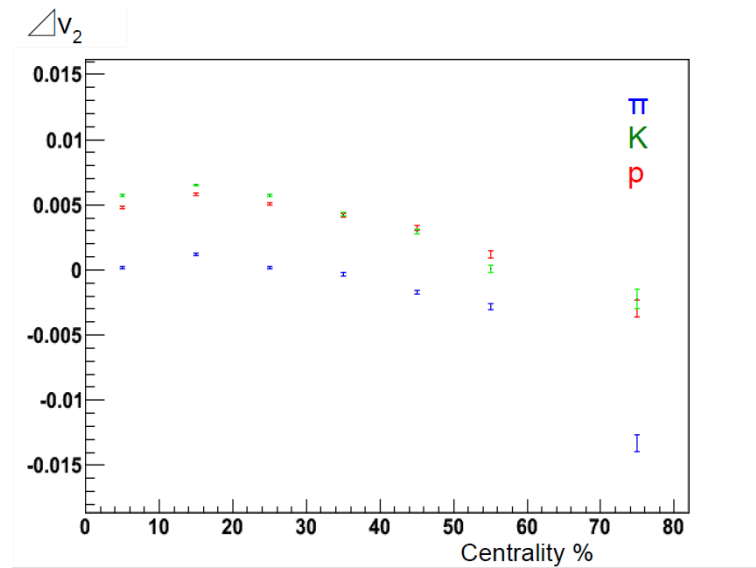


Figure 4.61:  $v_2$  difference as a function of centrality between with TOF+ACC and with TOF. Red shows  $p$ , blue shows  $\pi$  and green shows  $K$ .

$\pi$	
centrality (%)	$\Delta v_2$
0-10	0.00017
10-20	0.00118
20-30	0.00017
30-40	0.00033
40-50	0.00168
50-60	0.0028
60-90	0.0133
20-60	0.00086

$K$	
centrality (%)	$\Delta v_2$
0-10	0.0057
10-20	0.00650
20-30	0.00573
30-40	0.0042
40-50	0.0029
50-60	0.0000
60-90	0.0022
20-60	0.00384

$p$ centrality (%)	$\Delta v_2$
0-10	0.0048
10-20	0.00583
20-30	0.00503
30-40	0.0041
40-50	0.0032
50-60	0.0011
60-90	0.0029
20-60	0.00352

#### 4.12.4 Other Uncertainties

Additionally, other effects are considered for systematic error. Figure 4.62 shows  $d v_2$  with the calculation method (Method 1). The background  $v_2$  was measured at  $2.0 < M^2 < 3.0$  &  $4.5 < M^2 < 6.0$   $\text{GeV}^2/\text{c}^4$  in the method. The difference of the background  $v_2$  is also measured when different ranges are used for the background selection. The difference is negligible within statistical error. Figure 4.63 shows  $\Delta v_2$  difference among different normalization methods. Mix pair was normalized at  $IM < 1.1$  &  $IM > 1.13$   $\text{GeV}/\text{c}^2$ . Integral of Gaussian peak was calculated as number of the reconstructed  $\Lambda$  particles by the Gaussian fit for both real and mixed pairs. The  $v_2$  difference is investigated with various different normalization ranges. The difference is negligible within statistical error. The normalization range is also varied for  $\phi$ -meson in Fig.4.64. Gaussian fitting needs to be used to extract  $\phi$ -meson peak from two peaks for the ghost peak rejection. The difference is negligible within statistical error. The systematic error of uncertainty of particle identification and reaction plane are enough to estimate systematic uncertainty of measured  $v_2$ .

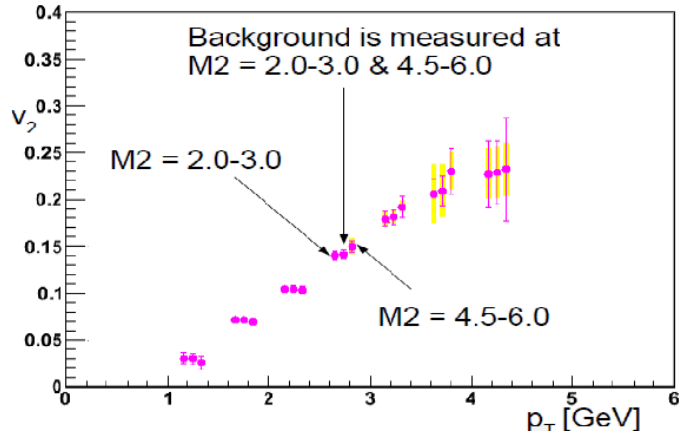


Figure 4.62:  $v_2$  as function of  $p_T$  of  $d$  by calculation method (Method 1). Points are shifted in the x-axis for other background estimation.

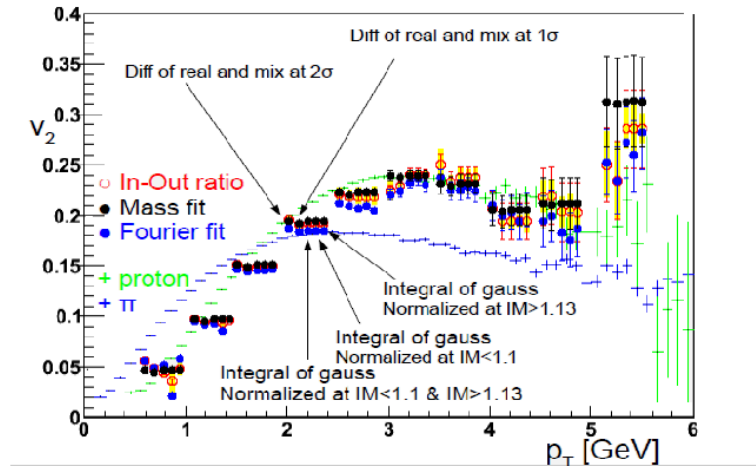


Figure 4.63:  $v_2$  as function of  $p_T$  of  $\Lambda$  by each method. Points are shifted in the x-axis for other background estimation.

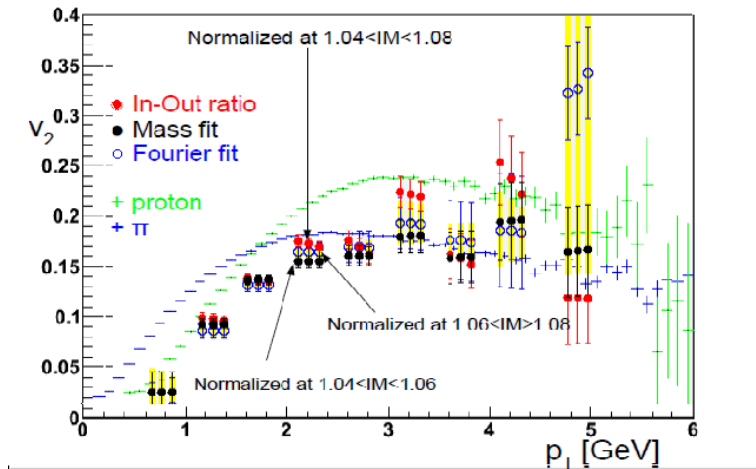


Figure 4.64:  $v_2$  as a function of  $p_T$  of  $\phi$ -meson by each method. Points are shifted in the x-axis for other background estimation.

# Chapter 5

## Result and discussions

### 5.1 The elliptic flow ( $v_2$ ) of hadrons as a function of transverse momentum ( $p_T$ ) in Au+Au $\sqrt{s_{NN}} = 200$ GeV

The  $v_2$  of identified particles ( $\pi^+$ ,  $\pi^-$ ,  $K^+$ ,  $K^-$ ,  $p$ ,  $\bar{p}$ ,  $\Lambda$ ,  $\bar{\Lambda}$ ,  $\phi$ ,  $d$  and  $\bar{d}$ ) were measured in Au+Au  $\sqrt{s_{NN}} = 200$  GeV collision at RHIC-PHENIX in 2007. Statistics of 4.2 billion events were obtained with the enhanced event plane resolution of the new reaction plane detector. Those results are shown in the following sections.

### 5.2 $KE_T$ and Quark number scaling

Figure 5.1 and 5.2 show the  $v_2$  as a function of  $p_T$  of the six particles. These values of  $v_2$  are average of particle and anti-particle. The  $p_T$  shift coming from the mass effect with the radial flow is often described by kinetic transverse energy ( $KE_T$ ) scaling ( $KE_T = m_T - m$ ). Figure 5.3 and 5.4 show the  $v_2$  as a function of  $KE_T$ . It seems to be consistent with each other separately for mesons or baryons in all centralities. The  $v_2$  as a function of  $p_T$  for  $d$  deviates further from the  $v_2$  of both of the mesons and the baryons. The consistency seems to be given for all hadrons including  $d$ , when scaling the both  $v_2$  and  $KE_T$  by the number of consistent quarks. Figure 5.5 and 5.6 show the  $v_2/n_q$  as a function of  $KE_T/n_q$  for each centrality selections.

Figure 5.7 and 5.8 show the ratio of the scaled  $v_2$  with respect to the polynomial function fitted to the pion data. Figure 5.9 to 5.12 show the  $v_2/n_q$  is plotted as a function of  $p_T/n_q$ . The  $v_2/n_q$  as a function of  $KE_T/n_q$  of all of the particles seem to be consistent within error at  $KE_T/n_q < 0.7\text{GeV}$  with  $KE_T$  and quark number scaling in all centrality ranges. This indicates the quark level collectivity in QGP and the  $v_2$  of the particles is given by the sum of quark  $v_2$  during QGP-hadron phase transition according to the quark coalescence model. The  $v_2/n_q$  as function of  $KE_T$  of  $p$  may have difference about 10% from that of  $\pi$ . However more detailed comparison is not feasible because of the large systematic error which is caused by reaction plane measurement and small absolute value of  $v_2$ . There is no guarantee that  $KE_T$  scaling can completely explain the  $p_T$  shift which could vary by the magnitude of the radial flow, although the agreement seems to be better in the  $KE_T/n_q$  scaling than in the  $p_T/n_q$  scaling. The  $\phi$ -meson could provide a pure  $v_2$  information from the QGP phase because of its small hadronic cross sections with light hadrons. It is found to be consistent with other hadrons with  $KE_T/n_q$ , too. The  $v_2$  of  $\phi$ , which consists of two quarks and have heavy mass, is similar to meson than baryon. Therefore the agreement of the

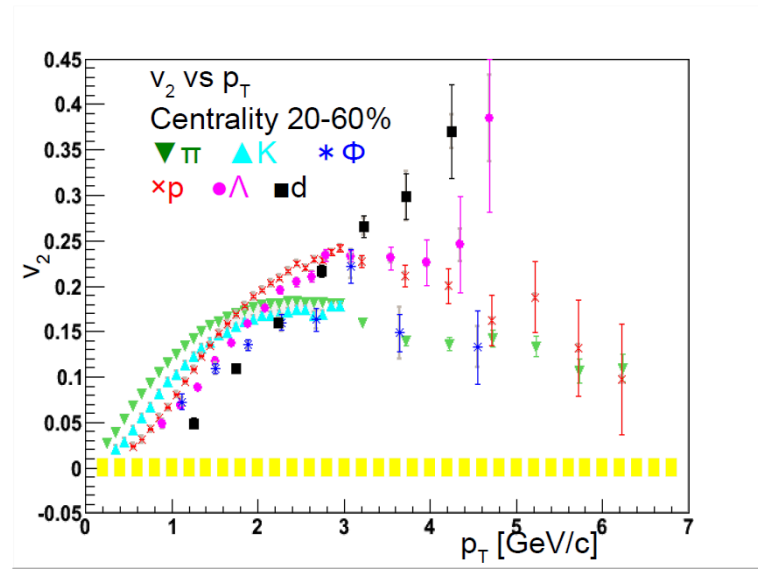


Figure 5.1:  $v_2$  as a function of  $p_T$  of identified six particles at centrality 20 – 60%.

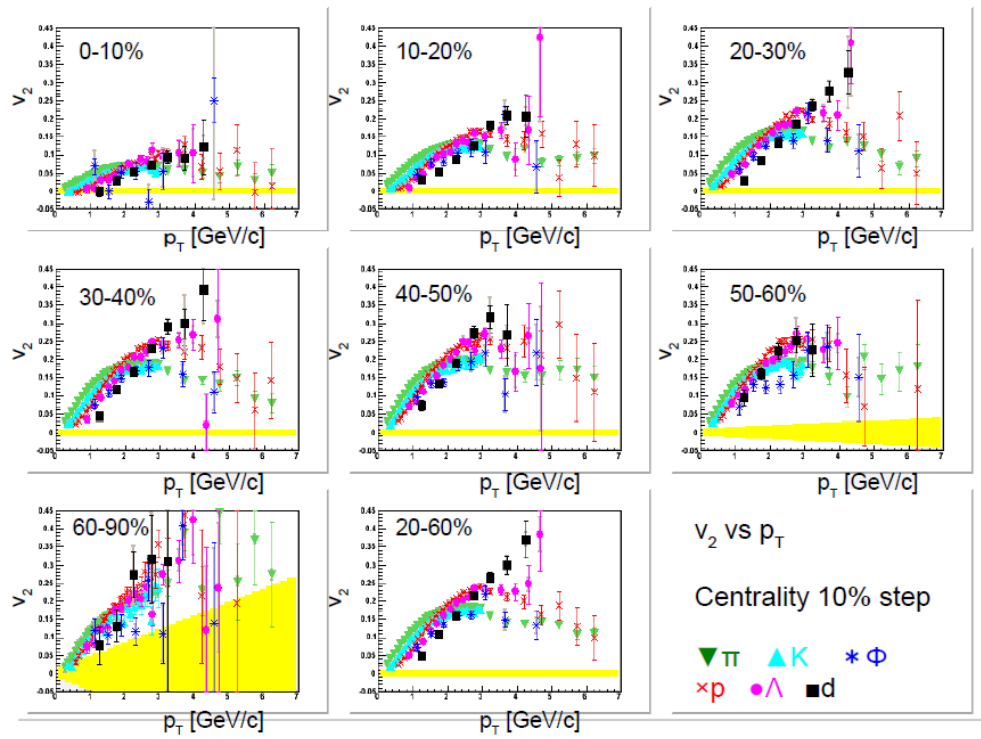


Figure 5.2:  $v_2$  as a function of  $p_T$  of identified six particles for each centrality range.

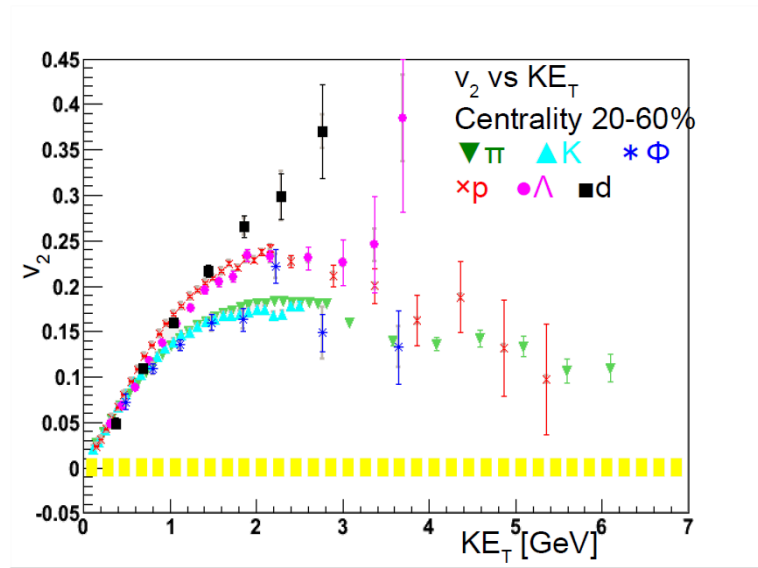


Figure 5.3:  $v_2$  as a function of  $KE_T$  for identified six particles at centrality 20 – 60%.

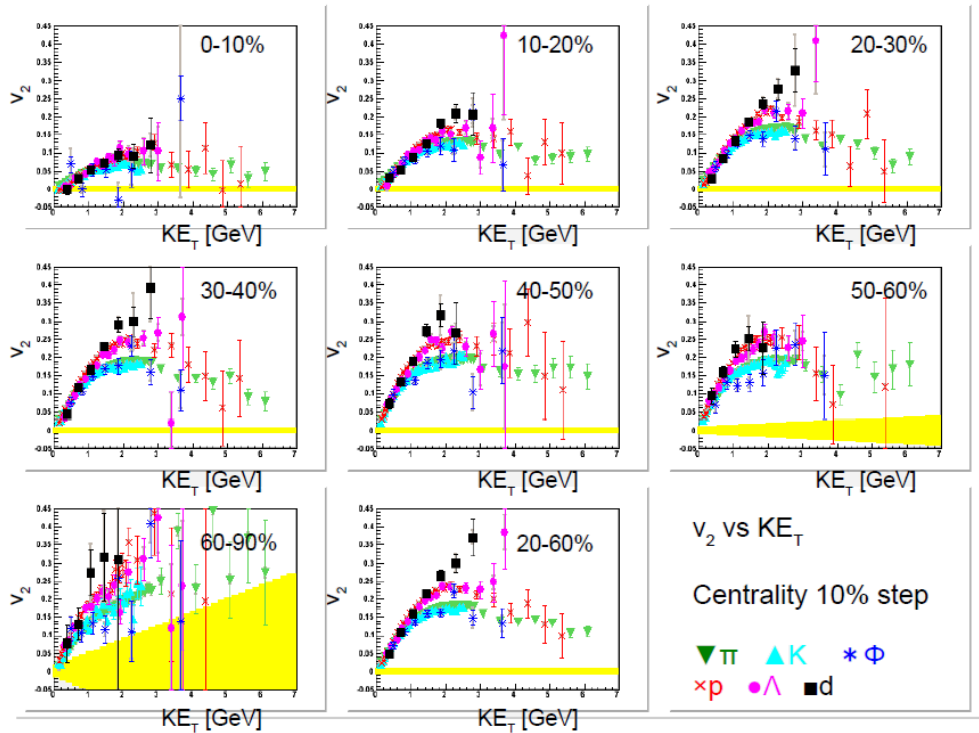


Figure 5.4:  $v_2$  as a function of  $KE_T$  for identified six particles for each centrality range.

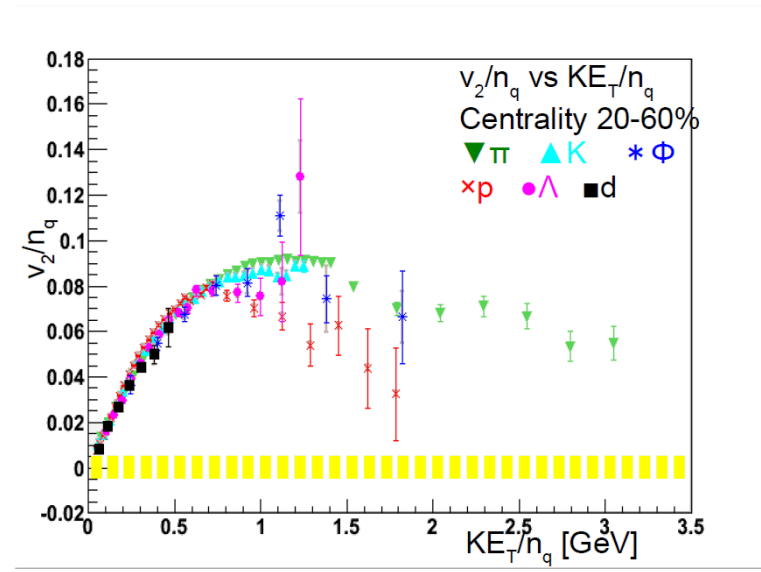


Figure 5.5:  $v_2/n_q$  as a function of  $KE_T/n_q$  for identified six particles at centrality 20 – 60%.

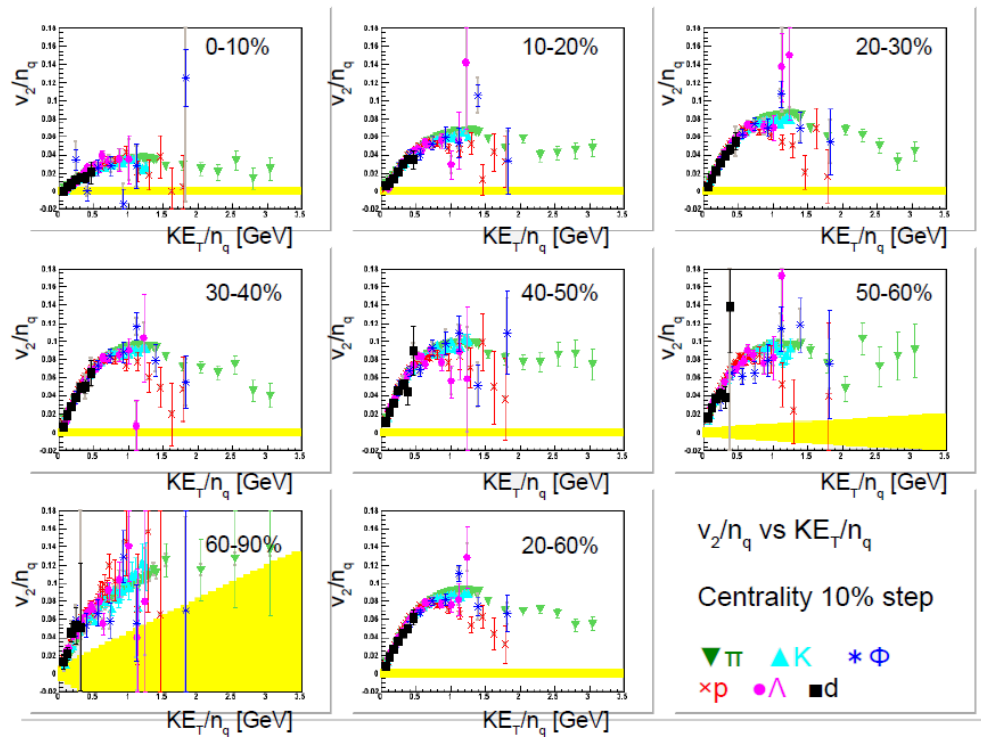


Figure 5.6:  $v_2/n_q$  as a function of  $KE_T/n_q$  for identified six particles for each centrality range.

scaled  $v_2$  of  $\phi$  with the other hadrons would support the idea of  $v_2$  formation during the QGP phase before the hadronic phase.

Conversely, the disagreement between them for  $v_2$  with  $KE_T/n_q$  scaling at the high momentum ( $KE_T/n_q > 0.7$  GeV) is remarkable. It is found that  $v_2$  of  $\pi$  and  $p$  are approaching with each other at high  $p_T$  without quark number scaling. It could be strong evidence of totally different mechanism for  $v_2$  generation from hard process compared with soft region at low  $p_T$ . Hard  $v_2$  of high momentum particles originated from jet might be generated by a path length dependence of jet-quenching (partonic energy-loss) in the dense medium, which would also have anisotropic geometry.

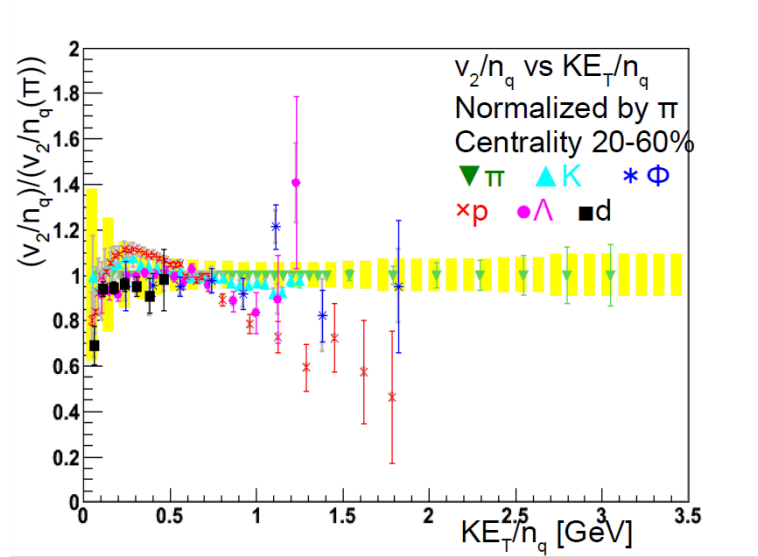


Figure 5.7: Ratio of  $v_2/n_q$  of each hadron to that of  $\pi$  as a function of  $KE_T/n_q$  at centrality 20 – 60%.

### 5.3 Blast wave fitting

Temperature, radial velocity and the eccentricity of the system at freeze-out are extracted by the blast-wave fitting to a  $p_T$  spectra and the  $v_2$  of the six particles. Figure 5.13 and 5.14 show the  $p_T$  spectra+ $v_2$  fitting for each centrality range. Figure 5.15 shows the extracted parameters. The radial flow velocity increases in the central collision. The freeze-out temperature is 150 MeV and it seems to be flat as a function of centrality. Figure 5.16, 5.17 show the density distribution and velocity profile distribution defined as gradient of the density distribution, the both figures indicate before (initial Glauber distribution, top) and after (result of the fit, bottom) the expansion of the system. Figure 5.18 shows the extracted eccentricity of the system at freeze-out timing. The final eccentricity is smaller than initial eccentricity of Glauber model. It is a result of matter expansion before freeze-out. The final eccentricity is compared with the result of HBT analysis which also measures the shape and size of the collision system at the freeze-out with two particle correlation. These results of both of the HBT and the blast-wave fitting of the  $v_2$  measurements are consistent with each other.

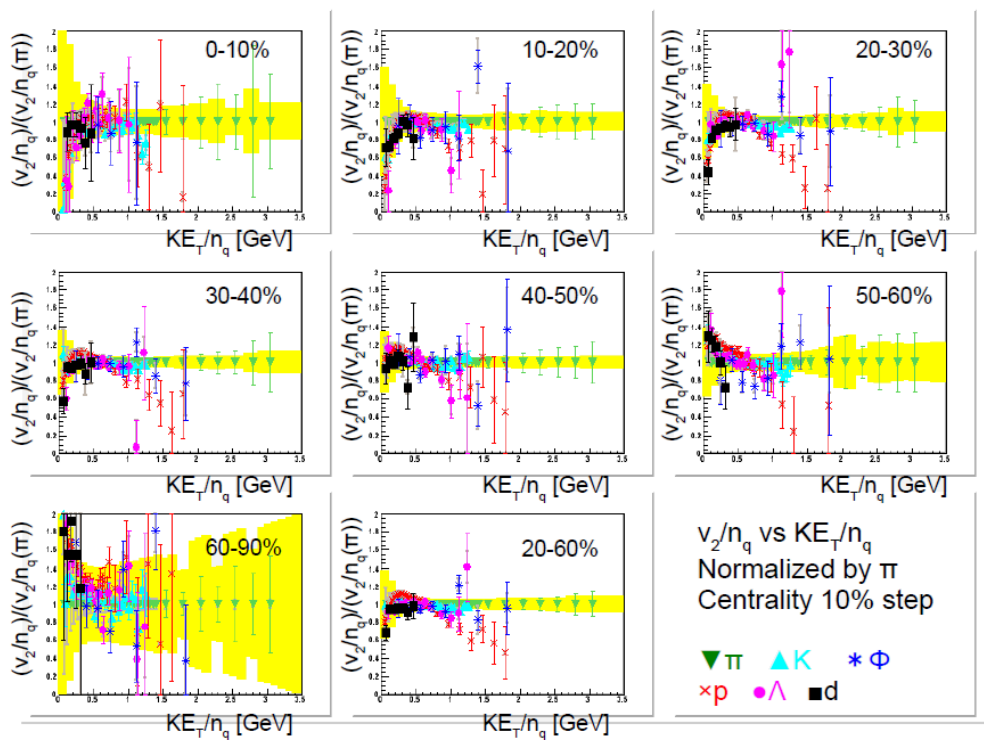


Figure 5.8: Ratio of  $v_2/n_q$  of each hadron to that of  $\pi$  as a function of  $KE_T/n_q$  for each centrality range.

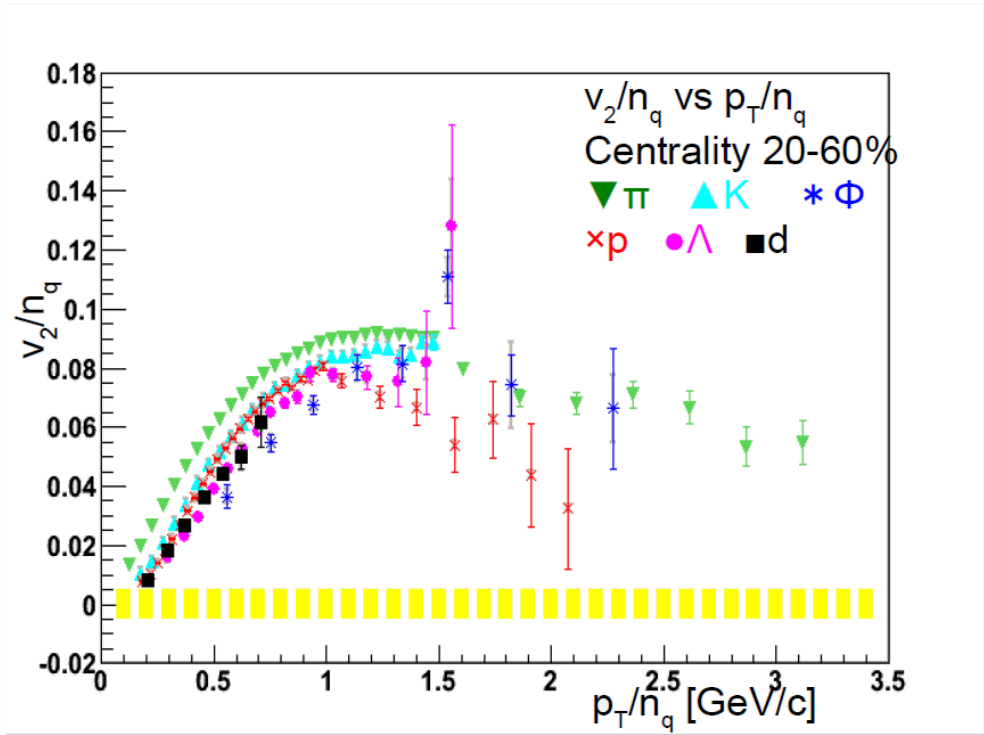


Figure 5.9:  $v_2/n_q$  as a function of  $p_T/n_q$  for identified six particles at centrality 20 – 60%.

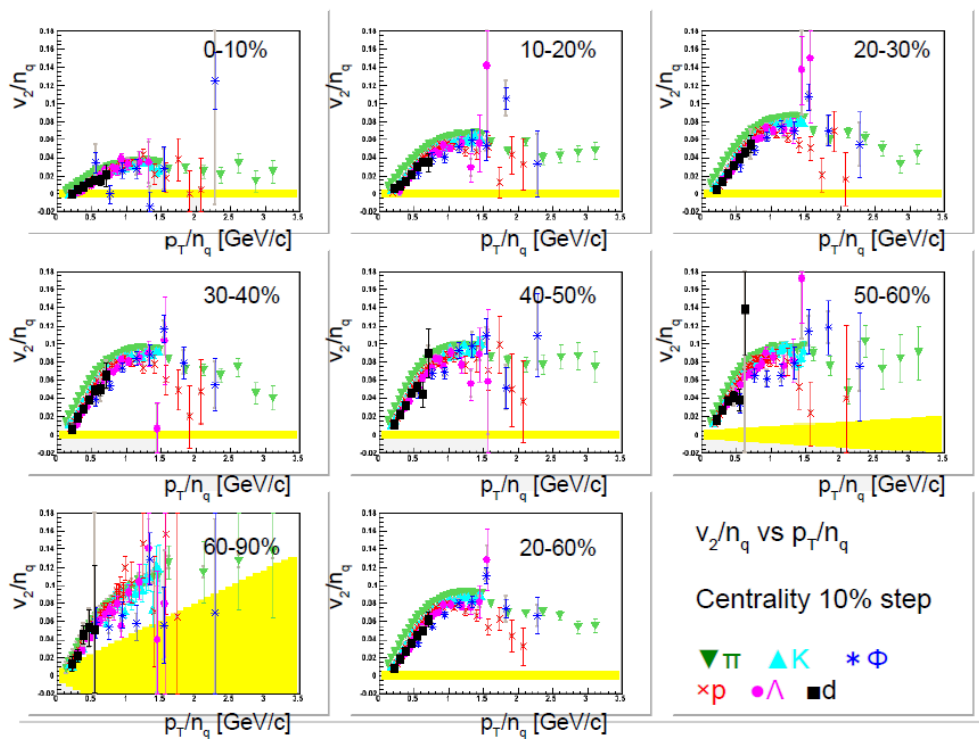


Figure 5.10:  $v_2/n_q$  as a function of  $p_T/n_q$  for identified six particles for each centrality range.

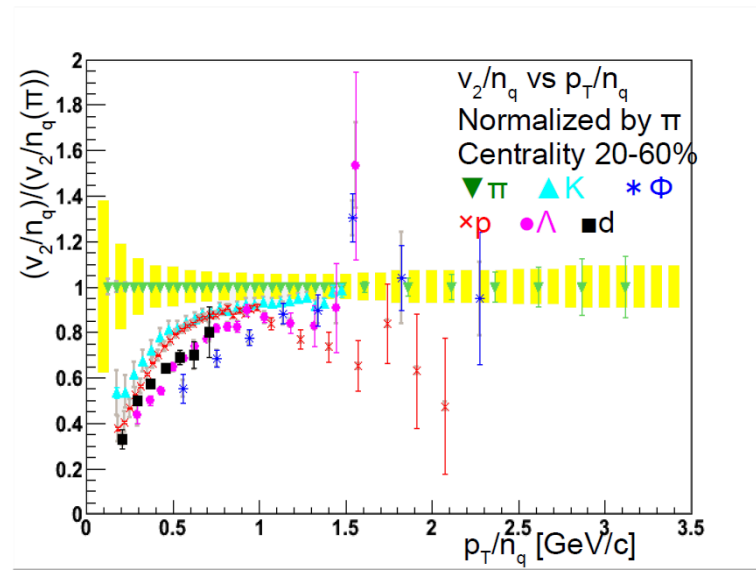


Figure 5.11:  $v_2/n_q$  as a function of  $p_T/n_q$  for identified six particles at centrality 20 – 60%.

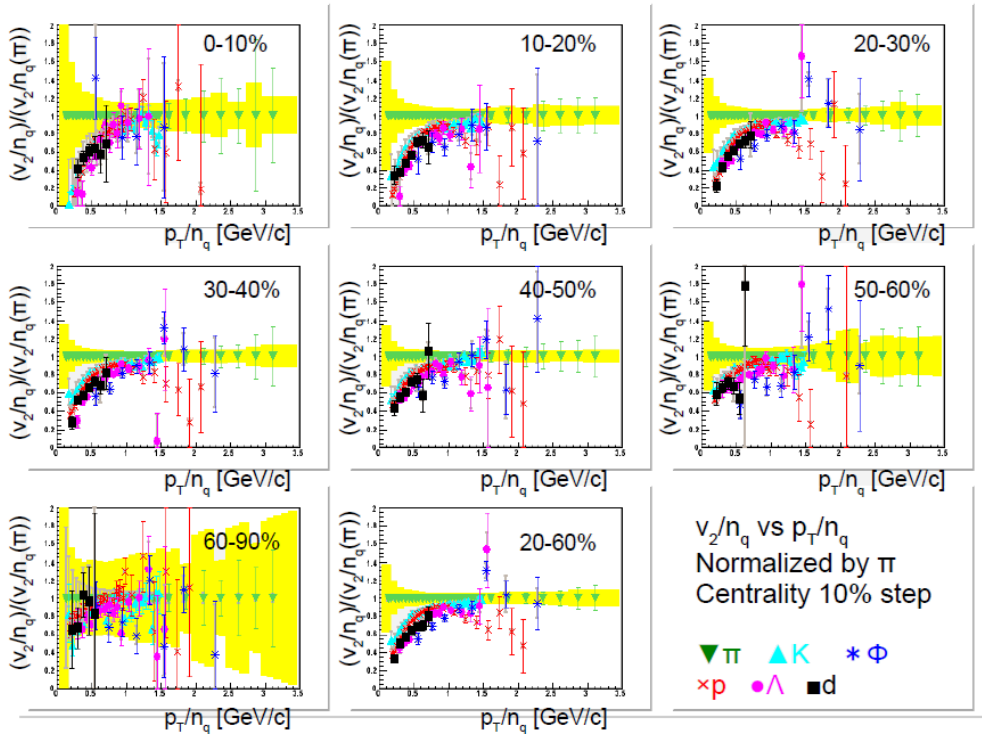


Figure 5.12:  $v_2/n_q$  as a function of  $p_T/n_q$  for identified six particles for each centrality ranges.

## 5.4 comparison between particles

### 5.4.1 $p$ and $d$

It is expected that  $d$  is formed by coalescence of  $p$  and  $n$  during the final stage of collision since the smaller binding energy rather than that of quarks in hadron.  $d$  and  $p$  can be compared with nucleon number scaling because  $p$  mass is similar to  $n$ . Figure 5.19 - 5.24 show the  $v_2$  as a function of  $p_T$  and the nucleon number scaling ( $v_2/2$  and  $p_T/2$  for  $d$ ).  $d$  has larger  $v_2$  than  $p$  in high  $p_T$  range ( $> 3$  GeV/c). They are almost consistent within the error with the nucleon number scaling for each centrality. This tells us that the  $v_2$  of  $n$  is same as the  $v_2$  of  $p$  and they form  $d$  according to the coalescence model. The  $v_2$  measurements of  $d$  do not provide the evidence of judgment of  $p$ - $n$  coalescence or six quarks coalescence at this momentum range. There is a theoretical expectation that the  $v_2$  value from  $p$ - $n$  coalescence would decrease because it is affected by the hadronic scattering during evolution through the hadron phase at very high momentum range ( $> 7$  GeV). But, much higher statistics than Run7 would be required to confirm the small difference expected between these scenarios[38]. The  $v_2$  of  $d$  seems to be slightly smaller than  $p$  ( $\sim 0.87\%$ ) with nucleon number scaling at centrality 20 – 60%.

### 5.4.2 $p$ and $\Lambda$

Figure 5.25 - 5.32 show the  $v_2$  and the scaled  $v_2$  and their ratios of  $p$ ,  $\Lambda$  and  $d$ . The  $v_2$  of  $p$  and  $\Lambda$  (and  $d$  with nucleon number scaling) is almost consistent with each other within error. The ratio of the  $v_2$  as a function of  $p_T$  of  $\Lambda$  over  $p$  is maximum of about 28 %. The ratio of the  $v_2$  as a function

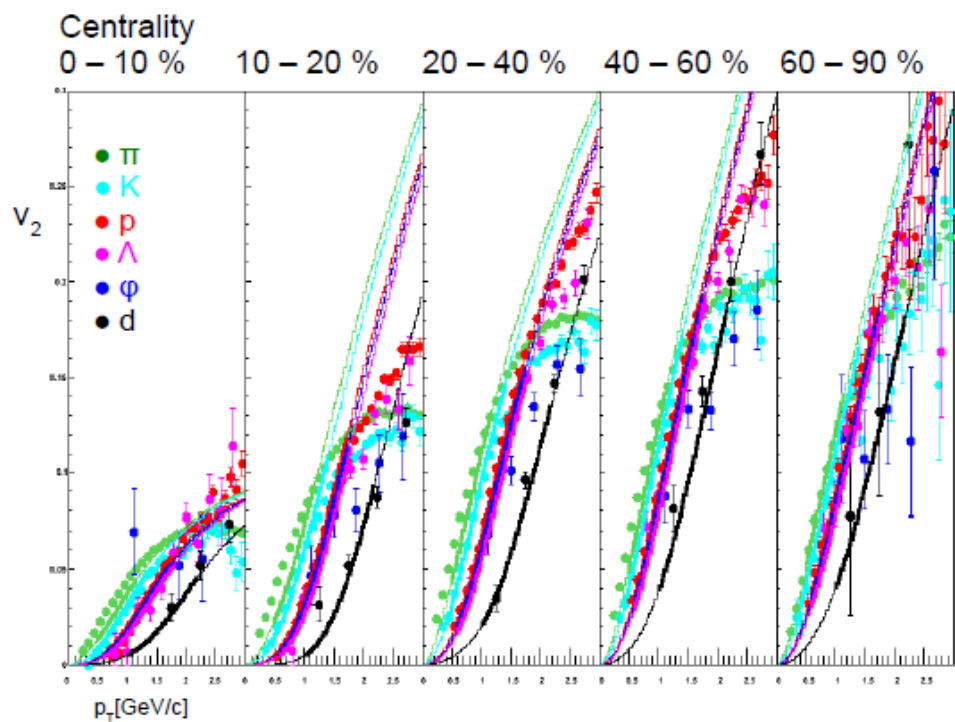


Figure 5.13:  $v_2$  as a function of  $p_T$  with fit lines of blast-wave spectra+ $v_2$  fitting. Wide line means fit  $p_T$  range.

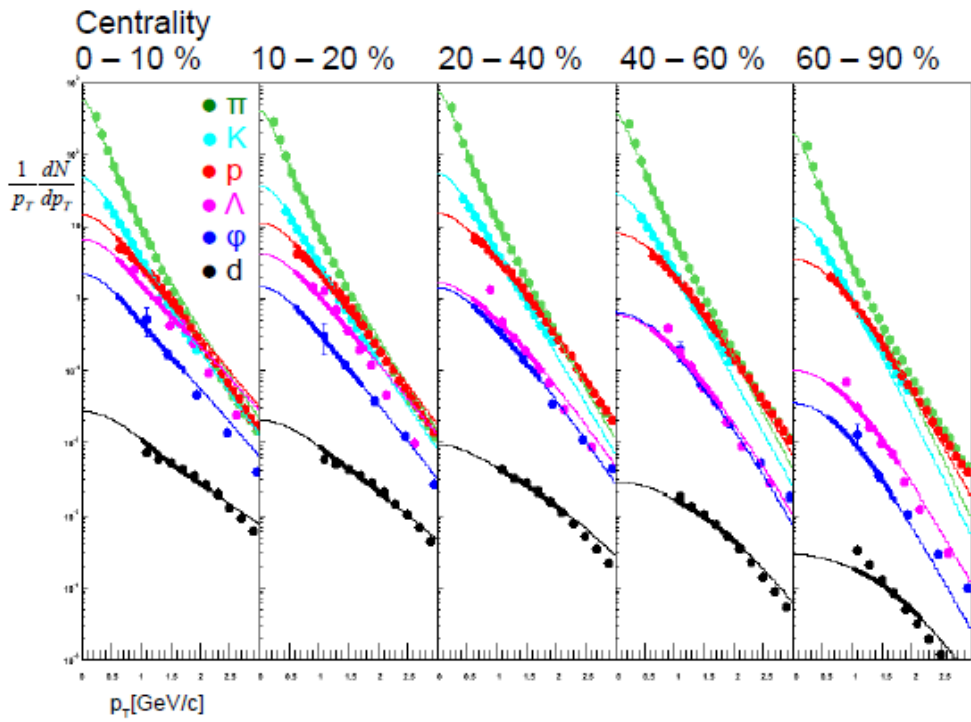


Figure 5.14:  $p_T$  spectra with fit lines of blast-wave spectra+ $v_2$  fitting for each centrality range. Wide line means fit  $p_T$  range.

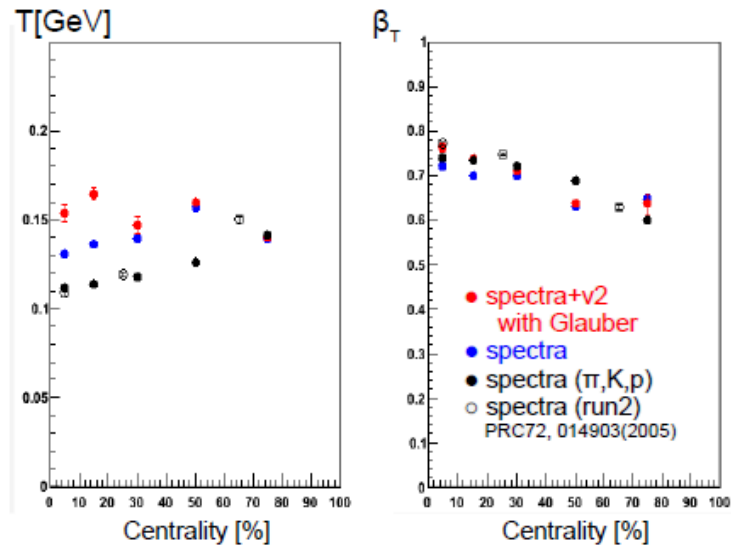


Figure 5.15: Left panel shows freeze out temperature as a function of centrality. Right panel shows radial velocity as a function of centrality. These were extracted by blast-wave fitting.

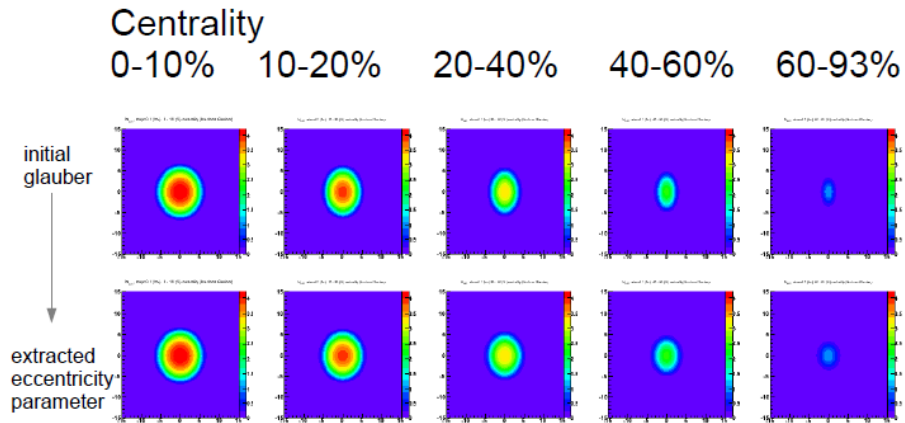


Figure 5.16: Top panels show the number of participant distributions which is estimated by Glauber Monte Carlo with Wood-Saxon distribution at initial stage of Au+Au collision. Bottom panels show the distributions which is estimated by blast-wave fitting and is expanded in x-axis.

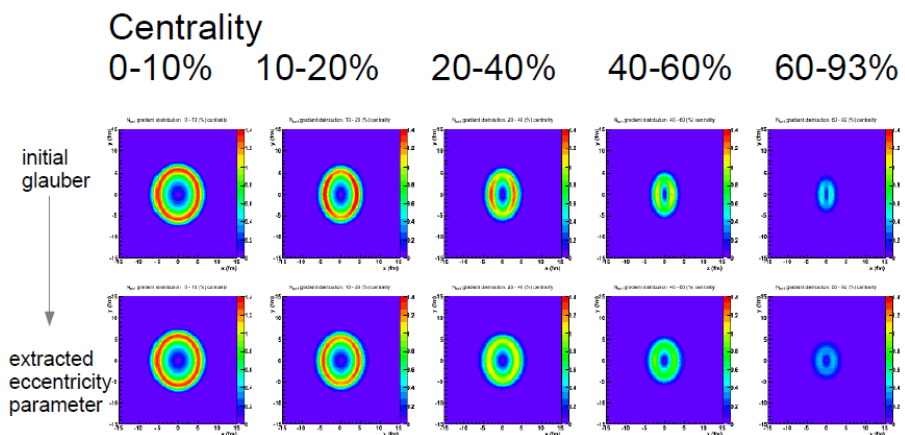


Figure 5.17: Gradient distributions of the number of participant distributions of Fig.5.6.

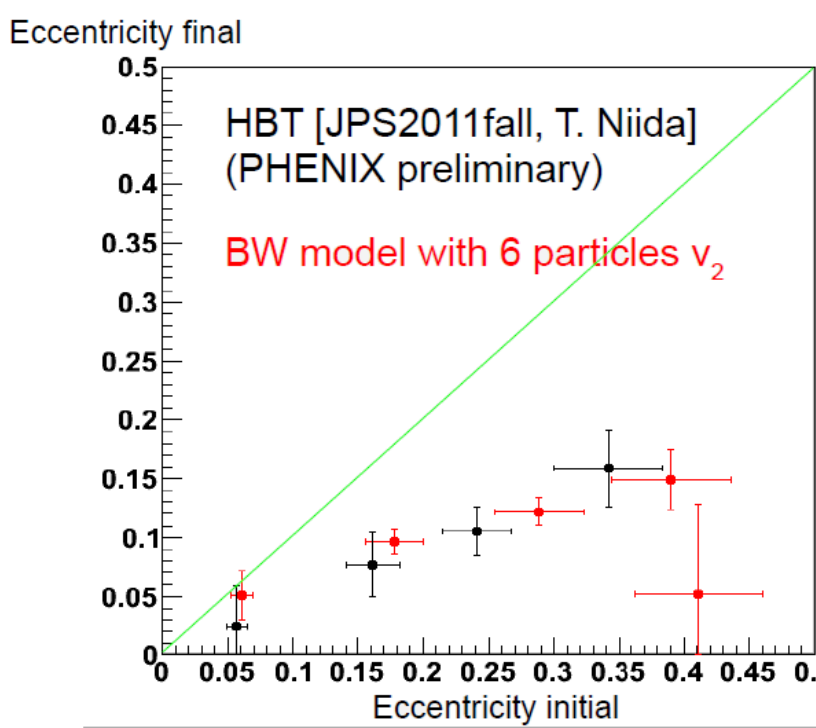


Figure 5.18: The final (freeze-out) eccentricity as a function of the initial eccentricity. Red shows the result of blast-wave fitting with measured spectra and  $v_2$ . Black shows measured eccentricity with pion emission by HBT method.

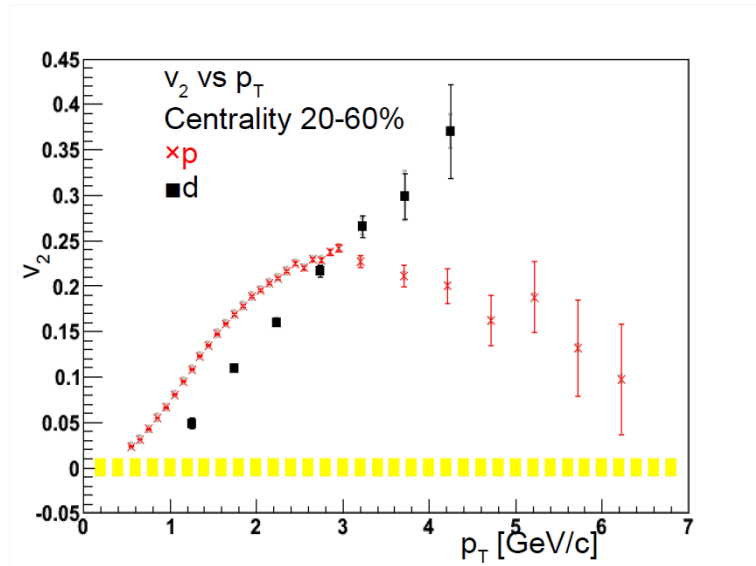


Figure 5.19:  $v_2$  as a function of  $p_T$  for  $(anti-)p$  and  $(anti-)d$  at centrality  $20 - 60\%$ .

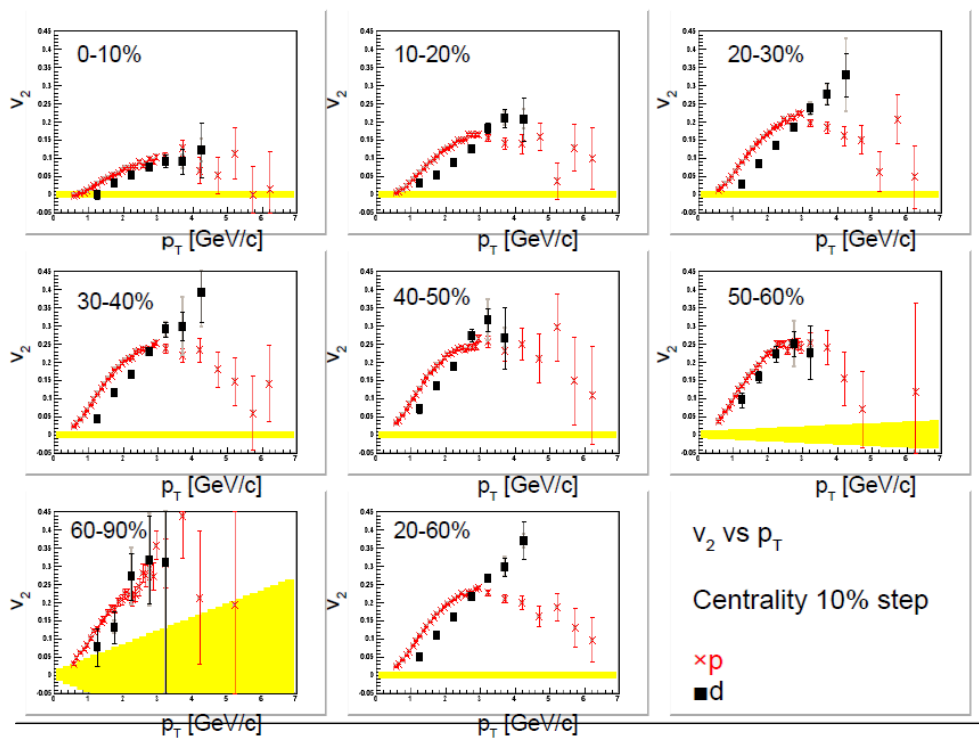


Figure 5.20:  $v_2$  as a function of  $p_T$  for  $(anti-)p$  and  $(anti-)d$  for each centrality range.

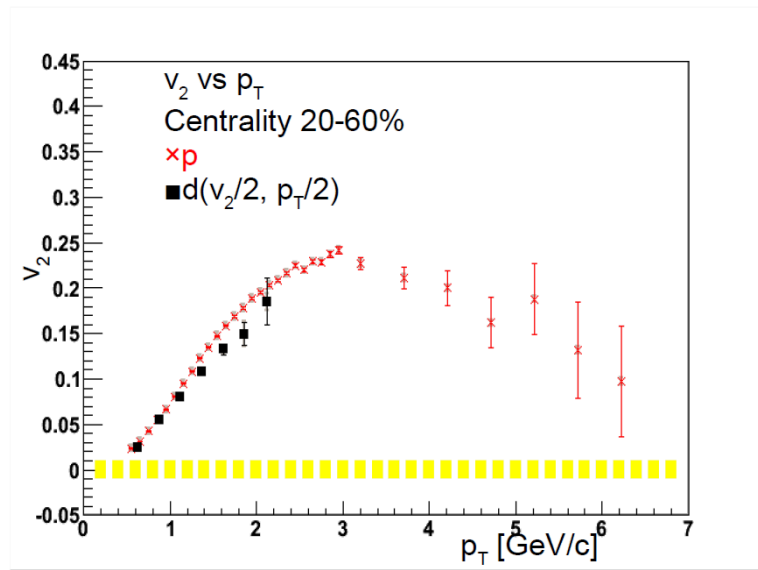


Figure 5.21:  $v_2/n_a$  as a function of  $p_T/n_a$  for  $(anti-)p$  and  $(anti-)d$  at centrality 20 – 60%.

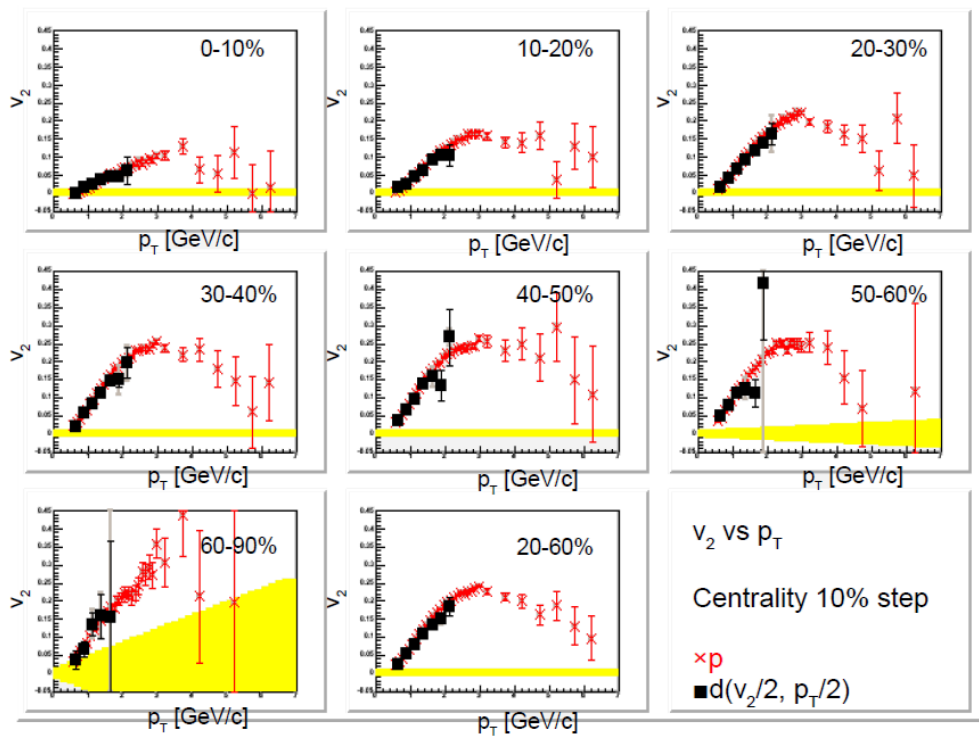


Figure 5.22:  $v_2/n_a$  as a function of  $p_T/n_a$  for  $(anti-p)$  and  $(anti-d)$  for each centrality ranges.

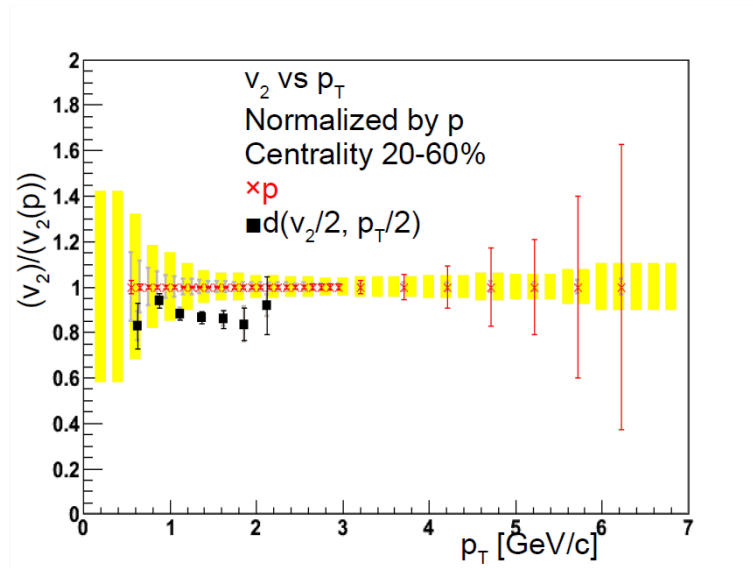


Figure 5.23: Ratio of  $v_2/n_a$  of  $(anti-d)$  to that of  $(anti-p)$  as a function of  $p_T/n_a$  at centrality 20 – 60%.

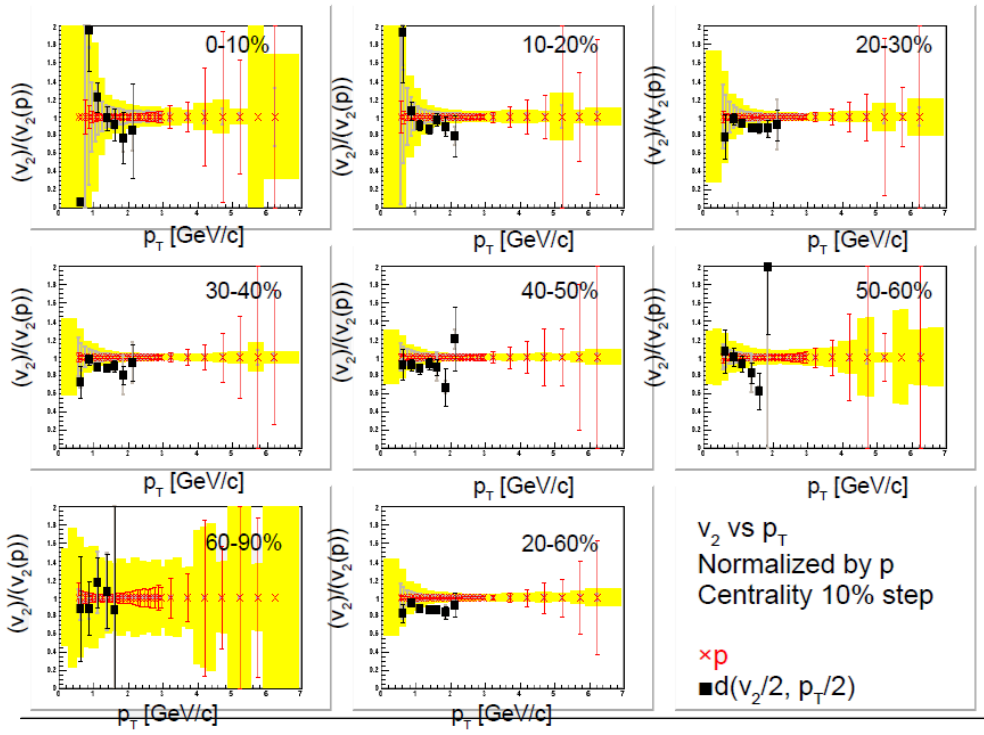


Figure 5.24: Ratio of  $v_2/n_a$  of  $(anti-)d$  to that of  $(anti-)p$  as a function of  $p_T/n_a$  for each centrality range.

of  $KE_T$  of these is maximum of about 20 %. The shape of  $v_2$  as a function of  $p_T$  of these two baryons are similar in all centrality ranges. But  $KE_T$  scaling does not describe the  $p_T$  shifts so well compared to mesons as discussed in the following sections.

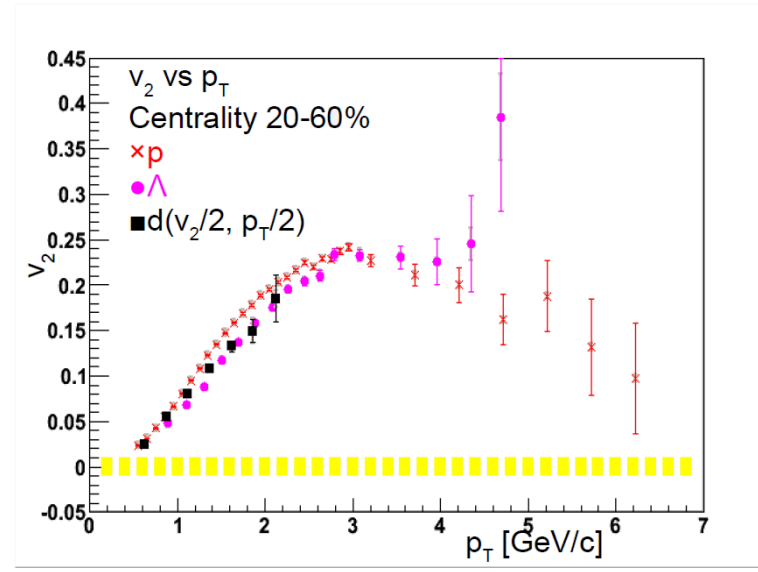


Figure 5.25:  $v_2/n_a$  as a function of  $p_T/n_a$  of baryons at centrality  $20 - 60\%$ .

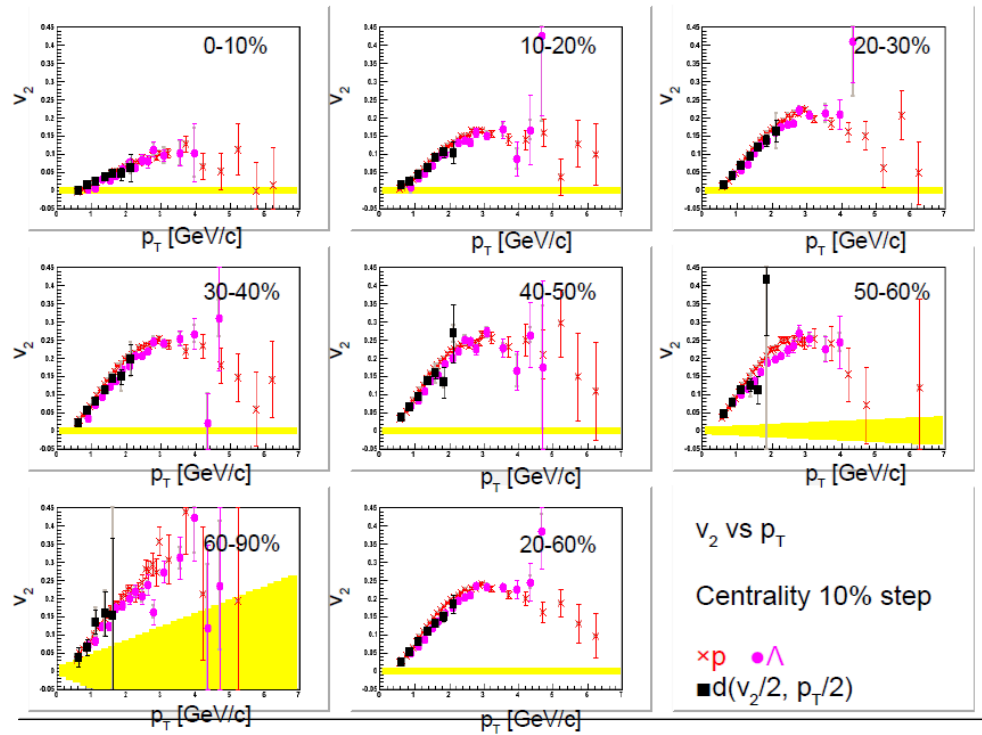


Figure 5.26:  $v_2/n_a$  as a function of  $p_T/n_a$  of baryons for each centrality ranges.

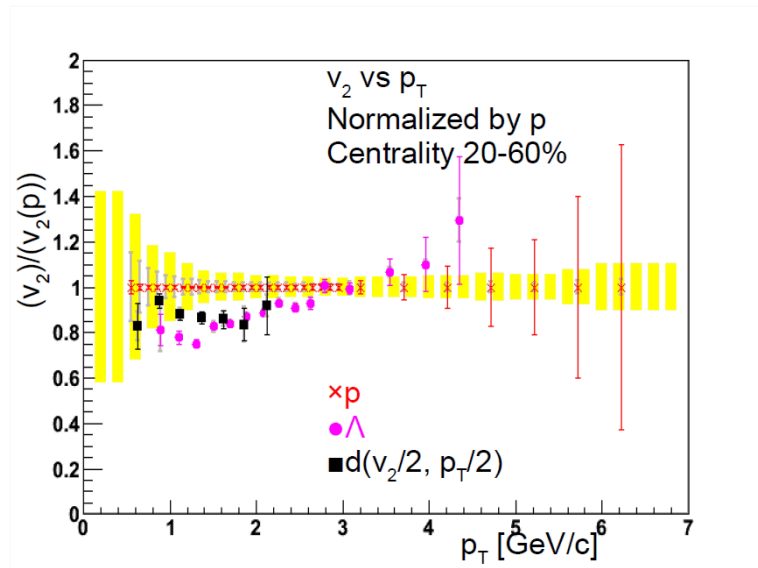


Figure 5.27: Ratio of  $v_2/n_a$  of baryons to that of  $(anti-)p$  as a function of  $p_T/n_a$  at centrality  $20 - 60\%$ .

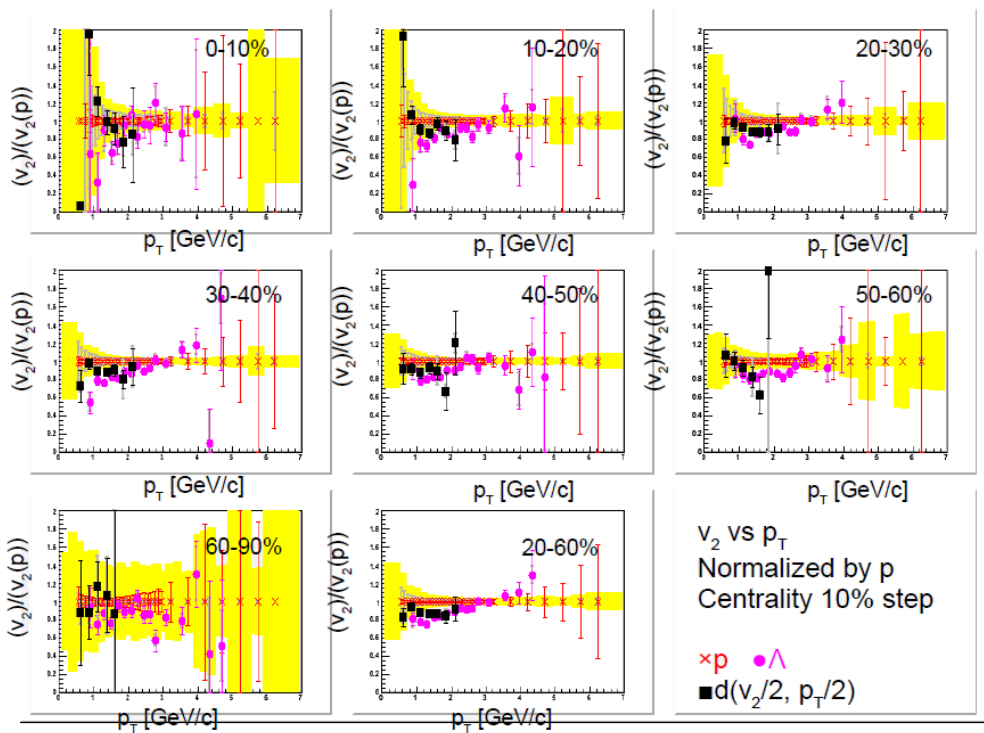


Figure 5.28: Ratio of baryons  $v_2/n_a$  to that of  $(anti-)p$  as a function of  $p_T/n_a$  for each centrality ranges.

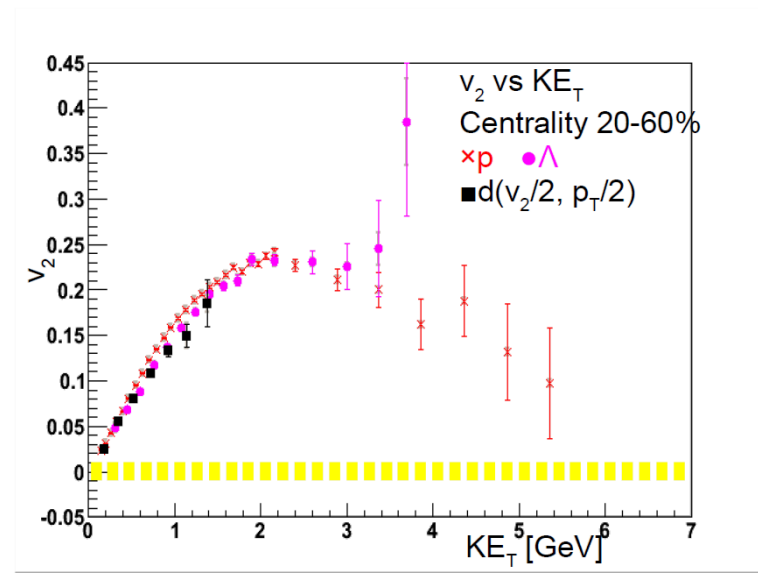


Figure 5.29:  $v_2/n_a$  as a function of  $KE_T/n_a$  for baryons at centrality 20 – 60%.

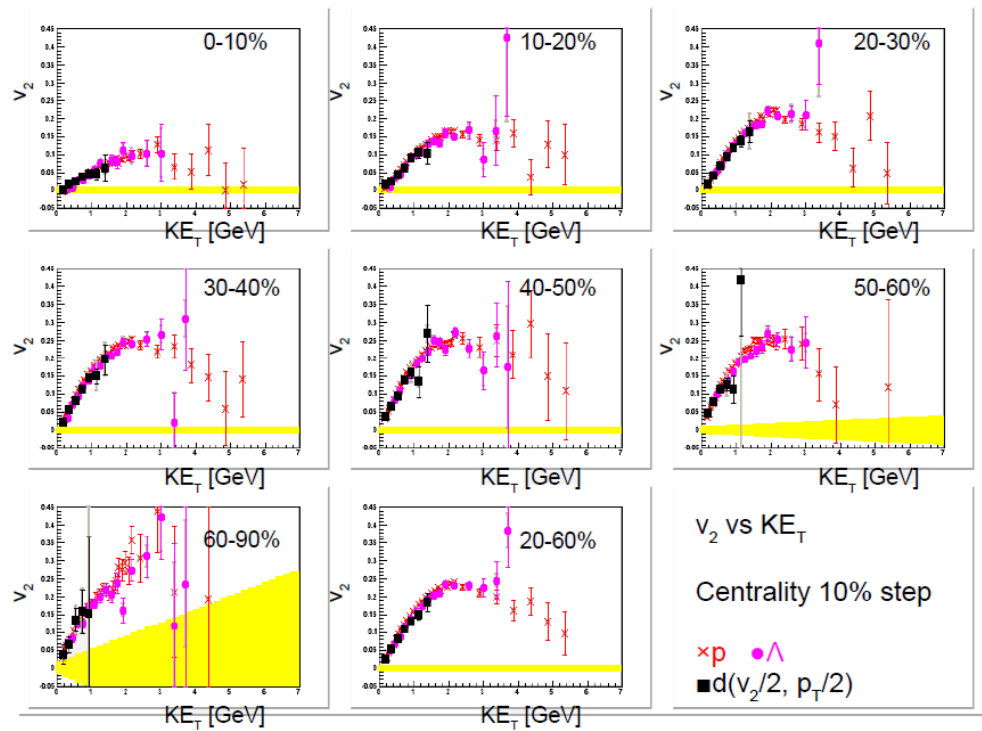


Figure 5.30:  $v_2/n_a$  as a function of  $KE_T/n_a$  for baryons for each centrality ranges.

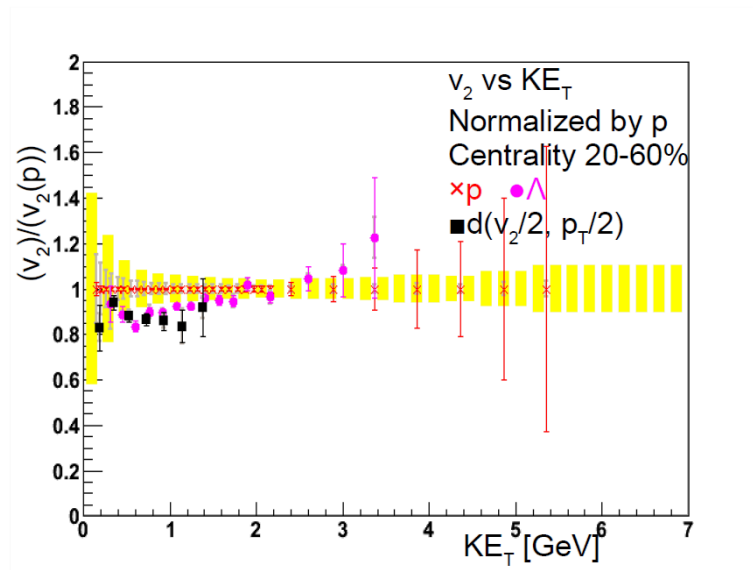


Figure 5.31: Ratio of  $v_2/n_a$  of baryons to that of  $(anti-)p$  as a function of  $KE_T/n_a$  at centrality  $20 - 60\%$ .

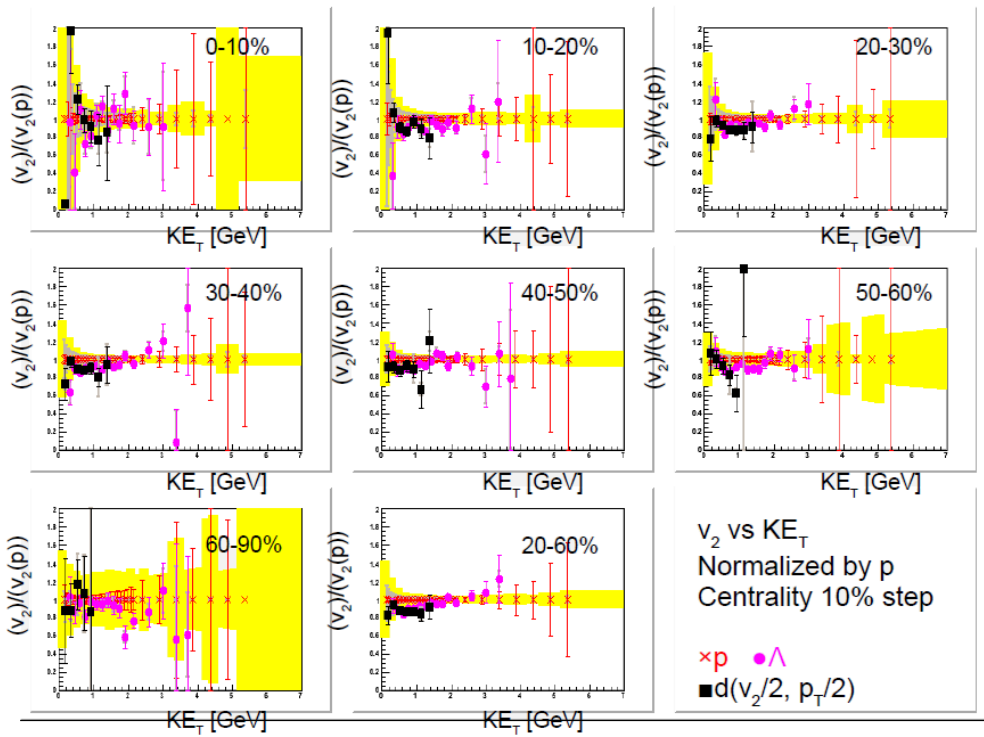


Figure 5.32: Ratio of  $v_2/n_a$  of baryons to that of  $(anti-)p$  as a function of  $KE_T/n_a$  for each centrality range.

### 5.4.3 $\pi$ , K and $\phi$ mesons

Figure 5.33 - 5.36 show the  $v_2$  of the mesons. They have different masses and the same quark number.  $K$  has smaller  $v_2$  than  $\pi$  and  $\phi$  has smaller  $v_2$  than  $K$  at  $p_T < 2 \text{ GeV}/c$ . Figure 5.37 - 5.40 show  $KE_T$  scaling. The  $v_2$  of mesons are consistent with  $KE_T$  scaling. It should be noted that  $\phi$  that has a small cross section of hadron scattering is consistent with other mesons. It means they have a smaller effect of hadron scattering. The mean value of relative magnitude of the  $v_2$  of  $\phi$  over  $\pi$  is  $0.95 \pm 0.02$ .

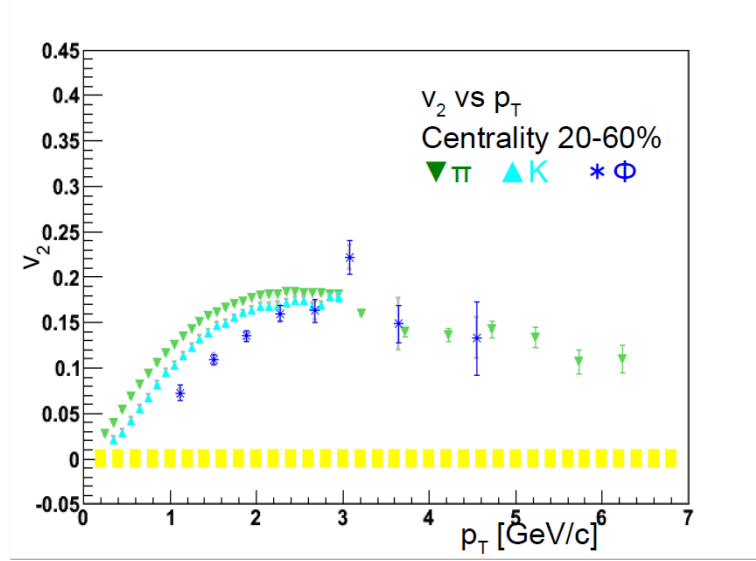


Figure 5.33:  $v_2$  as a function of  $p_T$  of mesons at centrality  $20 - 60\%$ .

## 5.5 Charm study

The  $v_2$  of a heavy quark may be decreased than light quarks because the heavy parton might not participate in the same collective expansion because of its heavy mass, if the heavy quarks do not undergo the sufficient interactions with light quarks. The  $v_2$  of heavy flavor electron that comes from  $D$  or  $B$  meson decay is measured. The results are shown in Fig.5.41 [34]. It agrees with the theoretical calculation that assumes charm  $v_2$  is same as light quarks.  $J/\Psi$   $v_2$  has also been studied. There are two possible formation processes of  $J/\Psi$ . A charm pair of  $J/\Psi$  may be formed in an early stage of collision by hard-scattering. It is called “direct  $J/\Psi$ ”. Or charm quark may pass through the partonic flow with other light quarks and recombined during phase transition. It is called “recombined  $J/\Psi$ ”. The direct  $J/\Psi$  is expected to have no (zero)  $v_2$  (if no suppression, or suppression does not depend on geometry) and the recombined  $J/\Psi$  would inherit the  $v_2$  from the charm quarks. The  $v_2$  of  $J/\Psi$  provides a key to elucidate the charm generation process. The analysis has been carried out the reaction plane from RxP in PHENIX-Run7 data analysis. Due to a limited statistics for the  $J/\Psi$   $v_2$  measurement, no significant result is obtained in order to distinguish these two different scenarios as shown in Fig.5.42 [35].

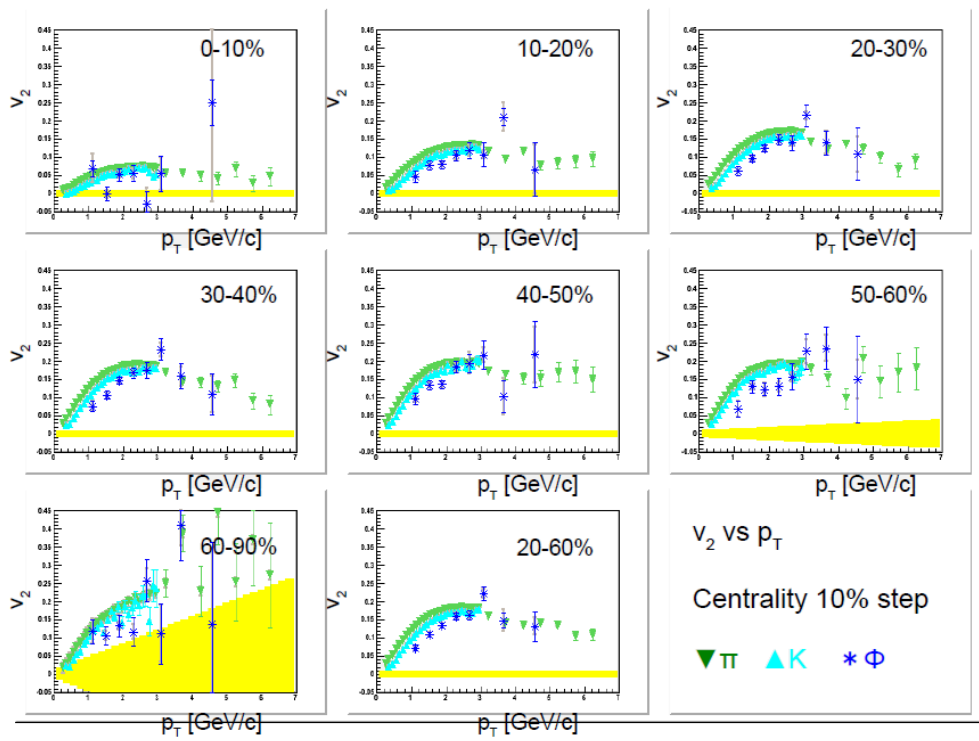


Figure 5.34:  $v_2$  as a function of  $p_T$  of mesons for each centrality ranges.

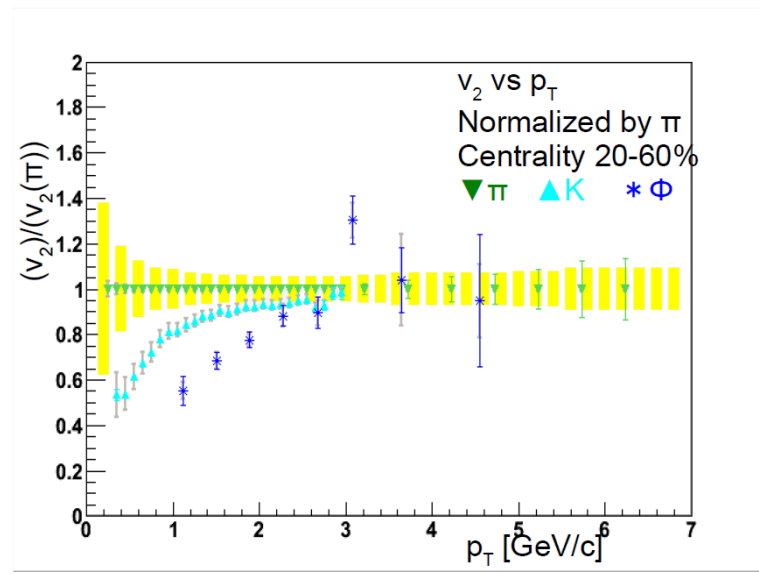


Figure 5.35: Ratio of  $v_2$  of mesons to that of  $\pi$  as  $p_T$  at centrality 20 – 60%.

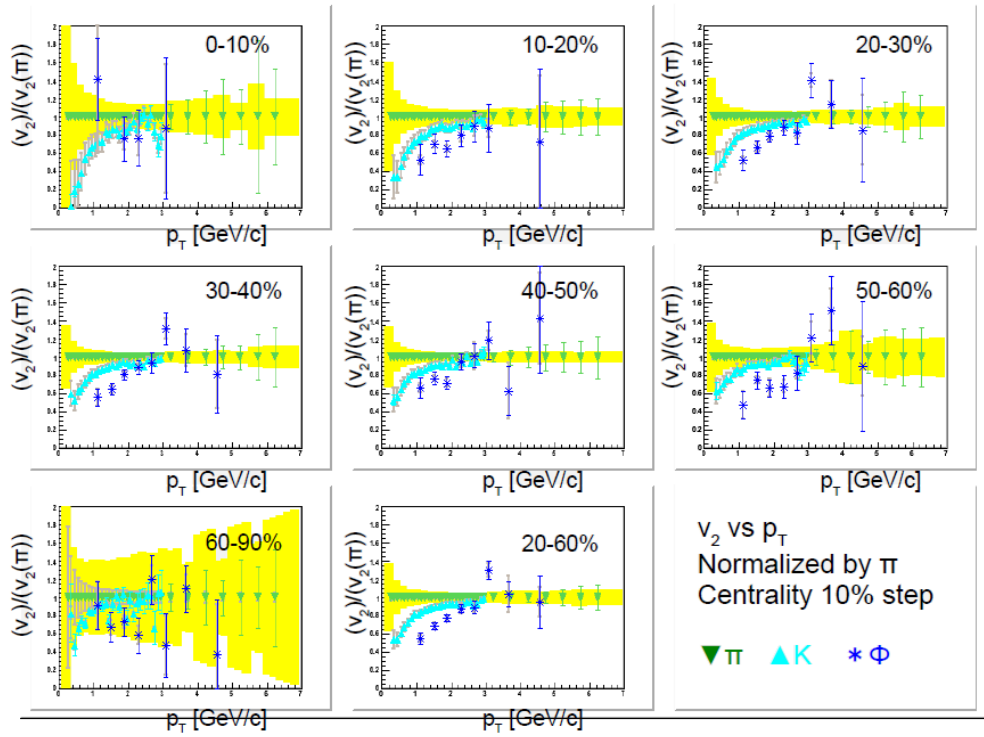


Figure 5.36: Ratio of  $v_2$  of mesons to that of  $\pi$  as  $p_T$  for each centrality ranges.

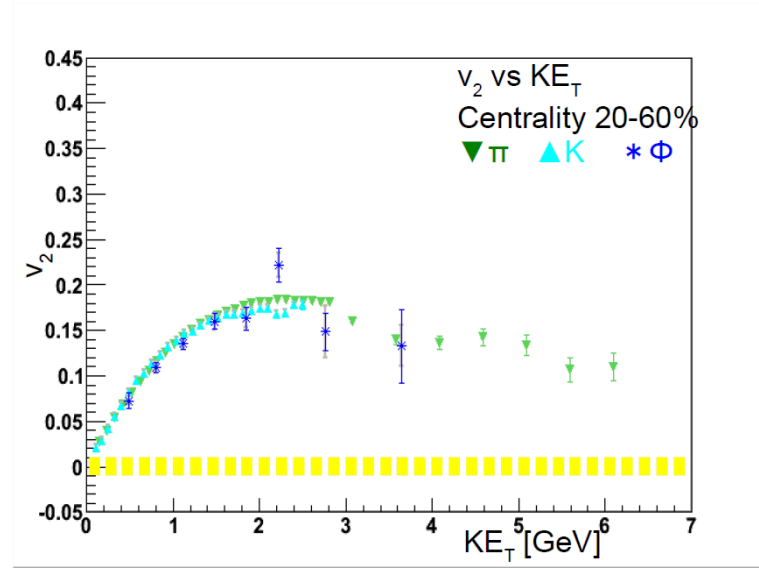


Figure 5.37:  $v_2$  as a function of  $KE_T$  of mesons at centrality 20 – 60%.

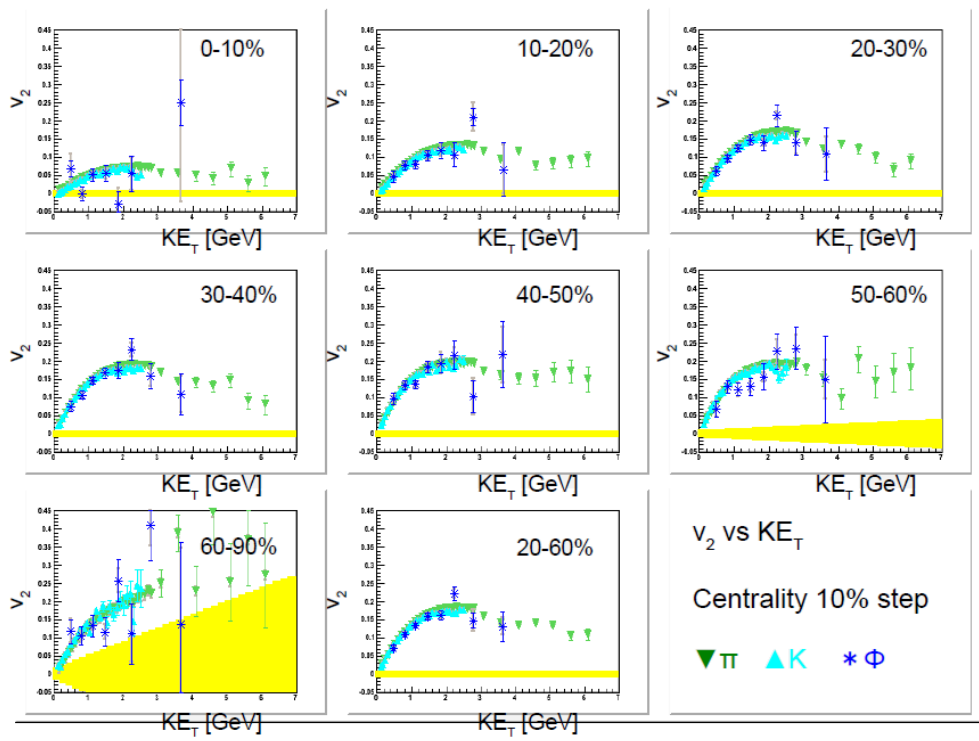


Figure 5.38:  $v_2$  as a function of  $KE_T$  of mesons for each centrality ranges.

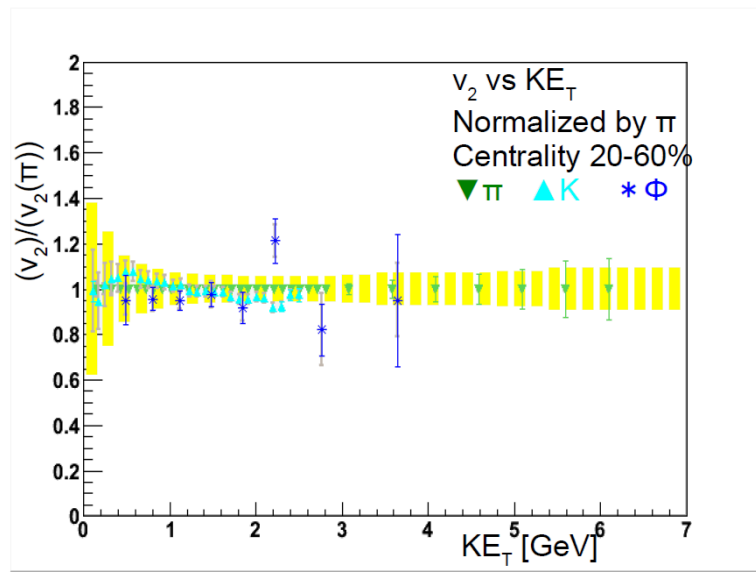


Figure 5.39: Ratio of  $v_2$  of mesons to that of  $\pi$  as a function of  $KE_T$  at centrality 20 – 60%.

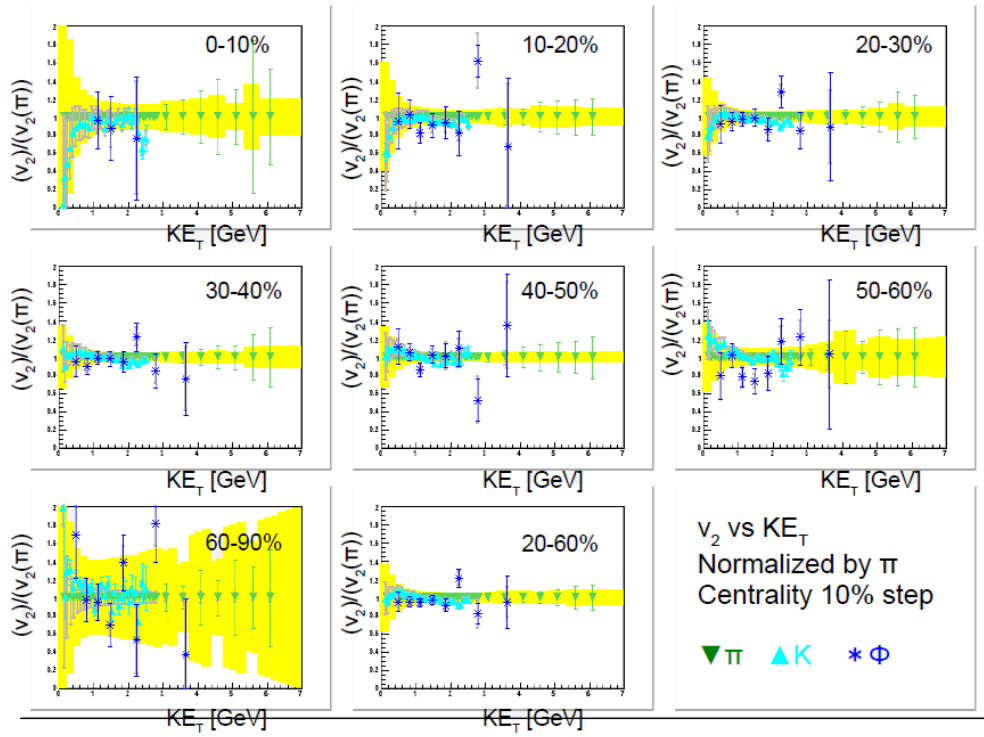


Figure 5.40: Ratio of  $v_2$  of mesons to that of  $\pi$  as a function of  $KE_T$  for each centrality range.

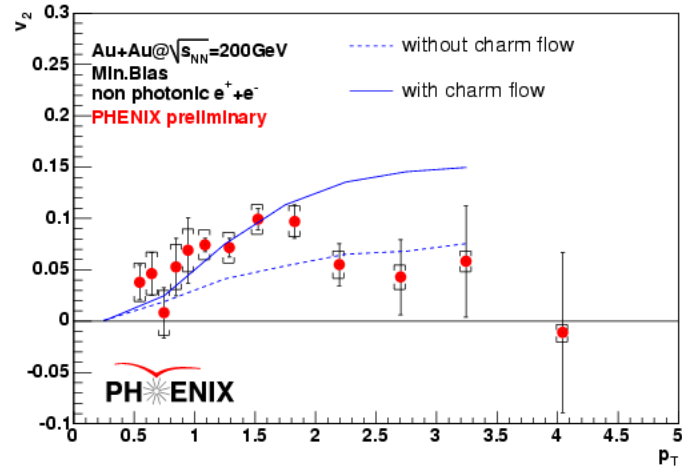


Figure 5.41: Non-photonic electron  $v_2$  with quark coalescence model calculation[34].

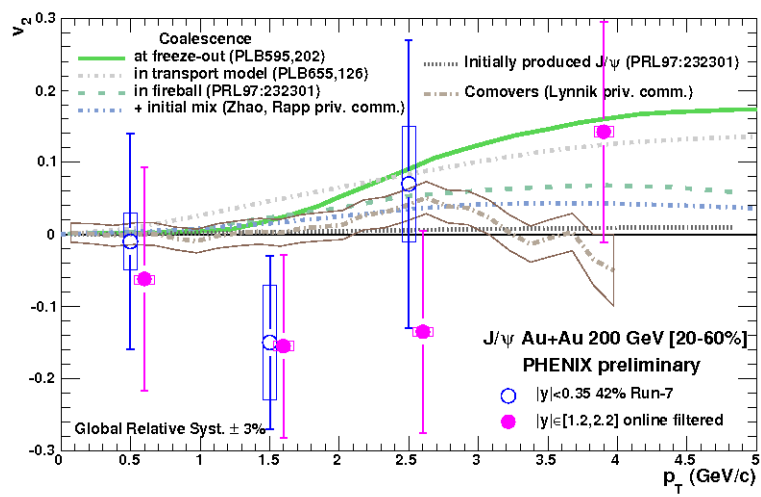


Figure 5.42:  $v_2$  of  $J/\psi$  as a function of  $p_T$  at mid and forward rapidities with theoretical expectation at mid-rapidity[35].

## 5.6 Interaction between hard and soft

The  $v_2$  is measured as amplitude of event anisotropy in particle distribution with respect to the event plane. It is expected that the collective flow (elliptic expansion) is given by the pressure gradient for the large the  $v_2$  at low momentum. The good consistency between results of RHIC and hydrodynamic model calculation indicates that the  $v_2$  is indeed caused by flow effect in the low momentum range ( $p_T < 2$  GeV/c). The dependence of the  $v_2$  as a function of parton number as well as a good consistency among different particles with quark number scaling would suggest the quark level collectivity (flow) and quark coalescence for the hadron formation at the mid momentum range ( $p_T < 1 - 3$  GeV/c).

Conversely, the particle mass or the quark number dependence of  $v_2$  seems to be failed at high momentum ( $p_T > 3$  GeV/c). This may be an evidence that  $v_2$  is dominated by the hard processes which is given by the jet quenching coming from the partonic energy loss at high momentum range. It could be given by the path length depending on the emission direction from the reaction plane (minor axis of the oval) of the matter. We know hadronization about the jet that is an elementary process which emits hadrons in a direction of small cone as well as back-to-back cones in the high energy parton interactions. The hard  $v_2$  that caused by interaction between high energy particles and hot dense matter may not depend on the number of constituent quarks of the particle unlike the soft  $v_2$ .

The soft  $v_2$  may be affected by hard particles if the hard  $v_2$  is the result of interaction between them. It is difficult to select hard events in heavy ion collision although the jet hadronization is observed in  $pp \sqrt{s_{NN}} = 200$  GeV collision at RHIC. We here define an event with high momentum particle as jet-like event and an event without high momentum particle as un-jet-like event at PHENIX central arm acceptance. Then, jet-like event and un-jet-like event are separated by the momentum of triggered particle. The centrality and the reaction plane distribution are biased by the trigger particle at high momentum. 40 - 50 % of centrality events are chosen for this analysis to minimize the centrality bias effect because  $v_2$  is flat within error in the centrality range. The biased reaction plane is re-flattened to measure  $v_2$ . Figure 5.45 shows the  $v_2$  of selected events by the value of trigger  $p_T$  which is the highest  $p_T$  of the event.  $v_2$  of events with  $p_T^{trig} > 1.2$  GeV/c (jet-like) is same to the inclusive  $v_2$ .  $v_2$  of events with  $p_T^{trig} < 1.2$  GeV/c (un-jet-like) is lower than the inclusive  $v_2$  at the low  $p_T$  range. This result suggests inclusive  $v_2$  is affected by the trigger selection at low  $p_T$  and pure flow  $v_2$  may be lower than that. It is difficult to measure the value of bias of soft  $v_2$  by jet because the trigger quality is not so good because PHENIX has only half of  $2\pi$  of acceptance of  $\phi$ -angle.

The jet-like event may be selected by maximum momentum (the highest momentum of the event) trigger. It is assumed that the event which has a high momentum track is jet-like. But, the event plane distribution of the selected events are not flat because of the limited azimuthal acceptance of the PHENIX central arm. An in-plane direction of the event plane is leaned to the acceptance direction when the events have a high momentum particle. An out of plane direction of the event plane is leaned to the acceptance direction when the events have no high momentum particle. The event plane must be a flat distribution to measure the  $v_2$ . Then, it is re-flattened by weighting method or flattening method. Figure 5.43 and 5.44 shows the re-flattening. The measured reaction plane distribution is normalized by the inverse weight of the distribution itself in the weighting method. It is also flattened by the usual higher order Fourier flattening methods as described previously.

The experimental results of  $v_2$  of (un-)jet like event are compared with a calculation result with

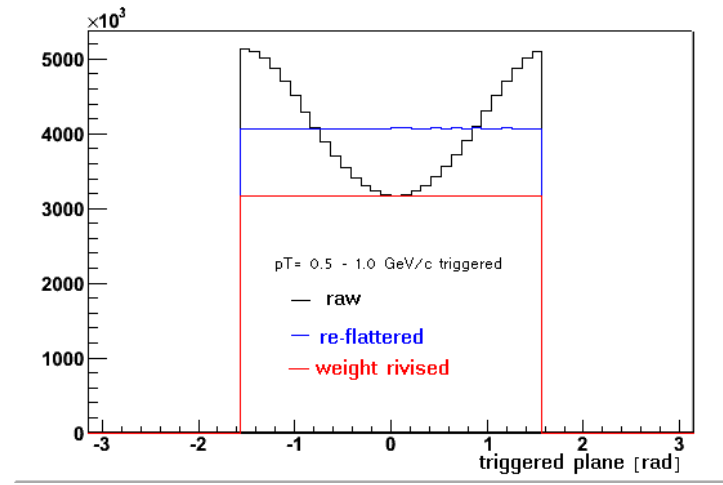


Figure 5.43: Event plane distribution of events that have trigger of  $p_T = 0.5 - 1.0$  GeV/c at centrality 0 – 50%. Black shows before revision. Red shows weighting method revision. Blue shows flattening method revision.

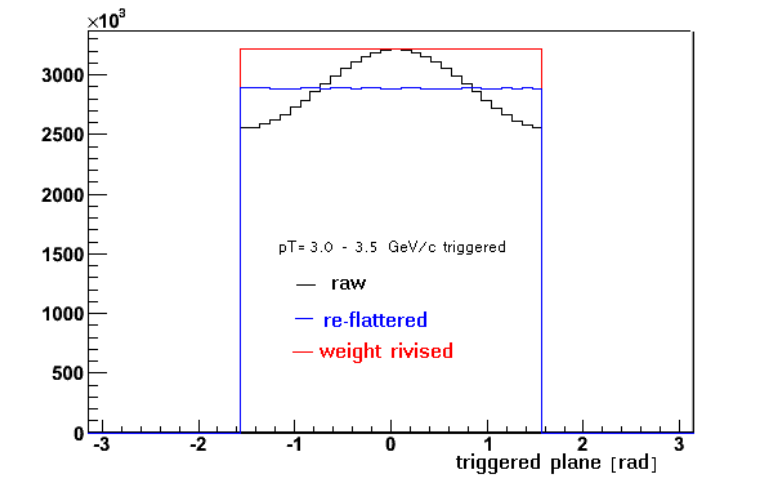


Figure 5.44: Event plane distribution of events that have trigger of  $p_T = 3.0 - 3.5$  GeV/c at centrality 0 – 50%. Black shows before revision. Red shows weighting method revision. Blue shows flattening method revision.

“A Multi-Phase Transport Model (AMPT)”. AMPT model is constructed to describe the heavy ion collisions at center-of-mass energies from about  $\sqrt{s_{NN}} = 5$  to 5500 GeV with the following various components. The hard mini-jet partons and soft strings of the initial condition are given by heavy ion jet interaction generator (HIJING) model. Scatterings of partons are given by Zhang parton Cascade (ZPC) model. Hadronization process is based on the Lund string fragmentation model and by a quark coalescence model. Scattering of hadrons are given by a relativistic transport (ART) model. It is known that the AMPT model has been able to reasonably describe many of the experimental observations at RHIC[36].

Figure 5.46 shows the comparison of  $v_2$  of PHENIX and AMPT at centrality 20 – 60%. Figure 5.47 show the jet biased  $v_2$  of AMPT at  $|\eta| < 0.35$  at centrality 40 – 50%. In the middle panel, particles that go through into limited  $\phi$ -angle acceptance to reproduce PHENIX experiment. The high momentum trigger is selected with the same acceptance to PHENIX central arm detectors ( $|\eta| < 0.35$ ,  $\phi \sim \pi$ ). The biased reaction plane by the trigger is re-flattened as same as PHENIX experimental data analysis. In the right panel, the trigger is selected in the full azimuthal angle acceptance. The reaction plane does not need to be re-flattened since it has no bias. A similar tendency is seen in both middle and right panels compared with the experimental measurement shown in the left panel. Un-jet-like  $v_2$  with the trigger particle selection lower than about  $p_T = 1.2$  GeV/c is smaller than inclusive  $v_2$  for all panels in Fig.5.47. The  $v_2$  reduction is observed for un-jet-like event, which is not at least given by the systematic bias of re-flattening process.

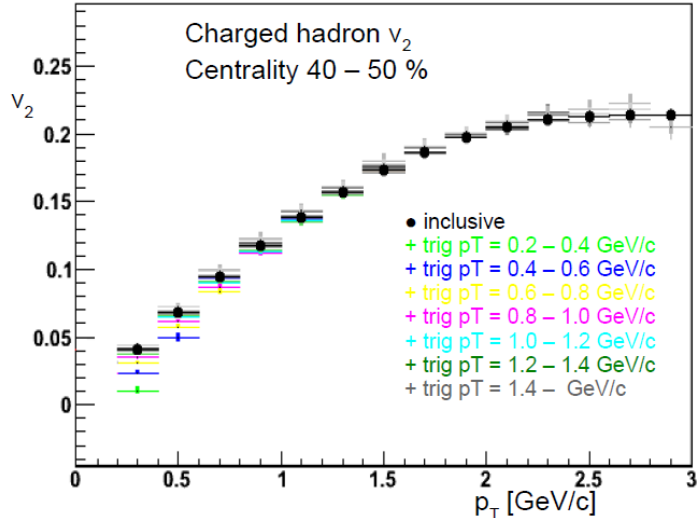


Figure 5.45: Charged hadron  $v_2$  as a function of  $p_T$ . Black points show inclusive  $v_2$  and colored points show selected event by each maximum momentum trigger.

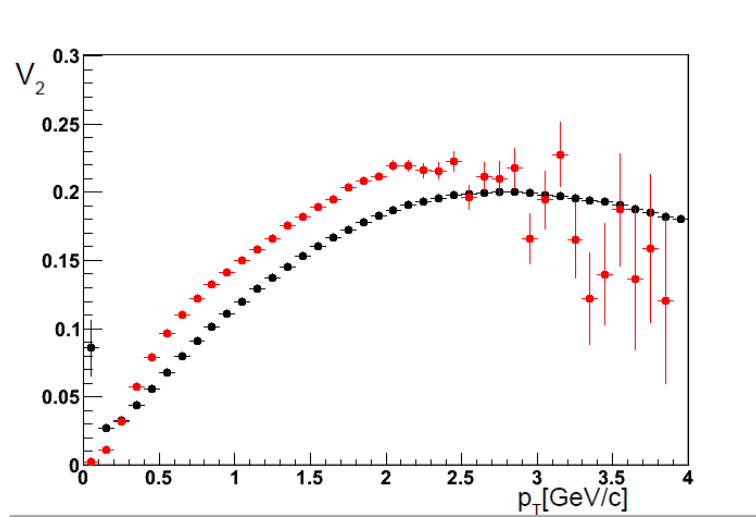


Figure 5.46: Charged hadron  $v_2$  as a function of  $p_T$ . Black points show result of PHENIX. Red points show result of AMPT

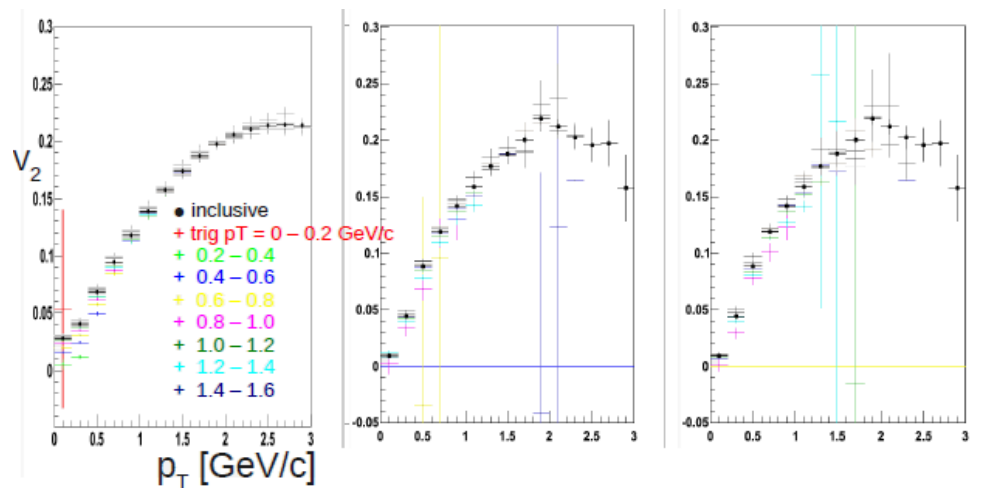


Figure 5.47: Charged hadron  $v_2$  as a function of  $p_T$ . Black points show inclusive  $v_2$  and colored points show selected event by each maximum momentum trigger. Left shows PHENIX. The center shows AMPT with PHENIX acceptance. Right shows AMPT ( $\phi = 2\pi$  acceptance)

## 5.7 consistency between particles and anti-particles

$\pi$ ,  $K$ ,  $p$ ,  $d$  and  $\Lambda$  have anti-particle that consists of anti-partons and have inverse charge except neutral  $\Lambda$ .  $\Lambda$  consists of u, d, and s quark and decay to  $p$  and  $\pi^-$ .  $\bar{\Lambda}$  consists of  $\bar{u}\bar{d}\bar{s}$  and decay to  $\bar{p}$  and  $\pi^+$ . The  $v_2$  of particles and anti-particles are consistent with each other if quark level collectivity (flow) is generated. Figure 5.48 - 5.67 show the comparison between particles and anti-particles. Red points show the  $v_2$  of the particles and blue points show the  $v_2$  of the anti-particles. The Yellow band shows the systematic error of reaction plane determination. Yellow error may be ignored when comparing between the particles and the anti-particles because the particles have the same systematic uncertainty with the anti-particles in terms of the reaction plane. They are almost consistent within error even without the systematic error from the reaction plane.

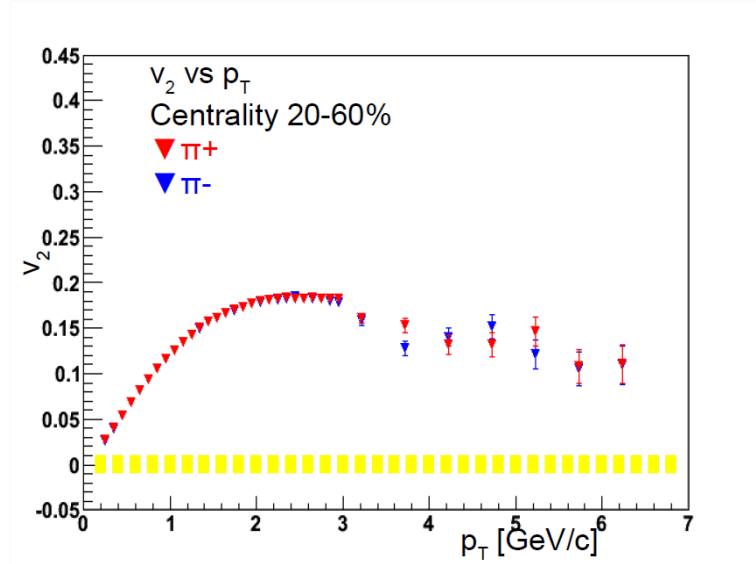


Figure 5.48:  $v_2$  as a function of  $p_T$  of  $\pi^+$  (Red) and  $\pi^-$  (Blue) at centrality 20 – 60%.

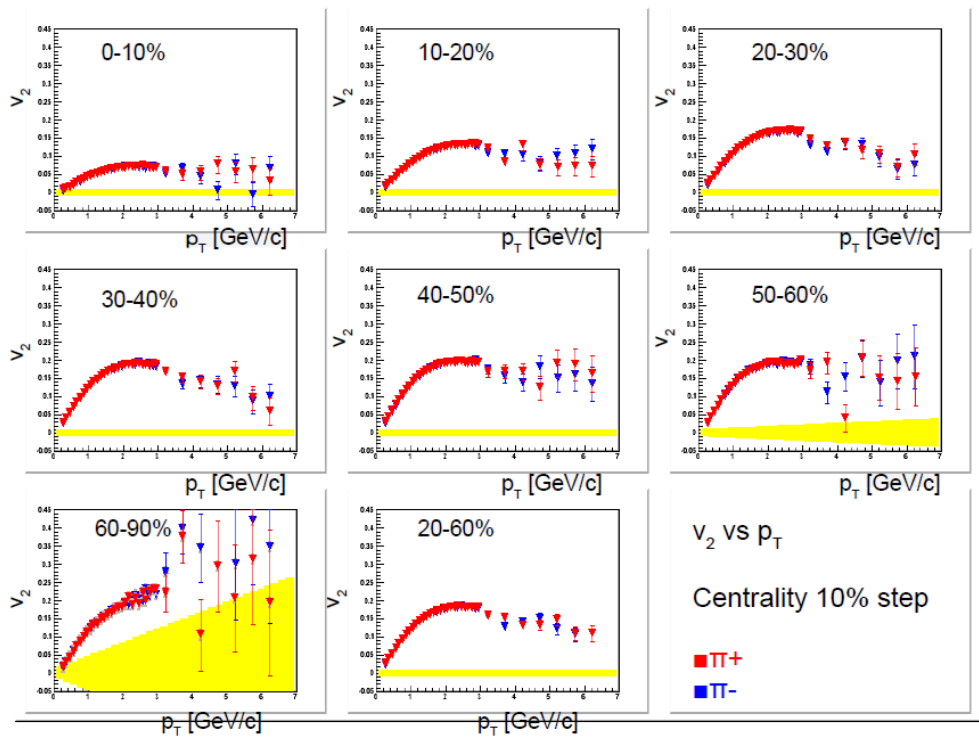


Figure 5.49:  $v_2$  as a function of  $p_T$  of  $\pi^+$  (Red) and  $\pi^-$  (Blue) for each centrality range.

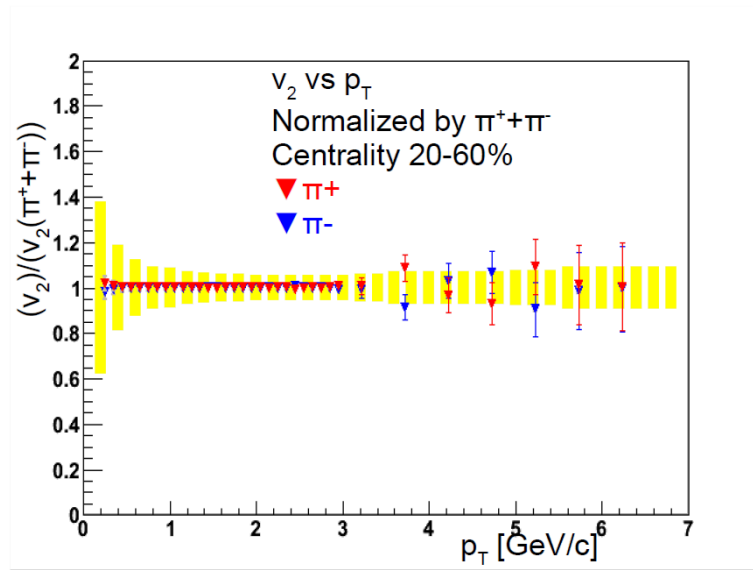


Figure 5.50: Ratio of  $v_2$  as a function of  $p_T$  of  $\pi^+/\pi$  (Red) and  $\pi^-/\pi$  (Blue) at centrality 20 – 60%.

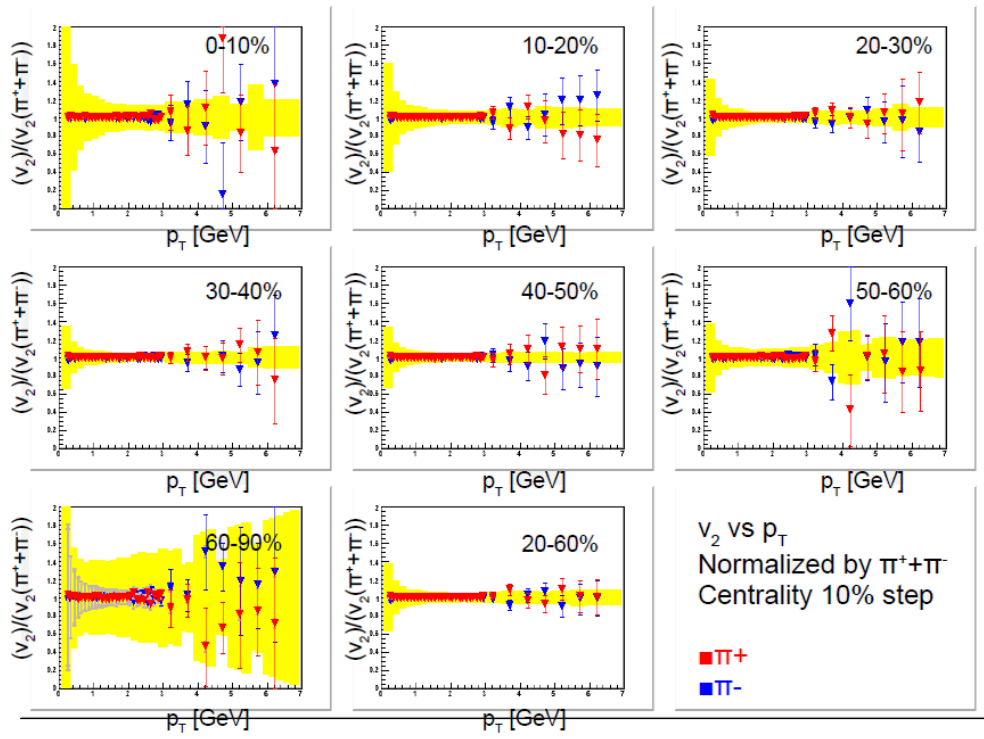


Figure 5.51: Ratio of  $v_2$  as a function of  $p_T$  of  $\pi^+/\pi$  (Red) and  $\pi^-/\pi$  (Blue) for each centrality range.

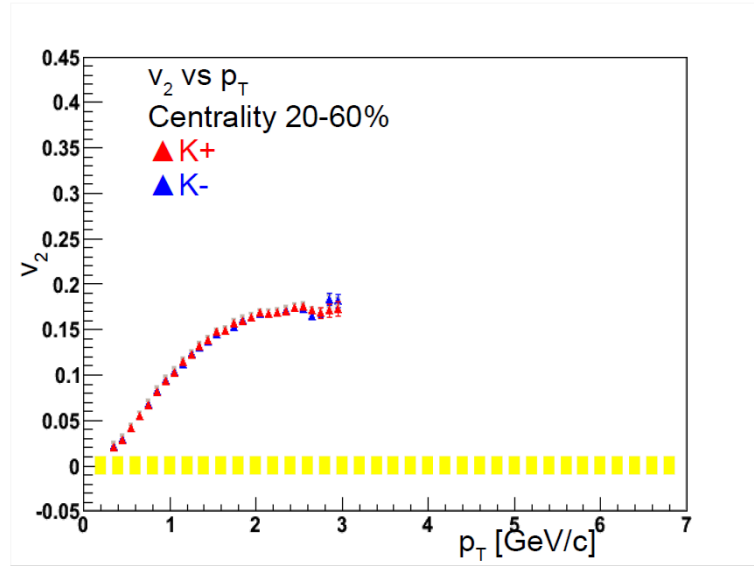


Figure 5.52:  $v_2$  as a function of  $p_T$  of  $K^+$  (Red) and  $K^-$  (Blue) at centrality 20 – 60%.

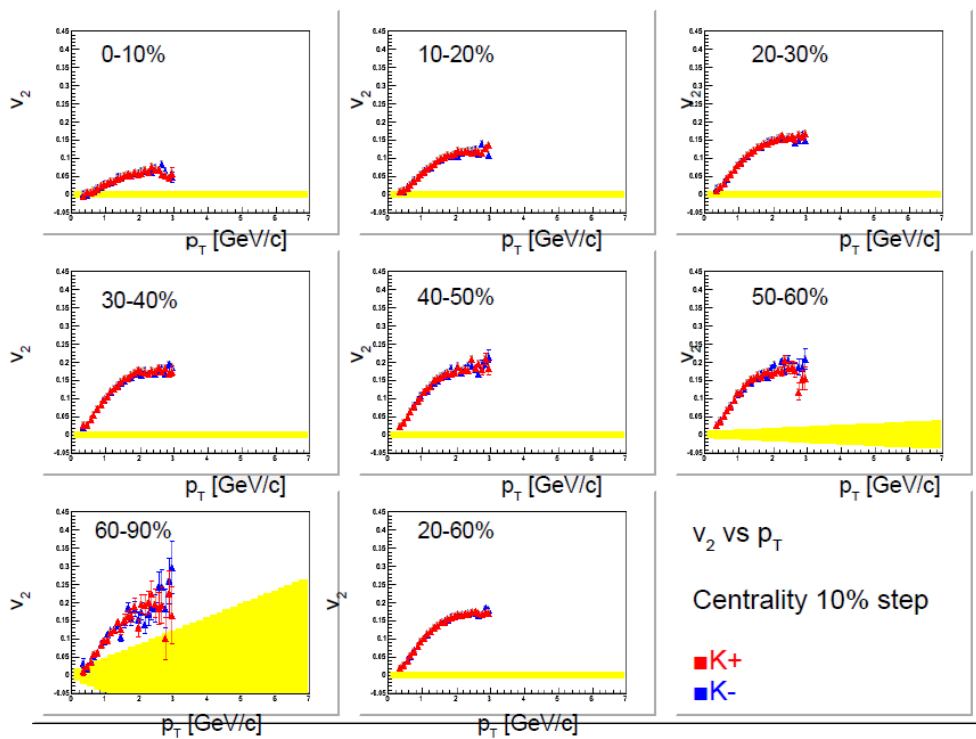


Figure 5.53:  $v_2$  as a function of  $p_T$  of  $K^+$  (Red) and  $K^-$  (Blue) for each centrality range.

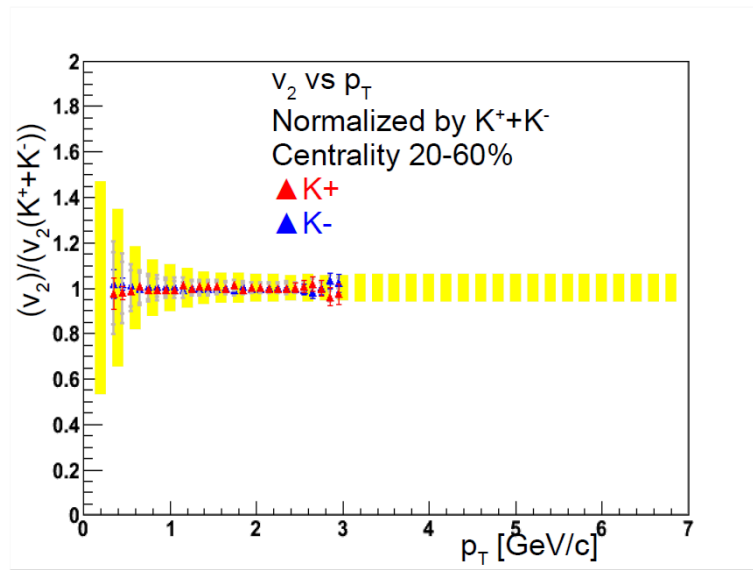


Figure 5.54: Ratio of  $v_2$  as a function of  $p_T$  of  $K^+/K$  (Red) and  $K^-/K$  (Blue) at centrality 20–60%.

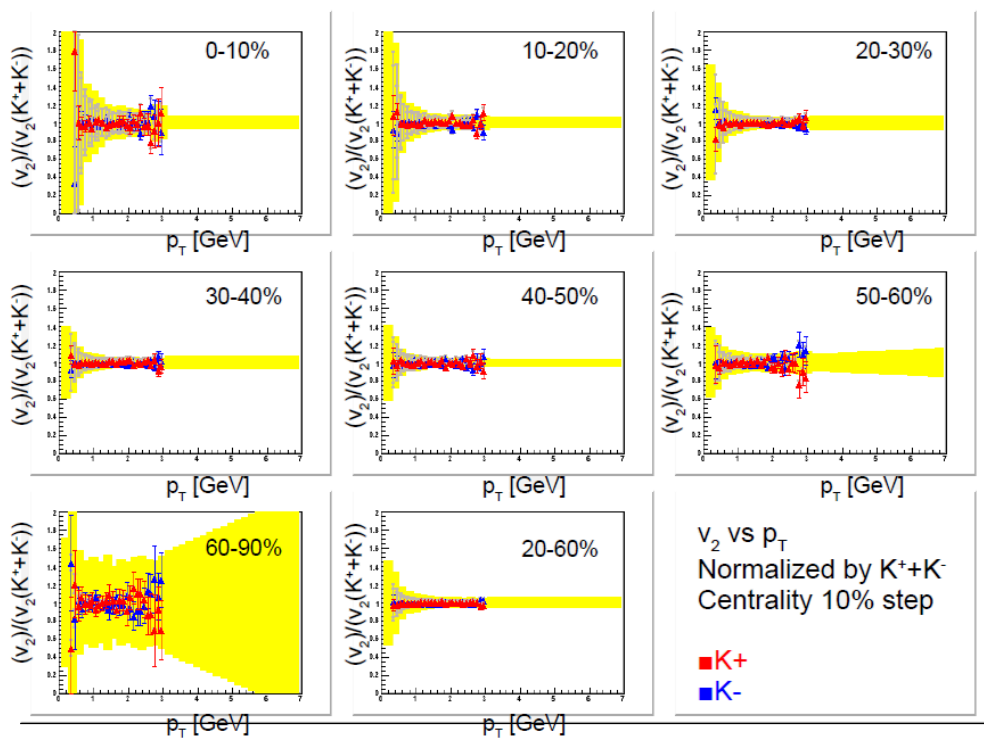


Figure 5.55: Ratio of  $v_2$  as a function of  $p_T$  of  $K^+/K$  (Red) and  $K^-/K$  (Blue) for each centrality range.

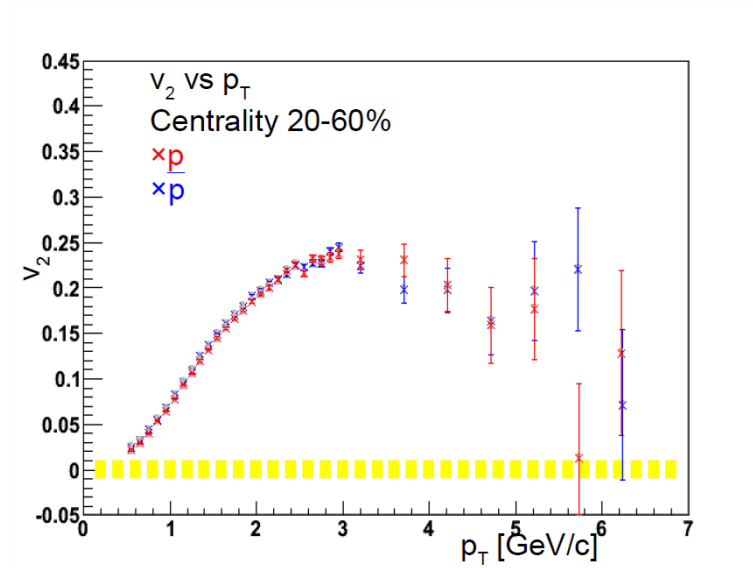


Figure 5.56:  $v_2$  as a function of  $p_T$  of  $p$  (Red) and  $\bar{p}$  (Blue) at centrality 20 – 60%.

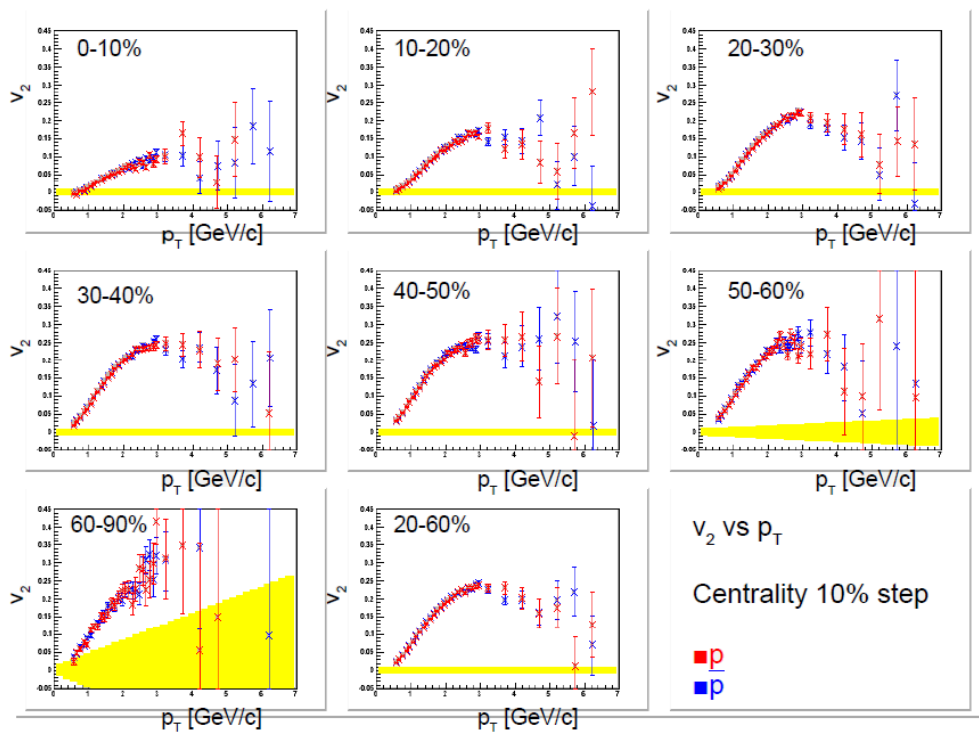


Figure 5.57:  $v_2$  as a function of  $p_T$  of  $p$  (Red) and  $\bar{p}$  (Blue) for each centrality range.

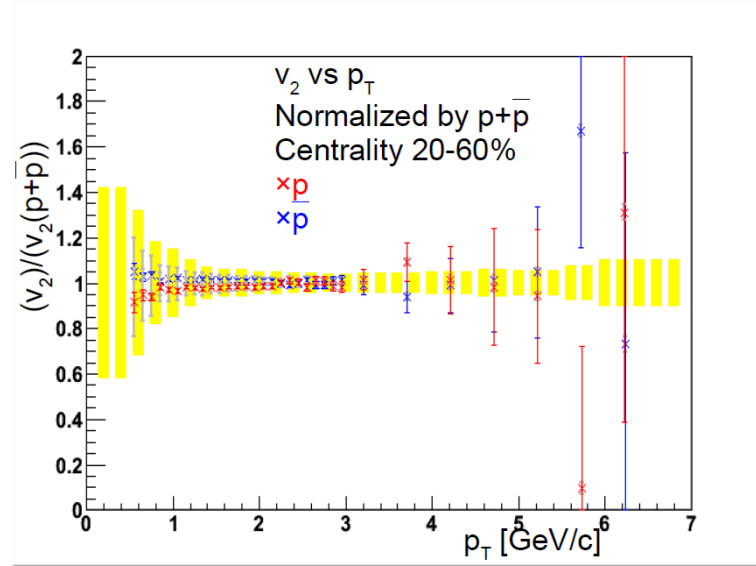


Figure 5.58: Ratio of  $v_2$  as a function of  $p_T$  of  $p/(p + \bar{p})$  (Red) and  $\bar{p}/(p + \bar{p})$  (Blue) at centrality 20 – 60%.

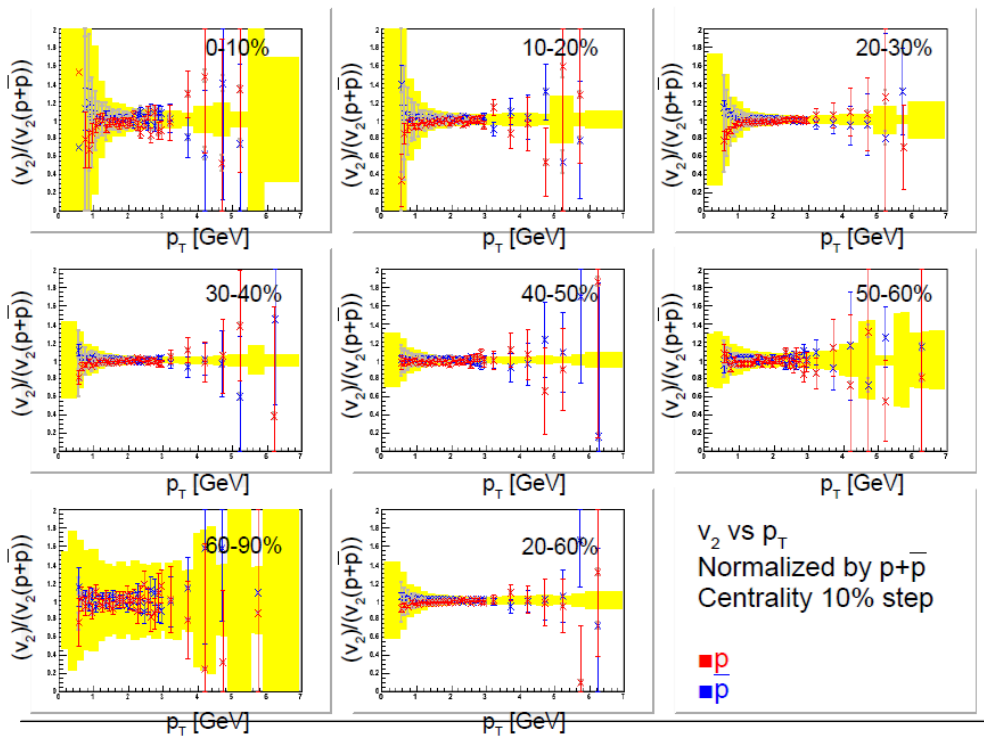


Figure 5.59: Ratio of  $v_2$  as a function of  $p_T$  of  $p/(p+\bar{p})$  (Red) and  $\bar{p}/(p+\bar{p})$  (Blue) for each centrality range.

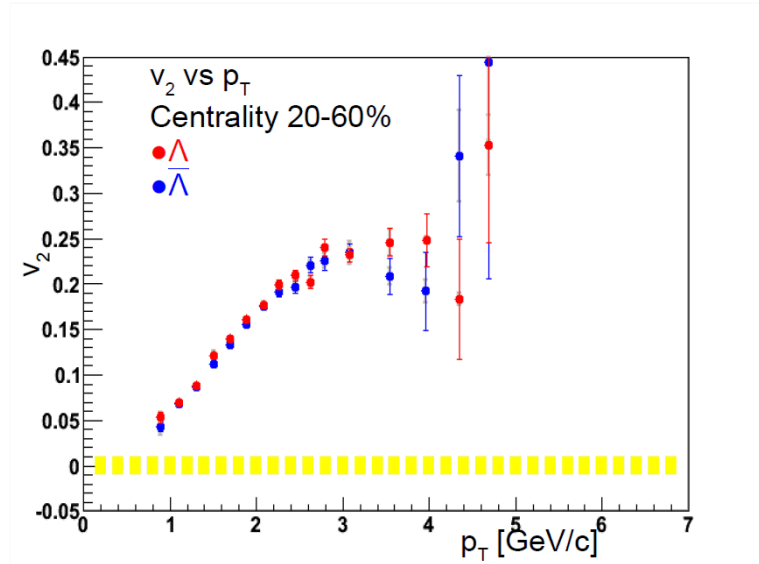


Figure 5.60:  $v_2$  as a function of  $p_T$  of  $\Lambda$  (Red) and  $\bar{\Lambda}$  (Blue) at centrality 20 – 60%.

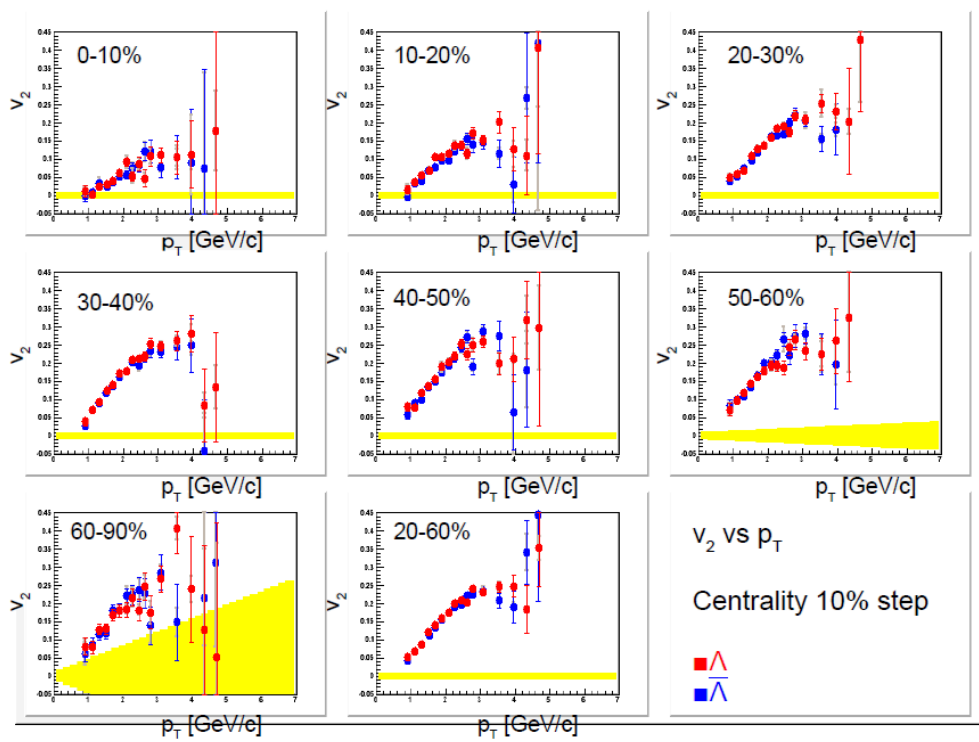


Figure 5.61:  $v_2$  as a function of  $p_T$  of  $\Lambda$  (Red) and  $\bar{\Lambda}$  (Blue) for each centrality range.

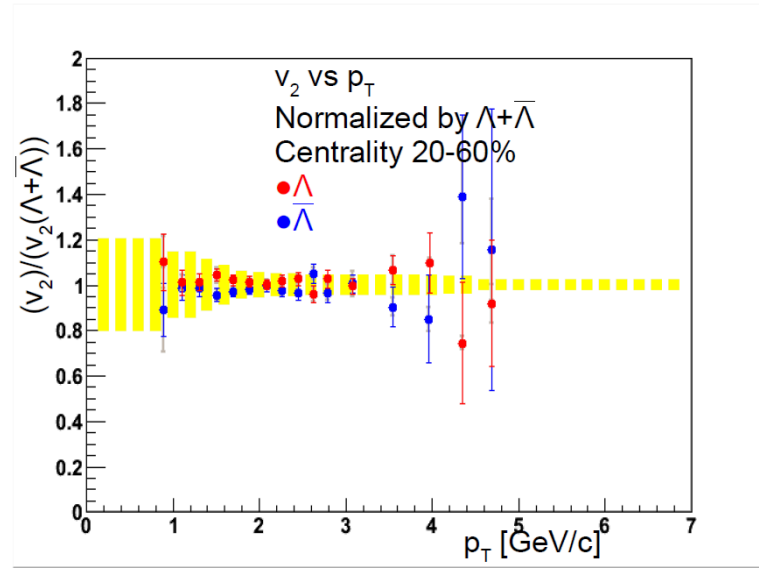


Figure 5.62: Ratio of  $v_2$  as a function of  $p_T$  of  $\Lambda/(\Lambda + \bar{\Lambda})$  (Red) and  $\bar{\Lambda}/(\Lambda + \bar{\Lambda})$  (Blue) at centrality 20 – 60%.

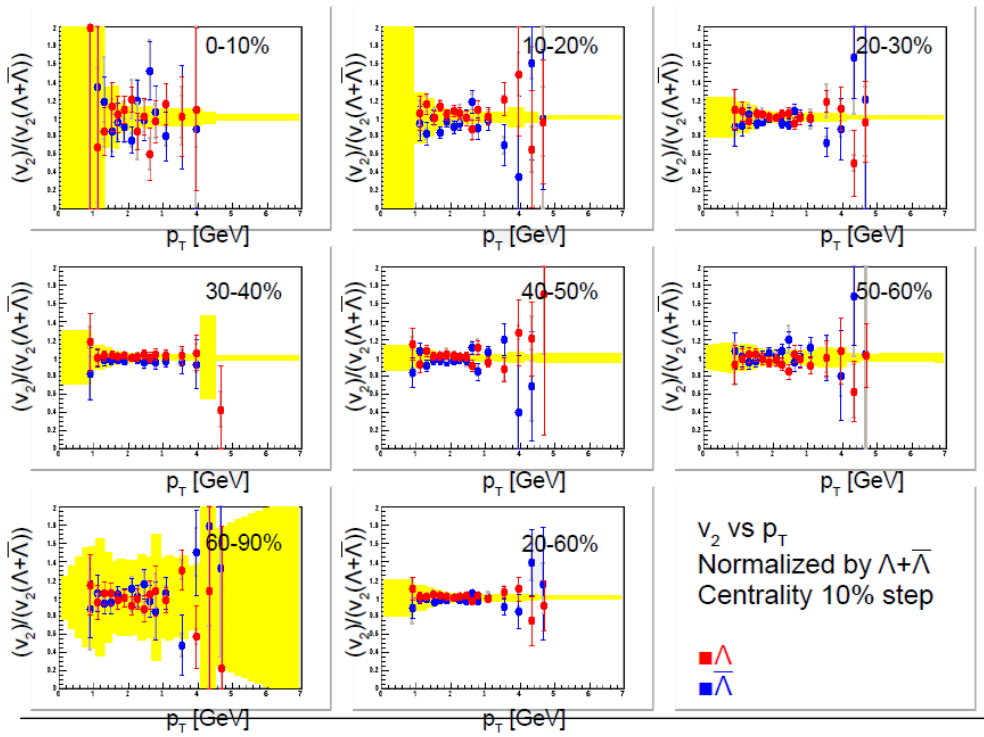


Figure 5.63: Ratio of  $v_2$  as a function of  $p_T$  of  $\Lambda/(\Lambda + \bar{\Lambda})$  (Red) and  $\bar{\Lambda}/(\Lambda + \bar{\Lambda})$  (Blue) for each centrality range.

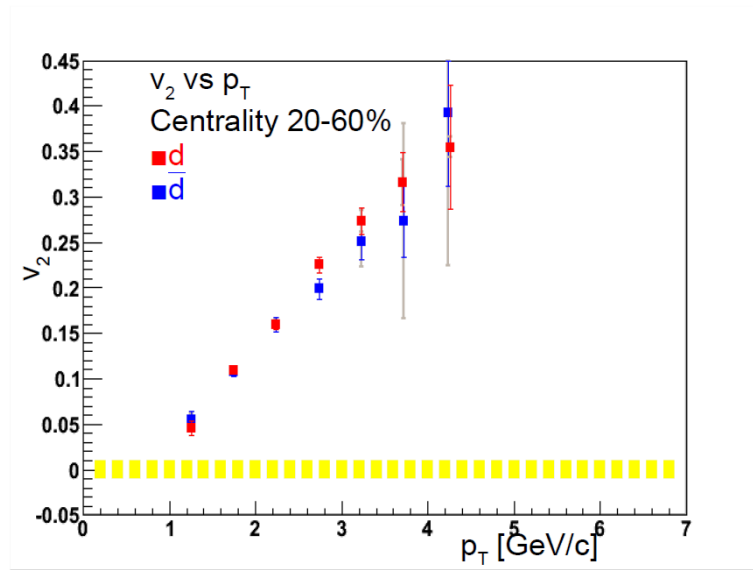


Figure 5.64:  $v_2$  as a function of  $p_T$  of  $d$  (Red) and  $\bar{d}$  (Blue) at centrality 20 – 60%.

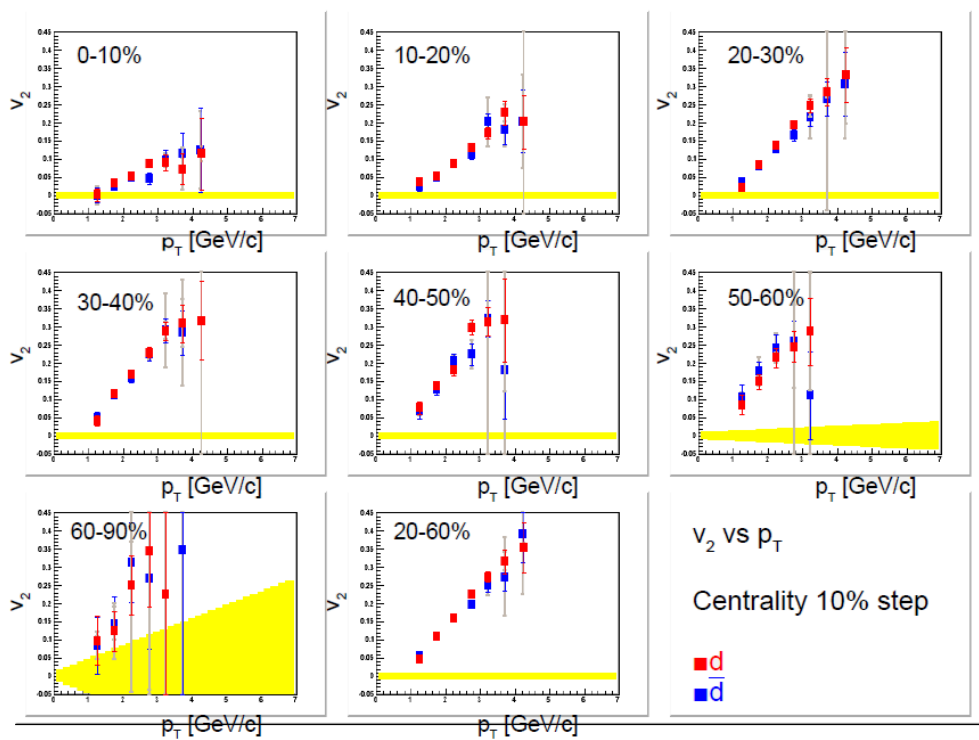


Figure 5.65:  $v_2$  as a function of  $p_T$  of  $d$  (Red) and  $\bar{d}$  (Blue) for each centrality range.

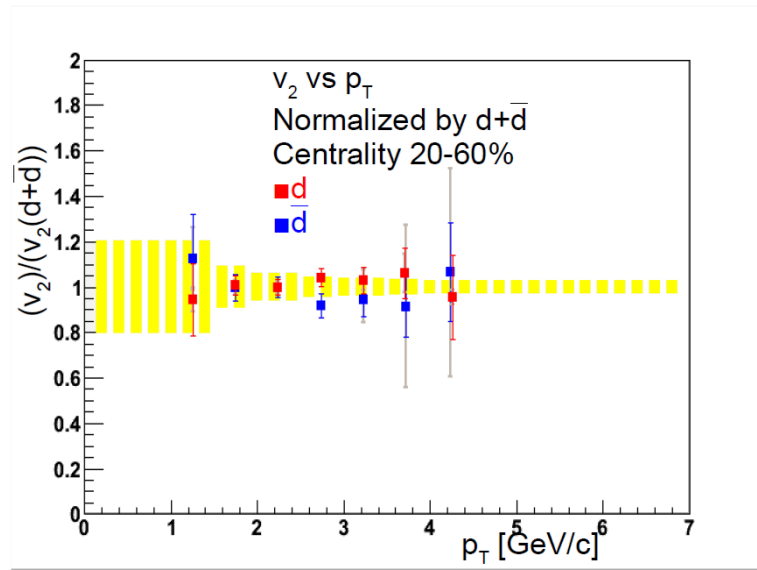


Figure 5.66: Ratio of  $v_2$  as a function of  $p_T$  of  $d/(d + \bar{d})$  (Red) and  $\bar{d}/(d + \bar{d})$  (Blue) at centrality 20 – 60%.

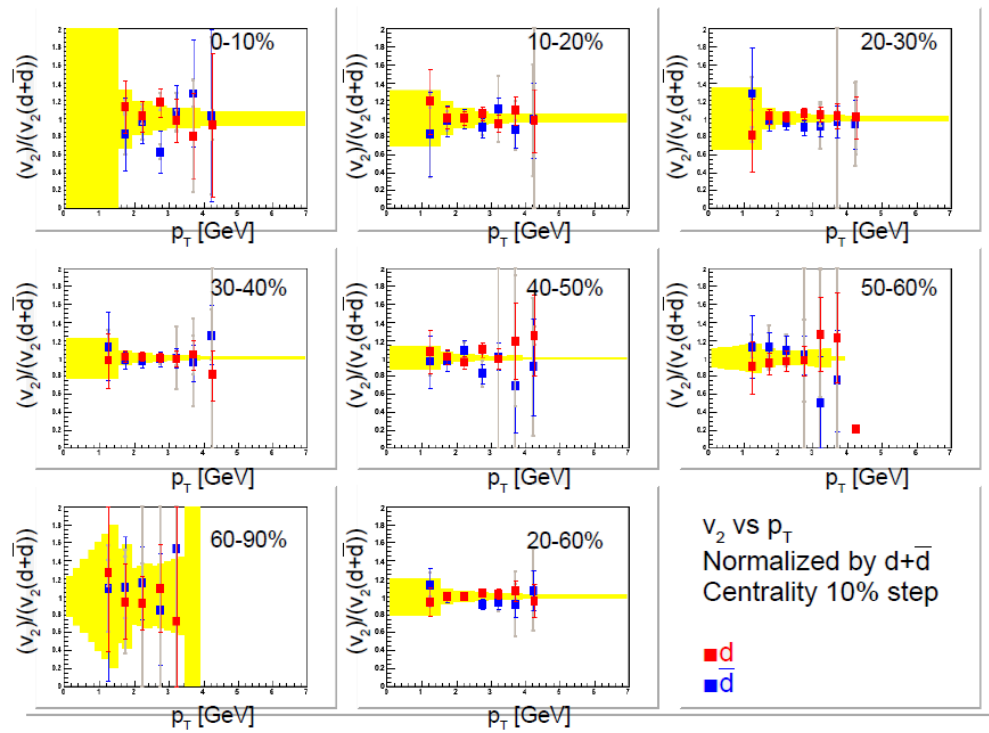


Figure 5.67: Ratio of  $v_2$  as a function of  $p_T$  of  $d/(d+\bar{d})$  (Red) and  $\bar{d}/(d+\bar{d})$  (Blue) for each centrality range.

## 5.8 Measurement of $v_2$ at Au+Au $\sqrt{s_{NN}} = 39$ and 62 GeV.

The purpose of the measurement of  $v_2$  with energy scan is to elucidate the threshold behavior of  $v_2$  in collision energy dependence with QGP phase transition. If the  $v_2$  of baryon as a function of  $p_T$  could be closer to that of meson, the number of constituent quark scaling would be broken without QGP phase. The number of 0.2 billion events of  $\sqrt{s_{NN}} = 39$  GeV Au+Au collision and 1 billion events of  $\sqrt{s_{NN}} = 62$  GeV Au+Au collision were taken at RHIC-PHENIX experiment Run10 (2010). The reaction plane resolutions for the low energy collisions are reduced because the multiplicity is smaller (as well as the  $v_2$  signal itself could be smaller) than that of Au+Au  $\sqrt{s_{NN}} = 200$  GeV collision. The influence to the flow analysis with RxP which has high resolution on the resolution is smaller than other detectors. Elliptic flow of hadrons are measured and compared with that of Run7 for  $\pi^+$ ,  $\pi^-$ ,  $K^+$ ,  $K^-$ ,  $p$ ,  $\bar{p}$  and  $d$  at minimum bias range of centrality.

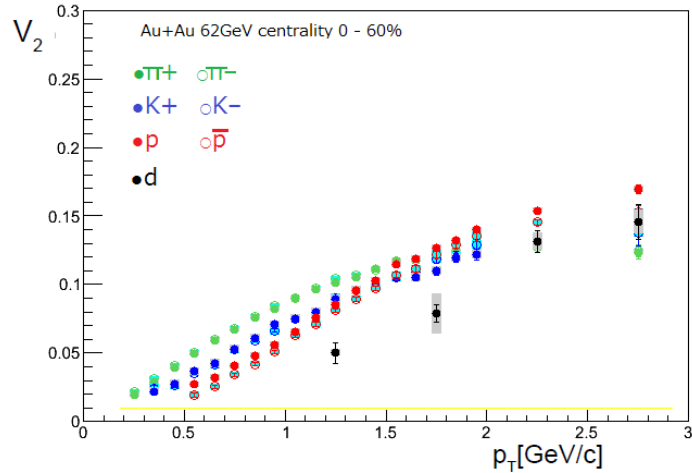


Figure 5.68:  $v_2$  as a function of  $p_T$  in  $\sqrt{s_{NN}} = 62$  GeV centrality 0 - 60% Au+Au collision.

Figure 5.68 - 5.71 show  $v_2$  and quark number scaled  $v_2$  distributions of identified particles ( $\pi^+$ ,  $\pi^-$ ,  $K^+$ ,  $K^-$ ,  $p$ ,  $\bar{p}$  and  $d$ ) in Au+Au  $\sqrt{s_{NN}} = 62$  or 39 GeV collision. They are almost consistent with quark number scaling. But the  $v_2$  of  $p$  is slightly larger than other particles. Figure 5.72, 5.73, 5.74 and 5.75 show the identified particle  $v_2$  comparison between  $\sqrt{s_{NN}} = 39$  and  $\sqrt{s_{NN}} = 200$  GeV for  $\pi$ ,  $K$ ,  $p$ ,  $\bar{p}$  and  $d$ , respectively. These  $v_2$  are almost consistent between  $\sqrt{s_{NN}} = 39$  and  $\sqrt{s_{NN}} = 200$  GeV except  $p$  and  $d$ .

The  $v_2$  of  $p$  is larger than that of  $\bar{p}$ . The  $v_2$   $\pi^+$  is slightly smaller than that of  $\pi^-$ . The  $v_2$  of  $K^+$  and  $K^-$  are consistent within measured accuracy at these energy. The difference of the  $v_2$  between  $p$  and  $\bar{p}$  increases with decreasing the collision energy. The  $v_2$  of  $d$  at  $\sqrt{s_{NN}} = 39$  GeV seems to be larger than that at  $\sqrt{s_{NN}} = 200$  GeV, too, despite the large error. The  $v_2$  difference may be the result of annihilation between  $p$  and  $\bar{p}$  because large net-proton number from baryon stopping at the low energy collisions.

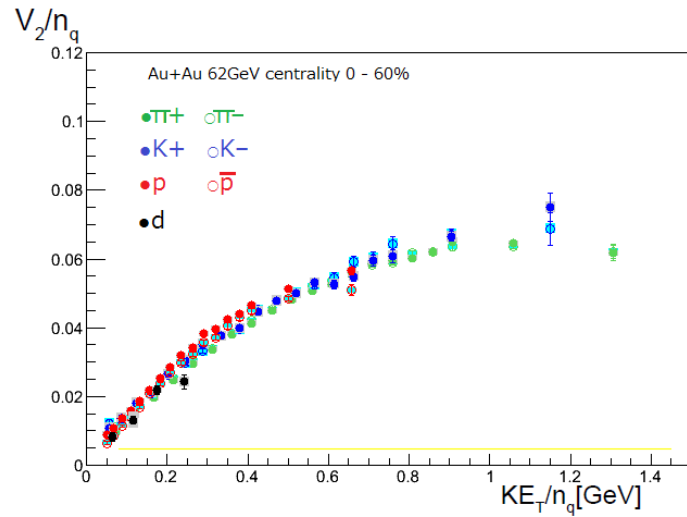


Figure 5.69:  $v_2/n_q$  as a function of  $KE_T/n_q$  in  $\sqrt{s_{NN}} = 62$  GeV centrality 0 - 60% Au+Au collision.

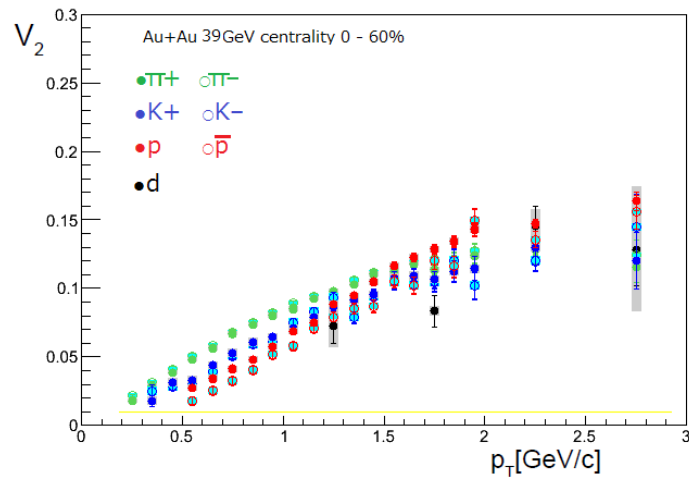


Figure 5.70:  $v_2$  as a function of  $p_T$  in  $\sqrt{s_{NN}} = 39$  GeV centrality 0 - 60% Au+Au collision.

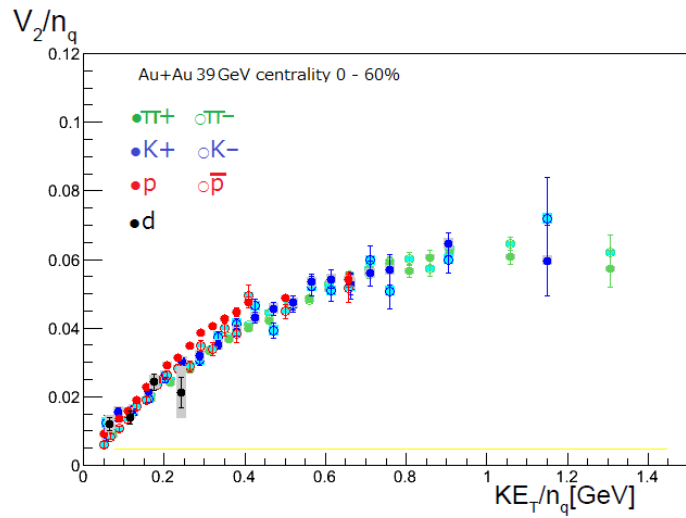


Figure 5.71:  $v_2/n_q$  as a function of  $KE_T/n_q$  in  $\sqrt{s_{NN}} = 39$  GeV centrality 0 - 60% Au+Au collision.

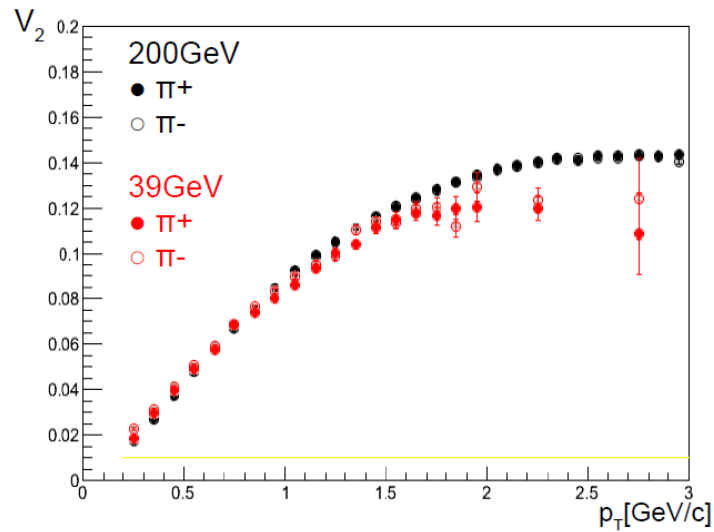


Figure 5.72:  $v_2$  as a function of  $p_T$  of  $\pi^+$  and  $\pi^-$ .

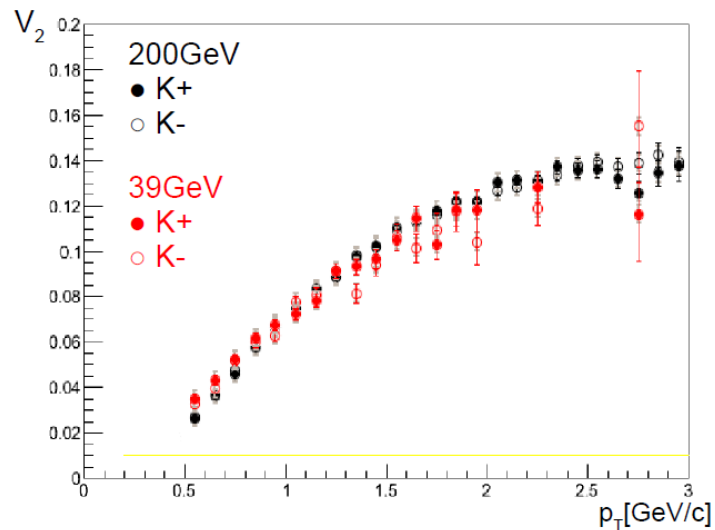


Figure 5.73:  $v_2$  as a function of  $p_T$  of  $K^+$  and  $K^-$ .

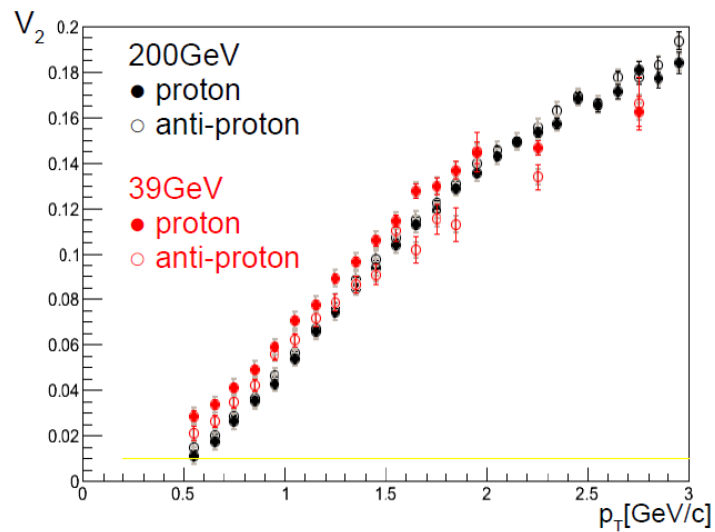
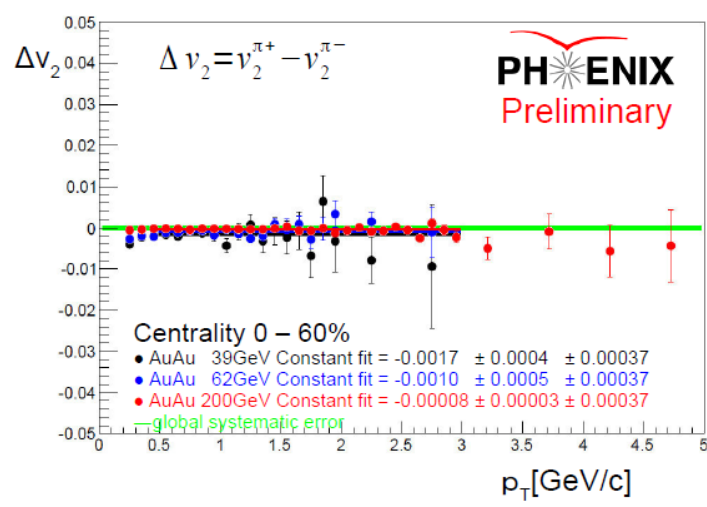
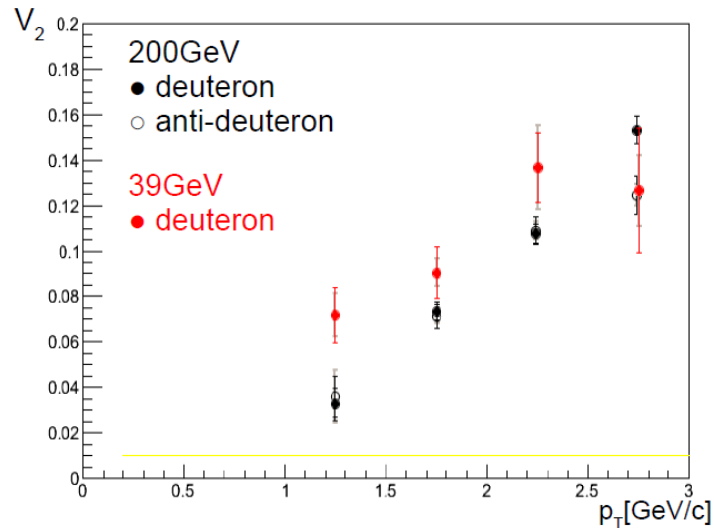


Figure 5.74:  $v_2$  as a function of  $p_T$  of  $p$  and  $\bar{p}$ .



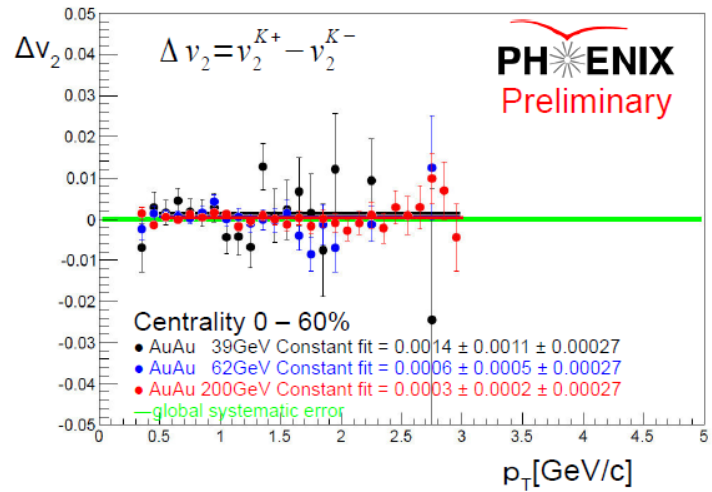


Figure 5.77: The difference  $v_2$  between  $K^+$  and  $K^-$  as a function of  $p_T$  in the three collision energy.

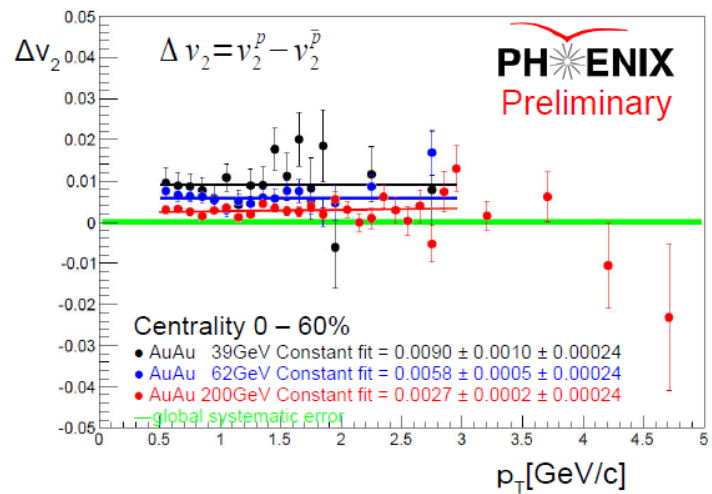


Figure 5.78: The difference  $v_2$  between  $p$  and  $\bar{p}$  as a function of  $p_T$  in the three collision energy.

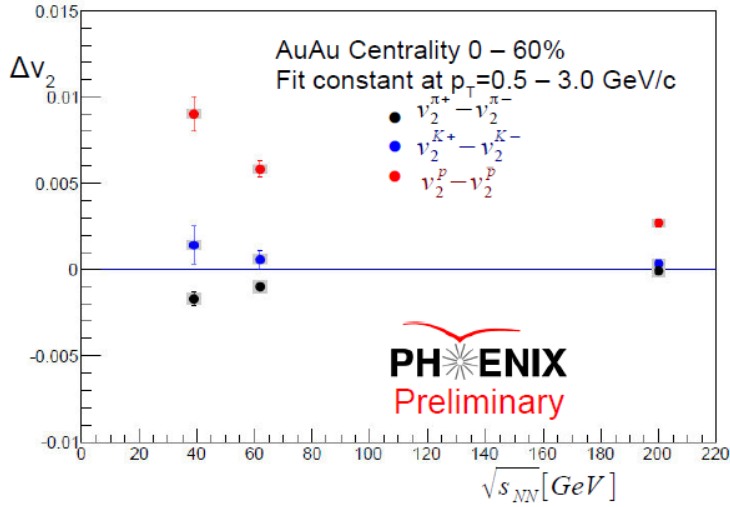


Figure 5.79: The difference  $v_2$  between positive charged hadron and negative charged hadron as a function of the collision energy.

## 5.9 Summary

The new reaction plane detector RxP worked well in  $\sqrt{s_{NN}} = 200$  GeV Au+Au collision in 2007 and in  $\sqrt{s_{NN}} = 62$  and  $39$  GeV Au+Au collision in 2010. It has been demonstrated that the design performance of maximum 0.75 of reaction plane resolution is achieved. It is two times better resolution compared to the ones before in  $\sqrt{s_{NN}} = 200$  GeV Au+Au collision.

The  $v_2$  as a function of  $p_T$  of  $\pi$ ,  $K$ ,  $p$ ,  $\bar{p}$ ,  $\Lambda$ ,  $\bar{\Lambda}$ ,  $\phi$ ,  $d$  and  $\bar{d}$  were measured in the Au+Au  $\sqrt{s_{NN}} = 200$  GeV collision. The  $v_2$  increases with  $p_T$  at low momentum range ( $p_T < 2$  GeV/c). Heavy mass particles have smaller values of  $v_2$  than the light mass particles for a given  $p_T$ . This can also be understood by shifting the rise of  $v_2$  towards higher  $p_T$  for heavier particles due to the collective expansion of the system.

The blast-wave function is extended for  $v_2$  with Glauber model which is expanded into the reaction plane direction. The estimated freeze-out eccentricity by blast-wave fitting of the  $p_T$  spectra and the  $v_2$  of the six particles has been found to be smaller than the initial eccentricity, but it still has the same orientation. The observation is consistent with the eccentricity extracted from HBT measurement. The freeze-out temperature is found to be about 150 MeV and it seems to be flat as a function of centrality.

The  $v_2$  of  $d$  is lower at  $p_T < 3$  GeV/c and higher at  $p_T > 3$  GeV/c than that of  $p$ . They are almost consistent with the nucleon number scaling within errors in all centrality ranges. But, simultaneously, the  $KE_T$  and  $n_q$  scaled  $v_2$  of  $d$  is slightly smaller than that of  $p$  in average at centrality 20–60%. The  $v_2$  of mesons are consistent at the high  $p_T$  region in which seems saturated at  $p_T > 2$  GeV/c. The  $v_2$  of baryons are higher than  $v_2$  of meson at  $p_T > 2$  GeV/c. The  $KE_T$  scaling describes the  $p_T$  shift coming from the mass effect based on hydrodynamic picture. The  $v_2$  as a function of  $KE_T$  of  $\pi$ ,  $K$  and  $\phi$  (mesons) or  $p$  and  $\Lambda$  (baryons) are consistent within mesons or baryons, separately. The  $v_2$  of  $d$  deviates from meson or baryon. All these observations conclude

that the  $v_2$  of all particles seem to be given by the centrality, the  $p_T$  and the constituent quark number of the particle. Therefore the  $v_2$  of identified particles were compared with the quark number scaling and the  $KE_T$  scaling. These particles are consistent with each other at  $KE_T/n_q < 0.7$  GeV. It indicates the quark level collectivity in the QGP and the quark coalescence mechanism to form hadron from quark matter via quark-gluon phase transition. The  $v_2$  scaling of quark number and  $KE_T$  is broken at  $KE_T/n_q > 0.7$  GeV. The  $v_2$  of  $\pi$  and  $p$  are approaching with each other at high  $p_T$  range (6 GeV/c). There could be another process which generates the high  $p_T$  particles such as jet production from hard process. In this case, the  $v_2$  is expected to be given by the path length dependence of the jet quenching coming from the partonic energy loss.

Jet-like event and un-jet-like event are separated by the highest momentum particle in each event. Jet-like event  $v_2$  is consistent with inclusive  $v_2$ , however un-jet-like event (trigger  $p_T < 1.2$  GeV/c)  $v_2$  is found to be smaller than inclusive minimum bias  $v_2$ . The hard  $v_2$  which is caused by an interplay between jet particles and the hot dense matter may affect soft  $v_2$  at the low momentum ( $p_T < 1.2$  GeV/c).

The  $v_2$  of  $\pi$ ,  $K$ ,  $p$  and  $d$  are measured in Au+Au  $\sqrt{s_{NN}} = 39$  and 62 GeV collisions. The  $v_2$  of the particles are almost scaled with the number of constituent quarks in the collisions. Considering the quark number scaling as an indication of the QGP phase, the threshold beam energy of QGP formation seems to be lower than the  $\sqrt{s_{NN}} = 39$  GeV.

The measured  $v_2$  of the particles is almost consistent with that of anti-particles in the Au+Au  $\sqrt{s_{NN}} = 200$  GeV collisions. While the  $v_2$  of particles (especially  $p$ ) differs from the  $v_2$  of anti-particles in the Au+Au  $\sqrt{s_{NN}} = 39$  and 62 GeV collisions. It could be given by interactions such as p-pbar annihilation within the high baryon density caused by the large net-baryon number from the baryon stopping in the low energy collision.

# Chapter 6

## Conclusions

The anisotropy of the particle emission depends on the elliptic initial system geometry in the heavy ion collision. It indicates the short mean free path of partons in the hot dense medium. The magnitude of the elliptic azimuthal anisotropy of the particle emission is measured as the second term of Fourier series ( $v_2$ ). The  $v_2$  gives information about the initial state and its expansion possibly through the QGP phase.

The  $v_2$  of identified hadrons depends on the mass of the hadron and the number of constituent quarks. The measured  $v_2$  increases with the transverse momentum  $p_T$  at  $p_T < 2$  GeV/c. The rise of  $v_2$  shifts towards higher  $p_T$  for heavier particles. It agrees with the collective expansion of the system according to the hydrodynamic model. The constant values of the  $v_2$  of the hadrons scale with the constituent quark number at around  $p_T = 3$  GeV/c. The  $v_2$  of hadron is the sum of  $v_2$  of combined partons in the quark coalescence model. It indicates that the flow of quarks in the QGP and QGP-hadron phase transition according to the quark coalescence model.

The  $v_2$  of rare particles should be compared as well as that of  $\pi$ ,  $K$  or  $p$  to obtain the conclusive evidence of the quark number scaling. The new reaction plane detector was installed to measure the  $v_2$  with the enhanced resolution of the event plane determination at RHIC-PHENIX experiment. It measures the azimuthal distribution of charged hadron yield with the acceptance of  $\phi = 2\pi$  and  $\eta = 1.5 - 2.8$ . The event plane was determined with two times better resolution compared to the ones measured before in the  $\sqrt{s_{NN}} = 200$  GeV Au+Au collision in PHENIX experiment. The higher resolution allows us to study  $v_2$  of rare particles or low energy collisions. The detector worked well for  $\sqrt{s_{NN}} = 200$  GeV Au+Au collisions in 2007 and  $\sqrt{s_{NN}} = 39$  and 62 GeV Au+Au collisions in 2010.

The  $v_2$  of  $\pi$ ,  $K$ ,  $\phi$ ,  $p$ ,  $\bar{p}$ ,  $\Lambda$ ,  $\bar{\Lambda}$ ,  $d$  and  $\bar{d}$  were measured in Au+Au  $\sqrt{s_{NN}} = 200$  GeV collisions. The  $v_2$  of  $K$  is smaller than the  $v_2$  of  $\pi$  and the  $v_2$  of  $\phi$  is smaller the  $v_2$  of  $K$  at  $p_T < 2$  GeV/c. This result agrees with the expectation that the heavy particles get larger transverse momentum via radial flow according to the hydrodynamic model. The blast-wave function describes the  $p_T$  spectra via the radial expansion with parameters of the local thermal temperature and the radial velocity at the freeze out. The blast-wave function is extended to describe the  $v_2$  as a function of  $p_T$ . The initial geometrical density distribution is taken from Glauber Monte-Carlo model with Wood-Saxon distribution. The additional elliptic expansion parameter, where the initial density distribution can expand into the reaction plane direction, is included to determine the final density distribution at the freeze-out. The gradient of the density distribution is used as the velocity profile and is scaled by the overall radial expansion velocity. The final eccentricity was given by the blast

wave fitting with the measured  $p_T$  spectra and the  $v_2$  of the six particles. The freeze-out eccentricity has been found to be smaller than the initial eccentricity, but it still holds the same orientation. The observation is consistent with the eccentricity extracted from Hunbury Brown and Twiss (HBT) effect measurement.

The  $v_2$  of baryons are larger than the  $v_2$  of mesons and the  $v_2$  of  $d$  is higher than the  $v_2$  of baryons at  $p_T > 3$  GeV/c. The  $KE_T = m_T - m_0$  scaling describes the  $v_2$  shift by the mass effect and it is used to compare the constituent quark number dependency clearly. The  $v_2$  of  $\pi$ , K and  $\phi$  (mesons) or  $p$  and  $\Lambda$  (baryons) are consistent separately with  $KE_T$  scaling. The  $v_2$  as a function of  $KE_T$  of mesons, baryons and  $d$  seem to be given by centrality and the number of constituent quarks of the particles  $n_q$ . The  $v_2/n_q$  of the particles are consistent with each other at  $KE_T/n_q < 0.7$  GeV.  $\phi$  has the smaller cross section of the hadronic re-scattering. Therefore this consistency of the  $v_2$  of the particles indicates that the dominant fraction of the elliptic anisotropy is formed before the QGP-hadron phase transition and less affected from the hadronic re-scattering after the QGP-hadron phase transition. The scaled  $v_2$  with the number of constituent quarks of the five hadrons and  $d$  indicates the quark level collectivity in the QGP, and hadron generation according to the quark coalescence mechanism during QGP-hadron phase transition.

The scaling of  $n_q$  and  $KE_T$  is broken at  $KE_T/n_q > 0.7$  GeV. The  $v_2$  of  $\pi$  and  $p$  are approaching each other at the high  $p_T$  range (6 GeV). There would be another generation process of the particles such as jet production from hard process. In this case,  $v_2$  of the high  $p_T$  particle is expected to be given by the path length dependence of the jet quenching coming from the partonic energy loss.

It is expected that  $d$  is formed from  $n$  and  $p$  at the final stage of collision because the smaller binding energy of  $p-n$  than that of quarks in hadron. The  $v_2$  of  $d$  should be the sum of the  $v_2$  of  $p$  and  $n$  if the nucleon coalescence model is established. The measured  $v_2$  of  $d$  is found to be lower at  $p_T < 3$  GeV/c and higher at  $p_T > 3$  GeV/c than the  $v_2$  of  $p$ . The  $d$   $v_2$  can also be scaled with parton number, since the proton  $v_2$  is known to be scaled. It means that  $n$  has the  $v_2$  as a function of  $p_T$  same as  $p$  and the  $v_2$  of  $d$  is less affected from hadronic re-scattering from hadronization to  $p-n$  coalescence.

The jet-like events and the un-jet-like events are separated with the highest momentum particle in each event. The  $v_2$  of the jet-like event is consistent with inclusive  $v_2$ . The  $v_2$  of un-jet-like event (trig  $p_T < 1.2$  GeV/c) is lower than that. The hard  $v_2$  which is caused by an interplay between jet particles and the hot dense matter may affect soft  $v_2$  at the low momentum ( $p_T < 1.2$  GeV/c).

The  $v_2$  of  $\pi$ ,  $K$ ,  $p$ ,  $\bar{p}$  and  $d$  are measured in Au+Au  $\sqrt{s_{NN}} = 39$  and 62 GeV collisions. The  $v_2$  of the particles are mostly scaled with the number of constituent quarks in the collisions, too. Considering this as the indication of the QGP phase, the threshold energy of the QGP-hadron phase transition would be lower than the  $\sqrt{s_{NN}} = 39$  GeV.

The measured  $v_2$  of the particles are almost consistent with that of anti-particles in the Au+Au  $\sqrt{s_{NN}} = 200$  GeV collisions. On the other hand, the  $v_2$  of particles (especially  $p$ ) differ from the  $v_2$  of anti-particles in the Au+Au  $\sqrt{s_{NN}} = 39$  and 62 GeV collisions. It could be given by interactions such as  $p-\bar{p}$  annihilation in the high baryon density caused by the baryon stopping in the low energy collision.

The precise measurement of the elliptic flow  $v_2$  of the identified hadrons with the new reaction plane detector has been carried out. The results indicate the partonic collective flow and the quark coalescence mechanism in  $\sqrt{s_{NN}} = 200$  GeV Au+Au collisions. The quark number scaling of elliptic flow could be taken as the indicator of formation of QGP phase in high energy heavy ion collision, while the scaling has been observed to be broken at high  $p_T$ . Study of elliptic flow in lower energy heavy ion collisions has also been done to search for the threshold behavior of collision energy for

QGP-hadron phase transition and it is found to be lower than  $\sqrt{s_{NN}} = 39$  GeV for Au+Au collision.

# Chapter 7

## Acknowledgments

I would like to express my deepest gratitude to Prof. Dr. Y. Miake and Prof. S. Esumi whose comments and suggestions were innumerable valuable throughout the course of my study.

I acknowledge the high energy nuclear experiment group of University of Tsukuba and members of that. I express my thanks to Prof. T. Chujo, Prof. M. Inaba, , Prof. H. Masui, Dr. S. Sakai, Dr. M. Konno, Dr. K. Miki, Dr. M. Shimomura, Dr. T. Niida, Mr. R. Tanabe, Mr. K. Watanabe, Dr. D. Sakata, Mr. M. Sano, Mr. T. Todoroki, Mr. H. Yokoyama, Mr. E. Hamada, Ms. M. Kajigaya and Ms. M. Kimura and Mr. S. Kato for their useful advise and many supports.

I acknowledge the collaborators of the PHENIX experiment with the Relativistic Heavy Ion Collider(RHIC) and the RIKEN Radiation Laboratory. I have analyzed the data of heavy ion collisions with the RHIC Computer Facility(RCF) and the RIKEN Computer Center in Japan(CCJ). I appreciate to Dr. H. Enyo, Dr. Y. Akiba, Dr. S. Yokkaichi, Dr. J. S. Haggerty, Dr. T. Sakaguchi, Prof. R. Seto, Dr. S. Huang, Dr. A. Taranenko, Dr. R. Pak, Dr. W. Xie, Dr. E. Richardson, Dr. R. Wei and Dr. T. Hachiya for their valuable advices and supports for analysis and detector-works.

I appreciate to Prof. T. Hirano and Dr. K. Murase for their useful advices and informations for theoretical approach with hydrodynamic model and blast-wave model.

I acknowledge High Energy Accelerator Research Organization(KEK), Brookhaven National Laboratory(BNL) and U.S. Department of Energy(DOE) for their support for studying nuclear physics.

I express my gratitude to my family for their moral support and warm encouragements.

# Reference

- [1] F.Karsch, in:Lecture Notes in Physics **583**, 209 (2002).
- [2] F. Karsch, E. Laermann, and A. Peikert, Phys. Lett. B **478**, 447 (2000).
- [3] E.V.Shuryak, Phys. Rep. **61**, 71 (1980).
- [4] J.C.Collins, M.J.Perry, Phys. Rev. Lett. **34**, 1353 (1975).
- [5] Michael L. Miller, Klaus Reygers, Stephen J. Sanders, Peter Steinberg, nucl-ex/0701025.
- [6] J. D. Bjorken, Phys. Rev. D **27**, 140 (1983).
- [7] P. F. Kolb, Heavy Ion Phys. **21**, 234 (2004).
- [8] K. Guettler et al., Phys. Rev. D **64**, 111 (1976).
- [9] B. Alper et al., Nucl. Phys. B **100**, 237 (1975).
- [10] J. Y. Ollitrault, Phys. Rev. D **46**, 229, (1992).
- [11] Nu Xu for the NA44 Collaboration, Nucl. Phys. A **610**, 175 (1996).
- [12] I.G. Berden et al., Phys. Rev. Lett. **78**, 2080 (1997).
- [13] S. S. Adler et al., Phys. Rev. C **69**, 034909 (2004).
- [14] P. Houvinen, P.E. Kolb, U.W. Heinz, P.V. Ruuskanen and S.A. Voloshin, Phys. Lett. B **503**, 58 (2001).
- [15] S. S. Adler et al., Phys. Rev. Lett. **91**, 182301 (2003).
- [16] R.J. Fries, B. Muller, C. Nonaka, S.A. Bass, Phys. Rev. Lett. **90**, 202303 (2003).
- [17] R.J. Fries, B. Muller, C. Nonaka, S.A. Bass, Phys. Rev. C **68**, 044902 (2003).
- [18] Asher Shor, Phys. Rev. Lett. **54**, 1122 (1985).
- [19] M. Allen et al., NIM A **499**, 549 (2003).
- [20] C. Adler et al., Nucl. Instrum. Meth. A **470**, 488 (2001)
- [21] <http://www.phenix.bnl.gov/techpapers.html>

- [22] <http://adsabs.harvard.edu/abs/2006APS..DNP.GH008K>
- [23] S.H. Aronson et al., Nucl. Instrum. Methods Phys. Res. A **499**, 480 (2003).
- [24] K. Adcox et al., Nucl. Instr. and Meth. A **497**, 263 (2003).
- [25] G. David et al., IEEE Trans. Nucl. Sci. **45**, 692 (1998).
- [26] A.L.S. Angelis et al., CERN/SPSLC/91-17, (1991).
- [27] B. B. Black, et al., Phys. Rev. Lett. **91**, 052303 (2003).
- [28] B. B. Black, et al., Phys. Rev. Lett. **94**, 122303 (2005).
- [29] HAMAMATSU(<http://jp.hamamatsu.com/>)
- [30] J. Haggerty et al., Letter of Intent for PHENIX Reaction Plane Detector (2006).
- [31] E. Richardson et al., Nucl. Instr. And Mass. A **636** 99 (2010)
- [32] A. M. Poskanzer and S. A. Voloshin, Phy. Rev. C **58**, 1671 (1998).
- [33] A. Adare et al., Phys. Rev. C **85** 064914 (2012).
- [34] A. Adare et al., Phys. Rev. C **84**, 044905 (2011).
- [35] Catherine Silvestre for the PHENIX Collaboration, Eur. Phys. J. C **61**, 841 (2009).
- [36] Zi-Wei Lin, et. al., Phys. Rev. C **72**, 064901 (2005).
- [37] Haidong Liu for the STAR Collaboration, J. Phys. G: Nucl. Part. Phys. **34**, S1087 (2007).
- [38] C. Nonaka et al., Phys. Rev. C **69**, 031902, (2004).
- [39] T. Hirano, U. Heinz, D. Kharzeev, R. Lacey, and T. Nara, Phys. Rev. C **77**, 044909 (2008).
- [40] F. Retiere, and M. A. Lisa, Phys. Rev. C **70**, 044907 (2004).